Polaron hopping in olivine phosphates studied by nuclear resonant scattering

Thesis by

Sally June Tracy

In Partial Fulfillment of the Requirements

for the Degree of

Doctor of Philosophy

California Institute of Technology

Pasadena, California, USA

2016

(Defended September 3, 2015)

For Matt

There's no such thing as a perfect piece of writing.

Just as there's no such thing as perfect despair.

-Haruki Murakami, Hear the Wind Sing

Acknowledgments

I would like to acknowledge my advisor, Dr. Brent Fultz, for his guidance during the years I spent at Caltech. I hold Professor Fultz's intellectual taste in high esteem and have been impressed by his thoughtful approach to science and dedication to a thorough understanding of fundamental questions. Furthermore, Professor Fultz is skilled in the art of always providing an optimum level of guidance, giving his students the space to grow into independent scientists but not letting them get too far off track along the way. I would also like to thank my undergraduate advisor, Professor George Schmiedeshoff, who first exposed me to scientific research. Without his push, I most likely would not have had the confidence in my own abilities to pursue research. I would be remiss not to mention my post-baccalaureate mentor Dr. Jason Cooley, who has always been someone I felt I could come to with questions. It has always amazed me that whatever the inquiry, even if he doesn't have an answer off hand, he will always know where to point you to find what you are looking for. I am always surprised, but incredibly grateful, that he seems to still take interest in what I am doing and continues to support me in whatever ways he can. I can only hope that his students since me have not caused him as much trouble.

I would like to express my gratitude to the faculty on campus who have generously allowed us access to their lab space, especially Professors Jennifer Jackson, William Johnson, and George Rossman. The access to equipment to synthesize samples as well as the ability to prepare diamond anvil cells on campus and collect Raman spectra was invaluable in making the experiments in this thesis possible. In addition to these faculty, I would like to acknowledge the other member of my committee, Professor Katherine Faber. I would like to thank all the people involved with EFree and HPCAT as well as the other scientists at Geophysical Lab and the Advanced Photon Source with whom I have had the chance to interact. In particular, I would like to express my appreciation of the technical staff at HPCAT and GSECARS who design and maintain an extensive suite of diamond-

anvil cell preparation tools and sample environments for high-pressure measurements. Access to this equipment, along with their dedicated user support, was invaluable in collecting the data in this thesis.

During my time at Caltech, I have had the pleasure of working closely with Dr. Lisa Mauger. Without Lisa's help there is no way most of this work would have been completed. During this time, Lisa has served as mentor, a collaborator and friend. I am continually amazed with her experimental prowess and her pragmatic outlook of life. I can only hope that the countless sleepless nights spent at the APS have forged a lifetime bond that will yield fruitful collaborations in the future and a lifelong friendship. I would also like to mention the other students I had the chance to collaborate with while at Caltech, particularly my former officemate Dr. Jorge Muñoz, who shared my inclination for working late at night, and is someone whom I hold in high regard. I would also like to thank Dr. Hongjin Tan, who is always a jovial labmate and was kind enough to teach me a bit of chemistry. More recently I also have had the pleasure of working with both Jane Herriman and Dr. Hillary Smith. I must also mention my other Los Angeles friends, particularly Lizzie Adelman and Amanda Armstrong. During my years in graduate school, spending time with these two was always a much needed breath of fresh air. They are really the best friends anyone could ask for.

Finally, I would like recognize my family for their ongoing love and support. I credit my parents with instilling me with a strong work ethic and creative outlook on the world. Whether helping her nearly thirty year old daughter edit her resumé, shoe shopping, or grading middle school social studies reports, my mother tackles the task at hand with what can only be described as an intense and unrelenting fervor. Regardless of the circumstance, this ardent pursuit of perfection will only come to a close when she has gone above and beyond the call of duty. I have always admired my father's unwillingness to subscribe to other people's notions of fulfillment and success. I would like to think I have inherited some of this unique outlook, his intellectual curiosity, and perhaps a dash of his anti-authoritarian convictions. I would also like to mention my sisters. While at times I found it difficult to be in the middle of two accomplished and well liked sisters, who were spared (to varying degrees) my intensely socially awkward tendencies, I feel incredibly fortunate to have two incredible and generous sisters. I can only hope that the official completion of my many, many years of schooling will allow me to make my final assent to crown status as the undisputed golden child. Last but most important, I would like to thank my partner Matt Graham, who has continually

made sacrifices to allow me to pursue my education. His patience with me and tolerance of my often neurotic behavior continues to amaze me. I am incredibly lucky to have a companion who challenges me and makes me laugh. Without him I would be lost.

Abstract

Valence fluctuations of Fe^{2+} and Fe^{3+} were studied in a solid solution of Li_xFePO_4 by nuclear resonant forward scattering of synchrotron x rays while the sample was heated in a diamond-anvil pressure cell. The spectra acquired at different temperatures and pressures were analyzed for the frequencies of valence changes using the Blume-Tjon model of a system with a fluctuating Hamiltonian. These frequencies were analyzed to obtain activation energies and an activation volume for polaron hopping. There was a large suppression of hopping frequency with pressure, giving an anomalously large activation volume. This large, positive value is typical of ion diffusion, which indicates correlated motions of polarons, and Li^+ ions that alter the dynamics of both.

In a parallel study of Na_xFePO_4, the interplay between sodium ordering and electron mobility was investigated using a combination of synchrotron x-ray diffraction and nuclear resonant scattering. Conventional Mössbauer spectra were collected while the sample was heated in a resistive furnace. An analysis of the temperature evolution of the spectral shapes was used to identify the onset of fast electron hopping and determine the polaron hopping rate. Synchrotron x-ray diffraction measurements were carried out in the same temperature range. Reitveld analysis of the diffraction patterns was used to determine the temperature of sodium redistribution on the lattice. The diffraction analysis also provides new information about the phase stability of the system. The temperature evolution of the iron site occupancies from the Mössbauer measurements, combined with the synchrotron diffraction results give strong evidence for a relationship between the onset of fast electron dynamics and the redistribution of sodium in the lattice.

Measurements of activation barriers for polaron hopping gave fundamental insights about the correlation between electronic carriers and mobile ions. This work established that polaron-ion interactions can alter the local dynamics of electron and ion transport. These types of coupled processes may be common in many materials used for battery electrodes, and new details concerning

the influence of polaron-ion interactions on the charge dynamics are relevant to optimizing their electrochemical performance.

Contents

List of Figures

Chapter 1

Introduction

1.1 Motivation

A global transition to renewable energy sources is of vital importance for the future of our planet. The challenge lies in finding creative ways to sustainably support a world of nine billion people while allowing for the continued globalization of modern technology. While I have hope that attitudes of indifference and the lack of education concerning human environmental impacts represent trends that are shifting, it is important to recognize that the only surefire way to institute change is through the development new technologies that make the transition to sustainable alternatives both convenient and affordable.

Energy storage remains a critical challenge in the transition to green energy. Rechargeable batteries have emerged as a particularly promising storage choice. Batteries can be designed in numerous shapes and sizes and are adaptable to a wide range of uses. The increasing reliance on batteries for portable electronics, electric vehicles and even large scale grid storage necessitates further research aimed at discovering new high-performance battery materials that are affordable, environmentally friendly, and safe. This goal requires a fundamental understanding of the material properties that effect electrode performance.

Transport of electrons and ions is a central issue in many energy storage materials. In particular, battery-cathode materials require relatively facile mobility of intercalation ions as well as reasonable mobility of electronic carriers. The electronic conduction mechanism in many transition-metal oxide cathodes is small polaron hopping. This mode of electronic transport is characterized by

phonon-assisted hopping of localized carriers between adjacent transition-metal ion sites. The aim of the work presented in this thesis was to develop a more detailed picture of charge transport in these framework oxides and better understand how the phase stability and transport properties of these materials are affected by electron-ion interactions.

1.2 Overview

Candidate cathode materials, specifically $LiFePO_4$ and $NaFePO_4$, were studied using a combination of synchrotron x-ray diffraction and nuclear resonant scattering for a range of temperatures and pressures. Both ion diffusion and small polaron hopping can be understood as activated processes having an Arrhenius-type temperature dependence. Consequently, measurements of the electronic charge hopping frequency as a function of temperature allow for the determination of an activation energy. Nuclear resonant scattering presents an ideal technique to examine the valence fluctuations that accompany polaron hopping in iron-bearing cathode materials. These measurements provide a local probe at the iron ion that is sensitive to valence switching within a frequency range that is well suited for studies of polaron dynamics.

Extending these measurements to elevated pressure using synchrotron techniques allows for the additional determination of an activation volume. This quantity can provide a window into the atomic rearrangements that occur during the transient state of a hopping event. The activation energy is the energetic barrier for the moving species to hop between adjacent sites. The activation volume quantifies the effect of pressure on this activation barrier, as it gives the local change in volume as the particle moves through its transition state. The important role of activation energy in setting the temperature dependence of the transport process is well known, but the activation volume is less well understood. The experiments in this thesis revealed new information concerning the nature of the activation barriers for polaron hopping in mixed electron-ion conductors.

Synchrotron x-ray diffraction carried out in the same temperature range gives complementary information concerning the structural evolution and phase stability of these materials with temperature and pressure. Combined with the nuclear resonant scattering results, diffraction data provides insight into the relationship between the development of disorder on the alkali-ion sublattice and the enhancement of electronic mobility. Additionally, the structural information obtained from these

Figure 1.1. Replica of Alessandro Volta's original cell, composed of a stack of zinc and copper disks. Figure: GuidoB- CC BY-SA 3.0

measurements gives insights into the relationship between ion ordering and electronic mobility.

1.3 Battery background

With the advent of consumer electronics, global societies are becoming increasingly reliant on battery technology, driven by an ever-increasing demand for portable power sources. The use of batteries as devices for electrochemical energy storage and conversion is by no means new technology. The first modern battery dates back to the Enlightenment, when Alessandro Volta, an Italian professor of natural philosophy, described his "voltaic pile" in an 1800 report to the London Royal Society. Volta's device was composed of a stack of zinc and copper disks immersed in a saltwater brine that served as an electrolyte [4]. Fig. 1.1 shows a replica of the original cell on display at a museum near Volta's home in Como, Italy. While the fundamental concepts of the electrochemical cell remain unchanged, contemporary developments in materials technology continue to make batteries a viable power source for modern electronics, and battery research now represents a diverse and vibrant field.

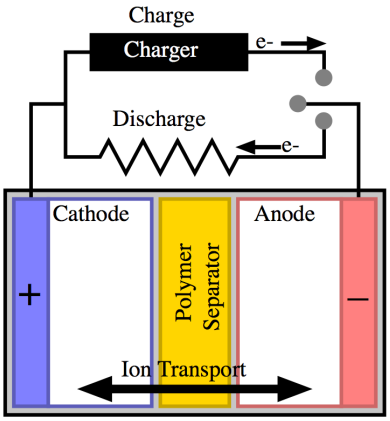

Figure 1.2. Essential components of electrochemical cell.

1.4 Lithium-ion cathode materials

During the operation of a conventional rechargeable lithium battery, lithium diffuses out of the anode material (usually graphite) and is transported through the electrolyte and through an electrically insulating separator layer. The Li-ions are then intercalated into the crystal structure of the cathode material. During this discharge process, electrons are transferred through an external circuit, providing usable electronic energy. To recharge the cell, a voltage is applied across the electrodes forcibly extracting lithium from the cathode material. The ions diffuse back through the electrolyte and are reinserted into the anode.

The material properties of the anode and cathode materials establish the overall performance of the electrochemical cell. The amount of lithium that can be reversibly extracted and reinserted into the cathode's crystal structure determines the cell's overall capacity and the relative Fermi energies of the anode and cathode set the cell voltage. An ideal material has a high energy density and exhibits good stability on cycling. It is also essential that the cathode is a good ionic conductor and exhibits reasonable electronic conductivity. Preferably the material is also non-toxic and affordable. The majority of commercial batteries today contain $LiCoO_2$ cathodes. Cobalt is not only expensive but is also quite toxic. Consequently, there is a great deal of interest finding viable cathode materials that contain alternate multivalent elements.

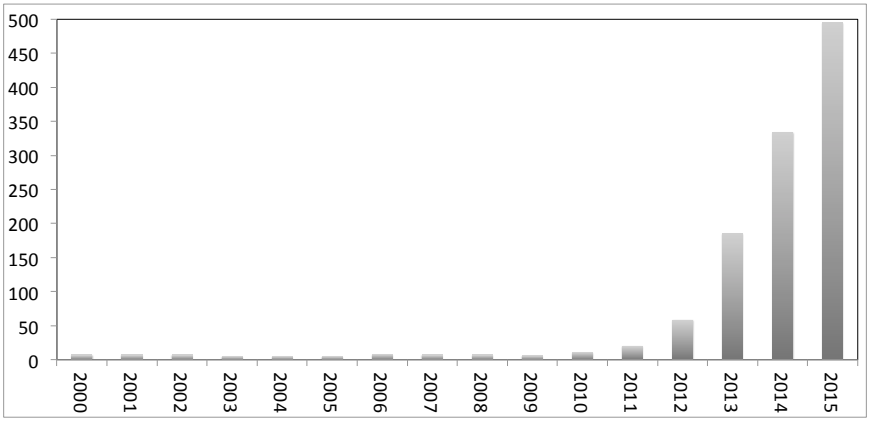

Figure 1.3. Yearly breakdown of number of Na-ion battery manuscripts in the last fifteen years. The total number of manuscripts in 2015 has been projected based on the number published up through July.

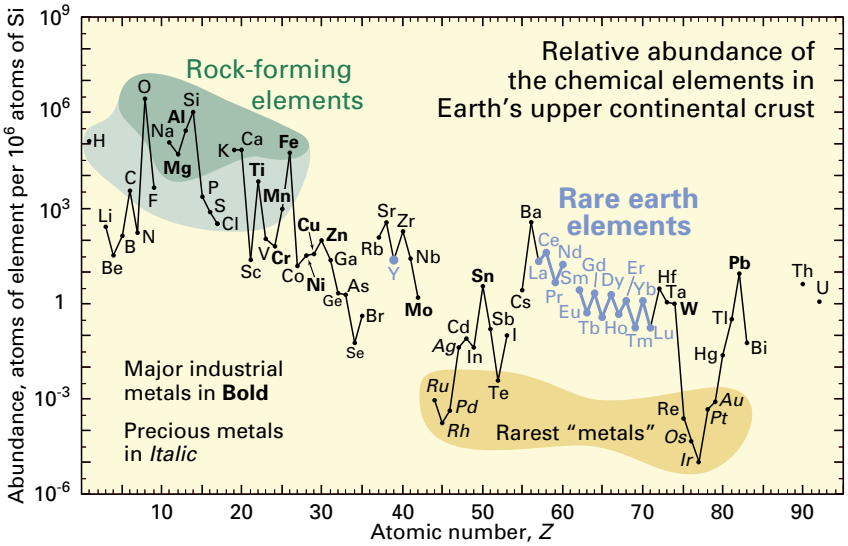

Figure 1.4. Atom fraction of the chemical elements in Earth's upper continental crust as a function of atomic number. Major rock-forming elements are shown in green field and minor rock forming elements are in light green field. The major industrial metals are shown in bold. Figure courtesy of the United States Geological Survey.

1.5 Sodium-ion cathode materials

Rechargeable sodium-ion batteries were first proposed in the same time period as early work on lithium batteries [5–10]. Due to the overwhelming successes of Li-ion technology, research tended to move in this direction and interest in these sodium systems dwindled. In recent years there has been a resurgence of interest in Na-ion batteries. Figure 1.3 shows the yearly breakdown of number of manuscripts on sodium-ion batteries in the last fifteen years. While this trend would be dwarfed by a similar plot of lithium-ion battery studies, the figure makes it apparent there has been an explosion of interest in the topic within the last few years. This newfound interest can be attributed mainly to the fact that in the last twenty years our society has rapidly become dependent on Li-ion technology. Given this rising demand, it has become apparent that lithium itself is a limited resource. In contrast, sodium is relatively plentiful. The abundance of various elements in the earth's crust is illustrated in Figure 1.4. Sodium is situated in the dark green field, indicating it is one of the major rock forming elements, as opposed to lithium that sits below the light green field of the minor rock forming elements. Consequently, the prospect of creating sodium analogues to lithium-ion batteries has become immensely attractive. Furthermore, in Fig. 1.4 cobalt can be found well below even lithium, motivating the interest in cathodes containing alternative earth-abundant transition metal redox ions, for example iron, manganese or magnesium.

Sodium-ion batteries have the potential to be significantly cheaper than their lithium-ion analogues. The prospect of designing a more affordable class of batteries enhances the feasibility of employing batteries for large scale grid applications. Much of the knowledge that has been acquired through the investigation of lithium systems is relevant to sodium cathodes, but Na-ion chemistry allows for additional intercalation structures, some of which may not form in their lithium counterparts. Although known sodium-ion systems tend to have lower energy densities and voltages, these details are surprisingly sensitive to the cathode's crystallography. An in-depth understanding of how crystal structure affects the transport properties and performance of these materials is critical to designing competitive sodium batteries.

1.6 Crystallography of framework oxides

1.6.1 Overview of cathode crystal structures

The performance a cathode is strongly influenced by the details of the material's crystal structure. An important feature is the availability of diffusion channels for alkali ions. Furthermore, the dimensionality of these diffusion pathways plays a key role in setting the overall rate capacity. Figure 1.5 shows the crystal structures for a range of different types prospective cathode materials. The most well established of these materials are the $LiMO_2$ layered structures, where the transition-metal ions (M) are generally cobalt or nickel and lithium ions are inserted between sheets of corner sharing MO_6 octahedra. Different stacking sequences of the oxygen planes give rise to different variants of these layered-type structures. The Natrium Super Ionic CONductor (NASICON) family ($A_xMM'(XO_4)_3$, A=Na, Li) is characterized by a three-dimensional scaffolding of metal-oxygen octahedra (MO_6 and $M'O_6$) corner-linked with phosphate or silicate tetrahedral units, XO_4. This open framework forms large interconnected channels for alkali ion mobility. The spinel family is another popular cathode candidate, most commonly $LiMn_2O_4$. This structure is composed of a cubic close pack lattice with Mn and Li cations occupying one-half and one-eighth of the octahedral and tetrahedral sites, respectively. Spinels have the benefit of three-dimensional ion conduction pathways, wherein alkali ions can move between tetrahedral sites via the unoccupied octahedral sites in the structure. More recently the orthosilicates have emerged as a promising possibility. The Li_2MSiO_4 family (M= Mn, Fe, Co) presents the potential for a M^{4+}/M^{2+} two electron redox reaction. The orthosilicates exhibit complex polymorphism and there is controversy over structural changes that occur during cycling. Notwithstanding, there is consensus that the general framework is composed of a distorted hexagonal close packing of oxygen with half of the tetrahedral sites filled by cations such that two dimensional layers of LiO_4 tetrahedra are linked by silicate tetrahedra. While the diffusion pathways in these structures are less well characterized, it is likely that these LiO_4 layers enable two-dimensional ion diffusion. The possibility of a Li_2FeSiO_4 cathode is especially appealing as all the constituent elements are members of the major rock-forming group at the top of Fig. 1.4.

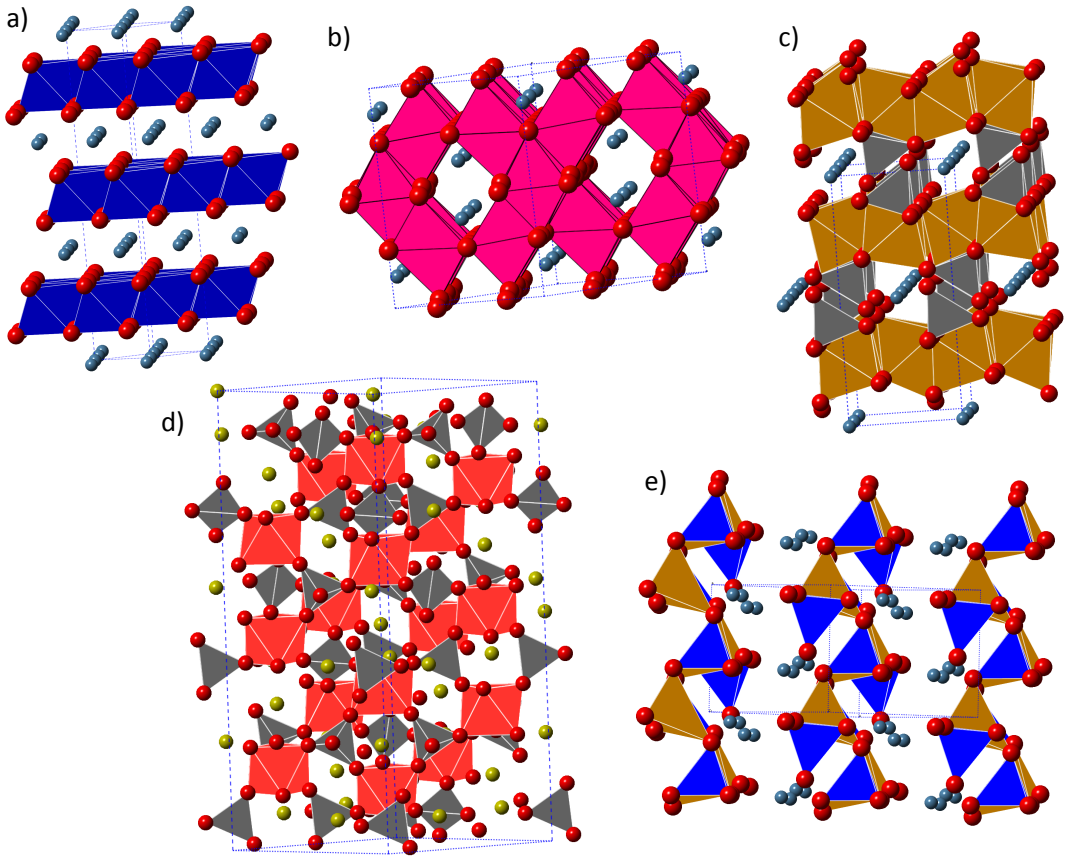

Figure 1.5. Crystal structures of prospective cathode materials, illustrating different dimensionalities of alkali ion diffusion pathways. a) Layered $LiCoO_2$ where colbalt octahedra are shown in royal blue, Li ions are in light blue and oxygen are in red. b) Spinel, $LiMn_2O_4$ with Mn ions in magenta. c) Olivine, $LiFePO_4$, with iron in light brown and phosphate tetrahedra in grey. d) $Na_3V_2PO_4$ NASICON structure with Na ions in yellow and vanadium octahedra in red.) Li_2FeSiO_4 with silicate tetrahedra in blue.

1.6.2 Triphylite

The focus of this thesis is the olivine-phosphate family, $MFe^{2+}PO_4$ (M=Li, Na). The olivine structure can be understood as a hexagonal close-packed array of oxygen atoms, with alkali and iron ions occupying half of the octahedral sites and phosphate atoms occupying one-eighth of the tetrahedral sites. The orthorhombic Pmna structure is shown in Fig. 1.6 (a). Layers of corner-sharing networks of canted FeO_6 octahedra in the b-c plane are spaced by phosphate tetrahedra, and Li^+ cations form one-dimensional chains that run between the FeO_6 planes. Within typical olivine notation, iron cations sit in the M1 octahedral sites and the alkali ions occupy the M2 sites. Upon lithium extraction, $Fe^{3+}PO_4$ has the same underlying structure with unfilled M1 octahedral voids, shown in Fig. 1.6 (b). The structures are often referred to by their mineral names triphylite and heterosite, for the lithiated and delithiated structures, respectively. In contrast to the structures discussed above, the diffusion path in triphylite is restricted to one dimension, along the b-axis channels. Due to this reduced dimensionality, ion mobility suffers as a result of channel blockage by defects, specifically cation Fe-Li antisite defects [11, 12]. It has been established that the rate capacity of the material can be improved by using nanosized cathode particles [13, 14]. The reduction in particle size will reduce the length of any given channel, reducing the probability that it is blocked.

1.6.3 Maricite

The ground state structure of the sodium analogue of $LiFePO_4$ is the maricite structure, shown in Fig.1.7(b). While density functional theory calculations suggest the ground state energies of the two structures are essentially equivalent [15], it is apparent that the maricite structure is favored at higher temperatures where the material is synthesized. The only known way to form triphylite-$NaFePO_4$ is through a chemical ion-exchange process using $LiFePO_4$ as the starting material. Once formed, the triphylite structure is stable up to temperatures of $\sim$800 K, at which point it will revert back to the maricite structure [16]. Calculations suggest a lithium analogue of the maricite structure is unstable and it has not been observed [15].

Maricite draws little to no interest from the electrochemical community as there are no apparent conduction pathways for sodium ions. Compared to the triphylite-type structure favored by $LiFePO_4$, the site occupancies of the alkali ion are swapped with the iron cations. The sodium

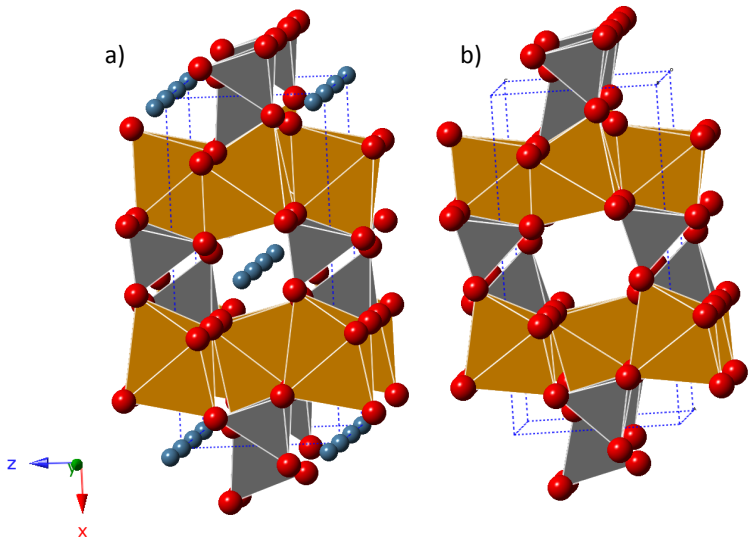

Figure 1.6. Orthorhombic olivine-phosphate structure. (a) Lithiated triphylite structure. (b) Delithiated heterosite structure. Iron octahedra are shown in brown, oxygen ions are in red, phosphate tetrahedra are in grey and lithium ions are in blue.

cations are isolated by the phosphate groups, and the structure is electrochemically inactive. Figure 1.7 shows a comparison of the two structures. In the triphylite structure the iron ions occupy the larger M2 octahedral sites, having corner sharing connectivity, and the alkali ions occupy the smaller edge sharing M1 octahedra. This edge type connectivity of the M1 octahedra creates a facile channel for ion mobility. In maricite the occupancies are switched, putting the alkali ions into the corner sharing M1 sites where there is no good pathway for ion diffusion. Despite the larger size of the sodium ions, the sodiated triphylite structure has reasonably good ionic conductivity and shows noteworthy electrochemical performance compared to other sodium-ion cathode materials [17, 18]. As both polymorphs are variants of the olivine structure, they will be distinguished by using their mineral names, triphylite and maricte.

1.7 Phase stability of olivine phosphates

Li_xFePO_4 is known to exhibit two-phase behavior at room temperature, with minimal Li/vacancy solubility in the end members. Despite the tendency for total phase separation, the observed viability of the intercalation process implies there is necessarily some amount of solubil-

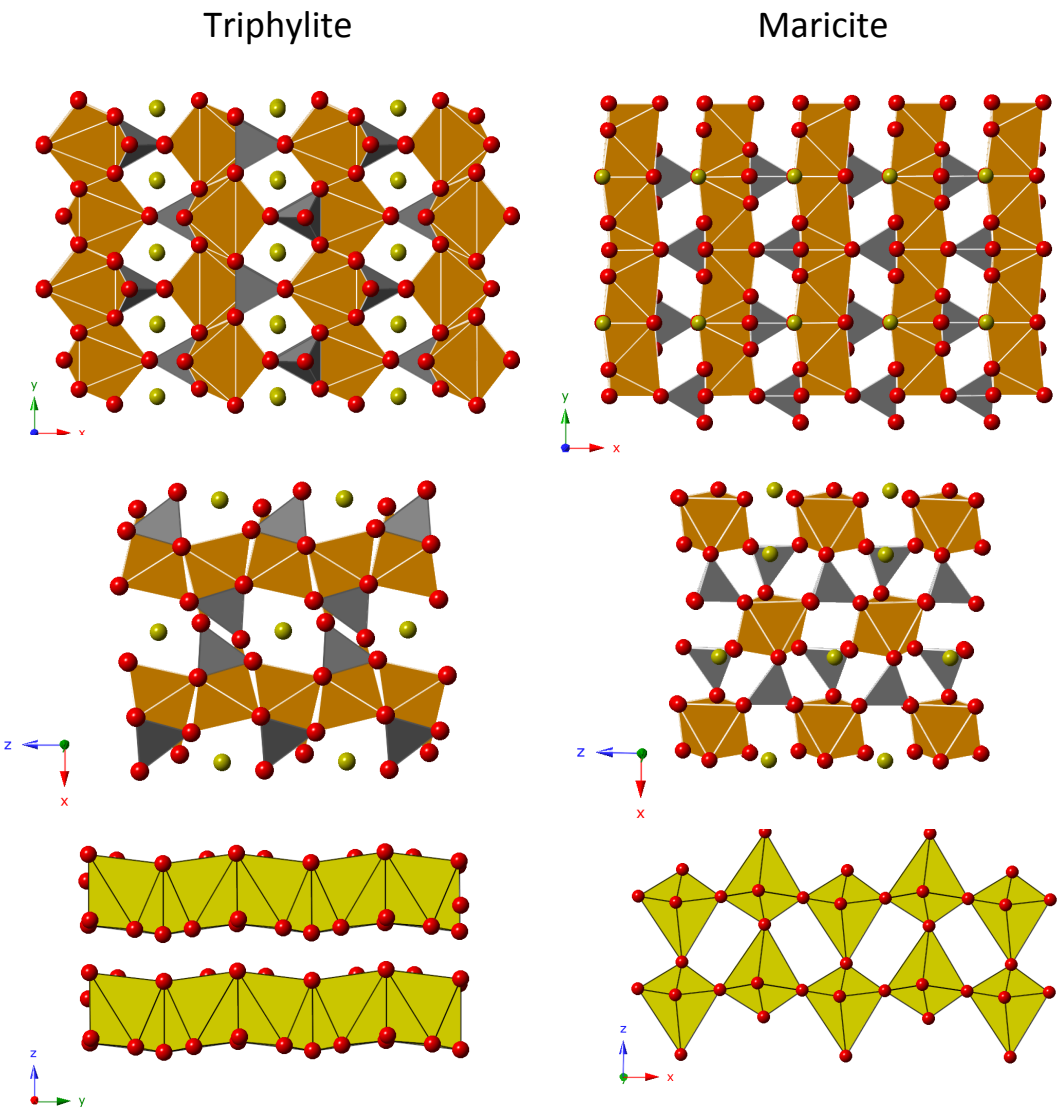

Figure 1.7. A comparison of the triphylite and maricite crystal structures.The first two rows show different views of the structures and the last row depicts the differences in the alkali ion octahedra connectivity. Iron octahedra are shown in brown, oxygen ions are in red, phosphate tetrahedra are in grey and sodium ions/octahedra are in yellow.

ity. The idea that the solubility limits are enhanced with reduced particle size has been discussed, as well as the suggestion of some sort of kinetically stabilized intercalation route [19–21]. There has been a great deal of interest in better understanding the details of how the lithiation process proceeds, specifically wether it occurs particle by particle though some sort of "domino cascade" process, wherein after a nucleation event the phase boundary propagates rapidly perpendicular to the b-axis diffusion channels, such that at any given time all particles are either fully lithiated or delithiated [22].

For temperatures above 500 K, the Li_xFePO_4 phase diagram exhibits a broad solid solution with a eutectoid around x=0.6 [23, 24]. It has been suggested that the details of the two-body coulombic interactions between the Li-ions, vacancies, electrons and holes have an influence on the phase stability, particularly for intermediate compositions where lithium removal gives rise to mixed valent iron ions. The attractive Li^+/Fe^{2+} and vacancy/Fe^{3+} interactions contribute to a tendency for phase separation while the repulsive Li^+/Li^+ and vacancy/vacancy interactions tend to stabilize a solid solution. The electronic configurational entropy gained from disordering Fe^{2+} and Fe^{3+} on the lattice is thought to account for the stabilization of the solid solution at high temperatures [25].

Although the phase diagram for Na_xFePO_4 has not been as well characterized as the lithium system, it is clear that there are some interesting distinctions when Na^+ replaces Li^+ as the intercalation ion. While these discrepancies in phase behavior are potentially an effect of differences between Na^+ and Li^+ interactions in the material or a result of differences in the ion's electronegativity, they likely arise as a result the size discrepancy in ionic radii. The ionic radius is more than 30% larger for Na^+ than Li^+, and full sodiation of the $FePO_4$ lattice results in a nearly 17% volume expansion, compared to the 7% expansion seen in $LiFePO_4$ [16]. For Na concentrations above x=2/3, there is a stable solid solution phase even at low temperatures. Below x=2/3 there exists an intermediate ordered phase that only disorders above $\sim$500 K. The ordered phase is described by a structure having a vacancy at every third sodium site along the Pmna b-axis [26]. Below x=2/3 the phase diagram exhibits a two phase region between the heterosite end member and this intermediate ordered phase.

Chapter 2

Polaron models

2.1 Overview

The concept of polaron formation was first proposed in a 1933 manuscript by Lev Landau [27]. Landau put forward the idea that an extra electron will inevitably self-trap in an ionic lattice. In an inversion of the Born-Oppenheimer approximation, the surrounding ions adjust their positions in such a way as to lower the potential energy of the excess charge. If these displacements produce a sufficiently deep potential well, the carrier becomes bound. Polaron formation is energetically stable when the localized carrier's binding energy exceeds the strain energy expended in displacing the surrounding nuclei. Once trapped, the carrier can only move if the local distortion travels with it, resulting in a slow moving particle with a large effective mass. The resulting "polaron quasiparticle" is composed of the carrier plus this locally-induced distortion. The quasiparticle is referred to as a "small polaron" when the spatial extent of the carrier's wavefunction is on the order of the separation between ions or molecules in the structure. In contrast, a "large polaron" extends over several unit cells. The work in this thesis is confined to the study of small-polaron motion. Large polarons exhibit many different properties than small polarons, and while not the focus of this thesis, are themselves an active topic of research.

Small polaron theory is a large subfield of condensed matter physics. A combined effect of narrow bands and strong electron-phonon coupling, small polarons are observed in a wide range of materials including transition-metal oxides, molecular crystals, mantle minerals, rare gas solids, fullerenes, high-Tc superconductors, and various glasses. At elevated temperature, small polarons

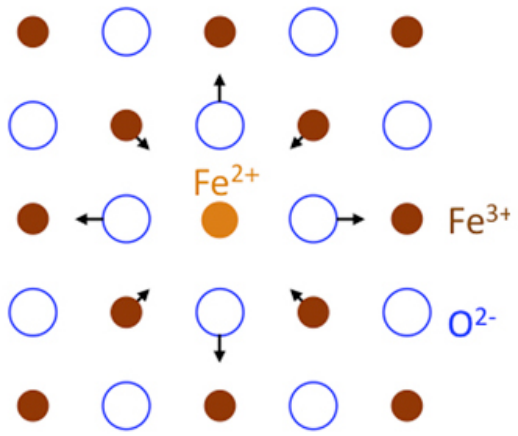

Figure 2.1. An electron polaron localized in an iron oxide lattice. Shifts of surrounding ion cores are shown with arrows. Image Courtesy of Pacific Northwest National Laboratory.

move by thermally-activated hopping, having a low mobility that rises with increasing temperature. This contrasts with the behavior of conventional free carriers that have a mobility that tends to fall off with temperature.

2.2 Holstein's molecular crystal model

In 1959 Theodore Holstein published two seminal papers about polaron localization and mobility [1, 28]. The first introduces the general theory of his molecular crystal model, and the second addresses the small polaron more specifically. This work provides the framework upon which much of later polaron theory is based. Holstein's model is essentially a tight-binding treatment of an excess electron in a one-dimensional chain of diatomic molecules. While this molecular crystal model pertains to an idealistically simple system, it captures the essential physics of small polaron formation and dynamics and illustrates the presence of two distinct temperature regimes. At low temperatures, the small polaron carriers are in band states. Because an excess carrier can self trap at any crystallographically equivalent ion site, the polaron can occupy Bloch states. This is not unlike semifree carriers, the difference being that the energy of the polaron band is many orders of magnitude smaller than the band for a free electron, typically far less than 1 meV. Above a threshold temperature, the energy uncertainty of these states exceeds their bandwidth, and the Bloch-type model breaks down. Above this temperature the polaron states are best treated as localized and the

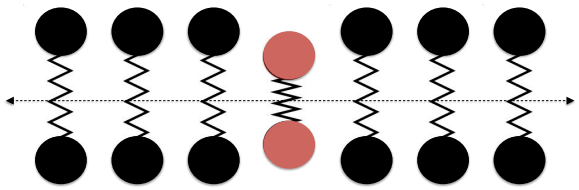

Figure 2.2. Holstein's Molecular Crystal Model. Here an excess electron is localized on the central diatomic molecule, depicted in red.

carrier mobility becomes diffusive, similar to the motion of light ions in a crystal. The following discussion will introduce the underlaying assumptions of the molecular crystal model and present the relevant results. For a full treatment of the Holstein model, readers are referred to the original 1959 manuscripts.

In its simplest form, the molecular crystal model describes the motion of a single electron (or hole) in a one-dimensional chain of deformable diatomic molecules, shown in Fig. 2.2. Each molecule has a fixed orientation and center of gravity and is specified with a position $\mathbf{R}_n = n\mathbf{a}$, an internuclear distortion variable, x_n, and a reduced mass M, where $M^{-1} = N^{-1}\sum_{\text{ions}} m^{-1}$. Here the distortion variable represents the deviation of the internuclear separation from its equilibrium position and $\mathbf{a}$ is the one-dimensional unit lattice vector. Within this model, a "lattice vibration" consists of a breathing mode in the individual internuclear separation (x_n) of the nth molecule, which affects the electron through a molecular potential $U(\mathbf{r} - \mathbf{R}_n, x_n)$. Here the electron-phonon interaction is established through the dependence of this potential of the distortion variable, x_n.

2.3 Semiclassical treatment of the molecular crystal model

Allowing for one vibrational degree of freedom per molecule, the positive strain energy is quadratic in the x_n (e.g., the interatomic separation of two ions in a diatomic molecule) with harmonic oscillator frequency, ω_0, associated with the configurational coordinate of an isolated molecule. The energy is reduced linearly with x_n in proportion to the strength of an electron-phonon interaction parameter, A, that characterizes the electron-lattice coupling strength in units of force.

$$E = \frac{1}{2}M\omega_0^2 x_n^2 - A(x_n - x_0). \tag{2.1}$$

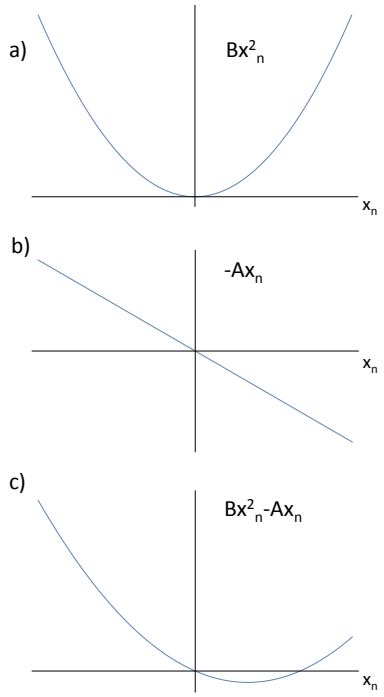

Figure 2.3. Energy of molecule as a function of distortion coordinate, x_n. Here $B \propto M\omega_0^2$.

Minimizing this energy gives,

$$\begin{aligned} E_0 &= Ax_n - E_b, \\ E_b &= \frac{A^2}{2M\omega_0^2}. \end{aligned} \tag{2.2}$$

Fig. 2.3 illustrates how a combination of the electronic and strain terms can give rise to a bound state. For $E_b > Ax_n$, a stable, self-trapped polaron will form. Once trapped, the carrier can move by hopping to a neighboring site. To hop, the energy of the carrier must be equivalent on adjacent sites. This condition is fulfilled when the distortions x_n and x_{n+1} of the initial and final sites are identical. If this distortion pattern is produced through thermal vibrations of the molecules, the carrier has the potential to transfer. Fig. 2.4 illustrates how electron transfer might occur through the development of a coincidence condition on a 1D chain. The transition is called adiabatic if given the development of this coincidence condition, the carrier will always transfer. Alternatively, if the carrier has a small chance of transfer despite the coincidence condition, the transition is termed non-adiabatic. At elevated temperature polarons travel through the crystal via thermally activated

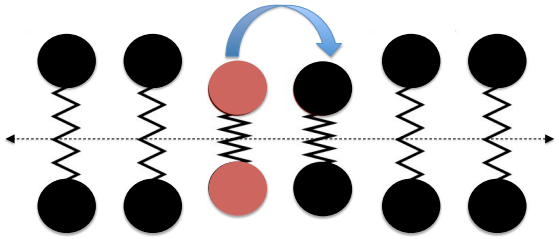

Figure 2.4. Depiction of polaron hop between adjacent sites on 1D chain illustrating the development of a coincidence event allowing for electron transfer.

hopping transitions, giving a mobility,

$$\Gamma \propto P \exp(-E_a/k_B T), \tag{2.3}$$

where $P = 1$ for adiabatic hopping and $P < 1$ for non-adiabatic hopping. The activation energy, E_a, is on the order of half the polaron binding energy, E_b. This type of hopping conduction is limited to elevated temperatures. Below a threshold temperature, the zero point energy allows for band-like tunneling between pairs of molecules .

2.4 The Holstein Hamiltonian

The total Hamiltonian of the molecular crystal system is composed of an electronic component, an electron-lattice interaction component, and a lattice component. The electron-lattice interaction, H_{int}, is a function the electron coordinate as well as the lattice displacements.

$$\begin{aligned} H =& H_{el} + H_{int} + H_{latt}, \\ & H_{el} + H_{int} = -\frac{\hbar^2}{2M}\nabla^2 + \sum_{n=1}^{N} U(\mathbf{r} - \mathbf{R}_n, x_n), \\ & H_{latt} = \sum_{n=1}^{N} \left(-\frac{\hbar^2}{2M}\frac{\partial^2}{\partial x_n^2} + \frac{1}{2}M\omega_0^2 x_n^2 + \frac{1}{2}M\omega_1^2 x_n x_{n+1} \right). \end{aligned} \tag{2.4}$$

The final term $(x_n x_{n+1})$ couples nearest neighbors, giving rise to dispersion of the vibrational frequencies. Proceeding with a typical tight-binding approach, the total wavefunction is built from a

linear superposition of molecular wavefunctions,

$$\Psi = \sum_n a_n(x_1, x_2...x_n)\phi_n(\mathbf{r}, x_n), \tag{2.5}$$

where the one-electron wavefunctions, $\phi_n(\mathbf{r}, x_n)$, constitute an orthonormal set and individually satisfy Schrödinger's equation for an isolated molecule,

$$\left[-\frac{\hbar^2}{2M}\nabla^2 + U(\mathbf{r} - \mathbf{R}_n, x_n)\right]\phi_n(\mathbf{r}, x_n) = E(x_n)\phi_n(\mathbf{r}, x_n). \tag{2.6}$$

The constituent wavefunctions, ϕ_n, are each localized about a particular molecular site and depend on the internuclear distortion variable of that molecule. Holstein assumed the eigenvalues, describing the energy of an electron on an isolated molecule, depend linearly on x_n,

$$E(x_n) = -Ax_n. \tag{2.7}$$

Equations for $a_n(x_1, x_2...x_n)$ are derived using a time-dependent Schrödinger equation, making use of customary tight binding approximations,

$$i\hbar\frac{\partial}{\partial t}a_n(x_1, x_2...x_n) = [H_{latt} - Ax_n]a_n(x_1, x_2...x_n) + \sum_{\pm} J(x_n, x_{n\pm1})a_{n\pm1}(x_1, x_2...x_n), \tag{2.8}$$

where J is the two-center overlap integral,

$$J(x_m, x_n) = \int \phi^*(\mathbf{r} - \mathbf{R}_m, x_m)U(\mathbf{r} - \mathbf{R}_m, x_m)\phi(\mathbf{r} - \mathbf{R}_n, x_n)d\mathbf{r}. \tag{2.9}$$

If in Eq. 2.8 the internuclear distortion variables are all fixed at single value, x, the molecular crystal model becomes no different from the standard tight-binding solution with a degenerate set of localized wavefunctions giving Bloch wave expansion coefficients,

$$a_n = e^{ikn}, \tag{2.10}$$

and an energy band,

$$E_k = E(x) + (N/2)M\omega_0^2x^2 - 2J\cos(k), \tag{2.11}$$

where J has been set equal to a negative constant.

2.5 Adiabatic electron transfer

For adiabatic electron transfer, the Hamiltonian describes a carrier traveling through nuclei whose positions are effectively fixed. In the adiabatic case, the electronic overlap energy J exceeds the phonon energies and electron transfer will invariably occur when the phonon displacements bring the nuclei into a coincidence position. As a result, the terms in Eq. 2.4 involving derivatives of the electron wavefunctions with respect to nuclear distortion coordinates, x_n, are dropped and the Hamiltonian reduces to,

$$H = -\frac{\hbar^2}{2M}\nabla^2 + \sum_{n=1}^{N} U(\mathbf{r} - \mathbf{R}_n, x_n) + \sum_{n=1}^{N}\left(\frac{1}{2}M\omega_0^2 x_n^2\right). \tag{2.12}$$

Neglecting the lattice coupling terms, Eq. 2.8 can be written,

$$\left(\frac{1}{2}\sum_{n=1}^{N} M\omega_0^2 x_n^2 - Ax_n\right) a_n - J(a_{n+1} + a_{n-1}) = E(x_1, x_2 ... x_n) a_n. \tag{2.13}$$

There are two different types of solutions to Eq. 2.13. The first is the band-type solution,

$$\begin{aligned} a_n &= e^{ikn}/N^{1/2}, \\ E(x_1^{(0)}, x_2^{(0)} ... x_n^{(0)}) &= -2J + Jk^2, \end{aligned} \tag{2.14}$$

where $(x_1^{(0)}, x_2^{(0)} ... x_n^{(0)})$ are the distortion coordinates that minimize the energy. A second localized solution to Eq. 2.13 is solved using a perturbation expansion in powers of J. To first order, it can be shown that the polaron binding energy becomes

$$E_P = \frac{A^2}{2M\omega_0^2} - 2J. \tag{2.15}$$

It is apparent the quantity $A^2/2M\omega_0^2$ represents the maximum polaron binding energy, in the limit of infinitely narrow polaron bandwidth ($J = 0$). The first term in Eq. 2.15 is half of the polaron binding energy derived in Eq. 2.2. Furthermore, the adiabatic case results in a transition probability

between localized states per unit time,

$$W = \frac{\omega_0}{2\pi} \exp^{-(E_b/2-J)/k_B T}, \tag{2.16}$$

where the activation barrier is half the polaron binding energy and the pre-exponential factor is a characteristic vibrational frequency.

2.6 Non-adiabatic electron transfer

This adiabatic treatment is no longer valid for systems in which the electronic overlap J is sufficiently small. When the electronic bandwidth ($2J$) is small compared to a characteristic energy,

$$2J < \frac{A^2}{2M\omega_0^2}, \tag{2.17}$$

it becomes appropriate to treat J as a perturbation. For the zeroth-order solution (J=0), the carrier is localized to a site and the energies become,

$$\begin{aligned} E^0(N_q) &= \epsilon_n(0) + E_b + \sum_q \hbar\omega_q \left(N_q + \frac{1}{2}\right), \\ E_b &\sim -\frac{1}{N}\sum_q \frac{A^2}{2M\omega_q^2}. \end{aligned} \tag{2.18}$$

In the derivation of Eq. 2.18 the x-dependence of the electronic overlap integrals is neglected and all Js are reduced to a single constant. The quantity $\epsilon_n(0)$ pertains to the energy of the carrier at site n in a rigid lattice and N_q is the phonon occupation number of the qth normal mode with frequencies given by the dispersion relation,

$$\omega_q^2 = \omega_0^2 + \frac{\omega_1^2}{2}\sum_n \cos(q). \tag{2.19}$$

Here $q = 2\pi j/N$, the integer j taking values between $\pm N/2$. The second term in Eq. 2.18 is analogous to the polaron binding energy in Eq. 2.2.

Including a non-zero overlap integral gives rise to fundamental differences in the high and low temperature behaviors. Applying first-order perturbation theory, it can be shown that as the temper-

ature goes to zero the energies become,

$$\begin{aligned} E(k, N_q) &= E^0(N_q) - 2J\cos(k)\exp\left[-S(N_q)\right], \\ S(N_q) &= \frac{1}{N}\sum_q (1+2N_q)\left(\frac{A^2}{2M\omega_q^2\hbar\omega_q}\right)(1-\cos(q)). \end{aligned} \tag{2.20}$$

Here S is related to the overlap between the harmonic oscillator wavefunctions on adjacent sites. Within this limit, transitions involving changes in the phonon occupancy of the system ($N_q \neq N_q'$) are negligible. This low temperature solution describes a polaron band with a bandwidth that depends on the vibrational quantum numbers through S,

$$\Delta E(N_q) = 2J\exp[-S(N_q)]. \tag{2.21}$$

Assuming a thermal average, $\langle N_q \rangle = 1/(\exp(\omega/k_BT) - 1)$, the bandwidth is maximum at absolute zero and shrinks exponentially with rising temperature.

Above a certain threshold, the polaron bandwidth becomes so small that this band picture breaks down, and a localized description becomes more appropriate. At these temperatures, transitions where the initial and final vibrational quantum numbers are changed become dominant. The crossover between low temperature band conduction and high temperature hopping behavior occurs when the inverse lifetime of the polaron band states becomes small compared to the bandwidth. This generally occurs at a temperature, $T_t \sim \hbar\omega_0/2k_B$. The crossover between these two temperature regimes is shown in Fig. 2.5. Above this threshold, the so called 'diagonal' transitions, where $N_q = N_q'$, are negligible compared to transitions where $N_q \neq N_q'$. A full treatment of these 'non-diagonal' transitions using standard perturbation theory gives the transition probability between localized states per unit time [29]. In the high temperature limit, $\hbar\omega_0/k_BT << 1$, this probability reduces to,

$$W(p, p\pm 1, T) = \frac{J^2}{\hbar}\left(\frac{\pi}{4k_BTE_a}\right)^{1/2}\exp^{-E_a/k_BT}, \tag{2.22}$$

where Ea is the activation energy for carrier hopping,

$$E_a = \frac{1}{2N}\sum_q \frac{A^2}{2M\omega_q^2}(1\cos(q)) \sim \frac{1}{2N}\frac{A^2}{2M\omega_0^2} = E_b/2. \tag{2.23}$$

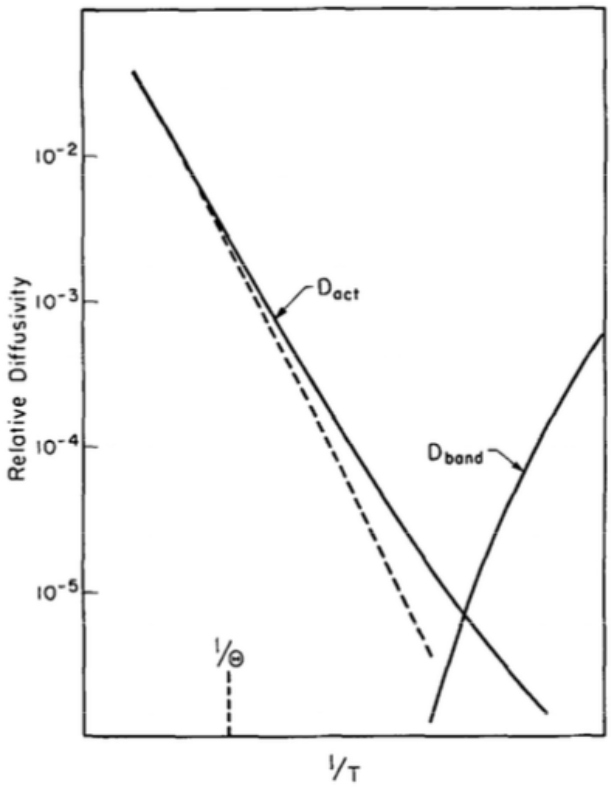

Figure 2.5. Depiction of crossover between low temperature, band conduction and elevated temperature Arrhenius-type behavior. Here the dotted line illustrates an Arrhenius fit to the high temperature result. Here θ is the characteristic temperature given by $\theta_0 = \hbar\omega_0/k_B$. Figure from Holstein (1959) [1].

The temperature dependence of 2.22 is characteristic of an activated process with an activation barrier for polaron hopping between adjacent sites of E_a.

Chapter 3

The activation volume

3.1 Overview

Electron transfer between adjacent sites in a crystal lattice occurs in an environment that is macroscopically at constant pressure. Accordingly, the activation barrier is best described in terms of an activation enthalpy that can be broken down into an energy component plus a volume dependent term,

$$H_a = E_a + PV_a. \tag{3.1}$$

The activation energy, E_a, describes the energy barrier for polaron transfer between adjacent sites and the second term quantifies the pressure effect on the activation barrier, giving the extra energy cost due to the finite volume change in the activated state. The activation volume, V_a, can be interpreted physically as the local change in volume as the particle moves through its transition state. V_a can be either positive or negative, indicating a local expansion or contraction of the lattice, respectively. Fig. 3.2 illustrates a possible sequence of events for a polaron hop on a one-dimensional chain. The second frame displays the development of a transient distortion pattern that facilitates electron transfer and illustrates the volume change in the activated state. In this case, the chain undergoes a local dilation, indicating a positive activation volume.

Accounting for the theoretical details of the last chapter, a general expression for the polaron

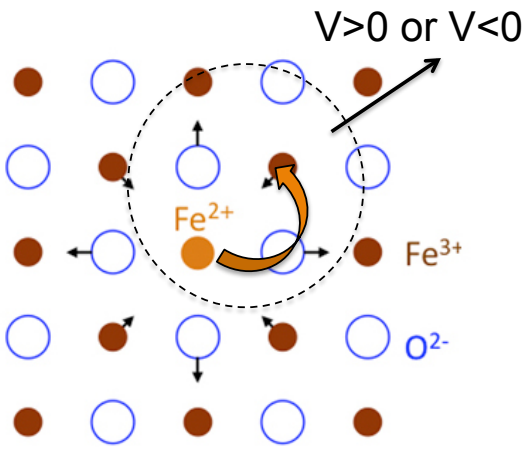

Figure 3.1. Illustration of the local lattice expansion or contraction that occurs during charge transfer process. Image Courtesy of Pacific Northwest National Laboratory.

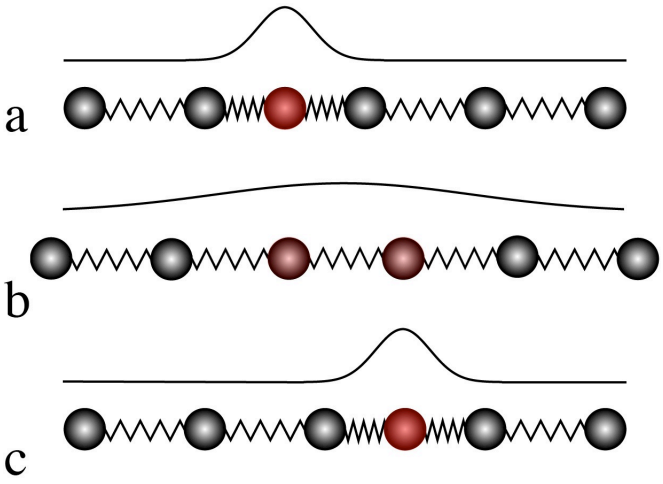

Figure 3.2. Depiction of polaron hop between adjacent sites on 1D chain, illustrating the development of a transient distortion pattern that allows for electron transfer and shows the local volume change in the transition state. a) Polaron localized on left site. b) Activated state during electron transfer, illustrating a local expansion of the lattice. c) Carrier localized on right site.

hopping rate can be expressed as,

$$\Gamma(P,T) \sim \frac{\Gamma_0}{T^n} \exp\left(-\frac{E_a + PV_a}{k_B T}\right), \tag{3.2}$$

where n=1/2 in the nonadiabatic case and n=0 for adiabatic case of concern here. Accordingly, measurements of the temperature dependance of the polaron hopping rate allow for the determination of the overall activation barrier. Measurements of the activation volume require the ability to alter the pressure of the system and gauge any effect on the activation barrier. For a positive activation volume, there is local expansion in the activated state and pressure will tend to suppress the polaron hopping rate. Conversely, a negative activation volume describes a local lattice contraction during electron transfer, in which case applying pressure will tend to enhance the polaron hopping rate. Activation volumes are usually reported using either cm^3/mol or in Å^3. As the later is more intuitive, this convention will be used from here on out.

3.2 Previous polaron activation volume measurements

The importance of the activation energy for understanding the kinetics of hopping type mobility is well established and there have been numerous studies looking at activation energies in polaronic systems. Meanwhile, measuring activation volumes remains largely unexplored. Despite the wealth of potential information these type of studies could provide, the experiments tend to be challenging. Historically there have been a handful of high pressure conductivity studies, mostly focusing on electrical transport measurements of minerals. These high pressure conductivity measurements are tricky and sorting out issues that arise due to pressure effects on the electrical contacts is not trivial. Recent improvements in tools for high pressure measurements are opening up high pressure work to different scattering techniques and expanding the availability of sample environments. With these advances, this topic is becoming increasingly accessible. In particular, nuclear resonant scattering is a technique that allows for a direct measure of the polaron hopping rate and can be extended to high pressures using synchrotron nuclear forward scattering in an externally heated diamond anvil cell.

The majority of experimental reports of activation volumes are from the geophysical literature. These studies generally address the high-pressure conductivty of iron-bearing mantle minerals in-

cluding perovskite-(Mg,Fe)SiO_3, olivine-(Mg,Fe)$_2SiO_4$, and magnesiowüstite-(Mg,Fe)O [30–33]. In these systems, the concentration of polarons is related to the concentration of vacancies and to oxygen partial pressure. Geophysical models as well as magnetotelluric and geomagnetic deep sounding methods give credence to a theory of a lower mantle layer with enhanced conductivity [34]. Consequently, understanding the electronic properties of minerals at elevated pressures and temperatures is relevant to constraining the chemistry profile of the mantle. These measurements of electrical transport properties of oxides under applied pressure gave small, negative values for V_a of a few tenths of a cubic angstrom. This is often interpreted in terms of better overlaps of electron wavefunctions when the ions are pushed closer together. Authors have gone so far as to suggest that a small, negative activation volume is inherent to polaron conduction [35]. This metric has been used to distinguish between ionic conduction and polaron conduction, where it is accepted that values of V_a for ionic mobility are larger and positive by comparison [30].

3.3 Corrections to the apparent activation volume

The activation barrier sets the temperature dependence of the polaron hopping rate. The activation volume is defined in terms of the pressure dependance of this activation barrier,

$$V_a = \left(\frac{\partial H_a}{\partial P}\right)_T. \tag{3.3}$$

Activation volumes are usually determined by performing a temperature series of a measurement that relates to the polaron hopping rate for a set number of fixed pressures in order to identify any shift in activation barrier with pressure. Consequently, the activation barrier is commonly defined as,

$$V_a \approx -k_B T \frac{\partial \ln \Gamma(P,T)}{\partial P}. \tag{3.4}$$

As the majority of activation volume data are from conductivity measurements, V_a is often expressed in terms of the electrical conductivity, in which case the polaron hopping rate, $\Gamma(T,P)$, in Eq. 3.4 is replaced with the conductivity, $\sigma(P,T)$.

Equation 3.4 assumes the prefactor in Eq. 3.2 does not depend on volume. While most studies use Eq. 3.4, it is possible that both the exponential term and the prefactor could exhibit a pressure

dependence. If this is the case, correction terms must be added to "apparent activation volume," defined in Eq. 3.4. It is also possible that there is an entropic contribution to the activation barrier. As a result of the inverse temperature dependance of the exponential in Eq. 3.2, any entropic contribution results in a constant term that is absorbed into the prefactor. The activation volume defined in Eq. 3.4 is only rigorously correct if the pressure dependance of this entropic term is negligible. Furthermore, depending on the experimental technique used to determine the polaron hopping rate, other pressure dependent terms can enter the prefactor as well.

For adiabatic electron transfer, the prefactor in Eq. 3.2 reduces to a characteristic phonon frequency. Recasting the expression for the adiabatic polaron hopping rate defined in Eq. 2.16 gives an activation volume,

$$V_a = -k_B T \frac{\partial \ln \Gamma}{\partial P} + k_B T \frac{\partial \ln \omega_0}{\partial P}. \tag{3.5}$$

It is straightforward to show that the final term can be rewritten in terms of a Grüneisen parameter and a compressibility,

$$V_a = -k_B T \frac{\partial \ln \Gamma}{\partial P} + k_B T \gamma \kappa_T. \tag{3.6}$$

Assuming a typical Grüneisen parameter $\gamma \sim 2$, a bulk modulus of 150 GPa, and a temperature of 300 K, the final term in Eq. 3.6 is on the order of 0.06 Å^3. This term can be understood as an enhancement of the polaron hopping rate due to pressure induced stiffening of the lattice, resulting in an overall reduction of the the apparent activation volume. This correction must be added to a volume determined using Eq. 3.4 to ascertain the true value of V_a.

For nonadiabatic hopping, the prefactor depends on the square of the overlap integral, J. The pressure dependence of the overlap integral can be estimated using an inverse localization length, α, describing the spatial extent of the wavefunction,

$$J = J_0 \exp^{-\alpha R}, \tag{3.7}$$

where R is the distance between two sites. Substituting Eq. 3.7 into the adiabatic polaron hopping rate defined in Eq. 2.16 gives an activation volume,

$$V_a = -k_B T \frac{\partial \ln \Gamma}{\partial P} + k_B T (2\alpha R_0 \kappa_T / 3), \tag{3.8}$$

where the pressure dependence of J arises from the reduction of the inter-site distance with pressure,

$$R = R_0(1 - P\kappa_T/3), \tag{3.9}$$

and the inverse localization length is assumed to be pressure independent. Taking $\alpha R_0 = 2$, this correction term becomes $\sim 0.04\,\mathring{A}^3$. Similar to the nonadiabatic correction, this factor must be added to the experimentally determined activation volume, derived from the pressure derivative of the polaron hopping rate.

Generally, for localized electrons, $\alpha > 1/R$. However, placing an upward bound on the inverse localization length is not straightforward without resorting to electronic structure calculations. Even in cases where calculated electronic density information is available, it is well known that density functional theory fails to accurately model strongly localized states, where self-interaction errors become important. Before the widespread availability of first principles calculations, predictive estimates of wavefunction overlap were often used to explain observations related to electronic structure.

In his "Solid State Table of the Elements," Walter Harrison developed a suite of approximation tools, providing parameters that allow for simple calculations of a range of material properties [36]. Using Harrison's method for approximating wavefunction tails, the overlap integral for d-type wavefunctions goes as the inverse 5th power of the site separation,

$$J \propto J_0/R^5. \tag{3.10}$$

Substituting this overlap approximation into Eq. 2.16 results in an activation volume,

$$V_a = -k_B T \frac{\partial \ln \Gamma}{\partial P} + k_B T \frac{10 k_T}{3 - \kappa_T P}. \tag{3.11}$$

For pressures of of $0-10$ GPa, the final term raises the activation volume by an $\sim$0.09 $\mathrm{\AA}^3$, giving a slighter larger result than the previous overlap approximation, with Eq. 3.8. In both cases, this factor represents an enhancement of the polaron hopping rate, due to the enlargement of the prefactor from

increased wavefunction overlap. The result is an overall shift to a lower apparent activation volume,

$$-k_BT\frac{\partial \ln \Gamma}{\partial P} \approx \frac{\partial H_A}{\partial P} - k_BT(2\alpha R_0\kappa_T/3) \approx \frac{\partial H_A}{\partial P} - k_BT\frac{10k_T}{3-\kappa_T P}. \tag{3.12}$$

For cases where the pressure shift of the enthalpy is small, this factor can be responsible for the observation of negative activation volumes.

Another commonly used expression for the polaron hopping rate is the Mott conductivity equation, originally developed to treat hopping conduction in transition-metal-containing glasses [37]. Given certain approximations of prefactor terms, this treatment is essentially equivalent to nonadiabatic Holstein model. That said, as this formalism is frequently adopted for experimental data analysis, it is treated separately here. Within this model, the expressions for the polaron hopping rate and the activation volume become,

$$\Gamma(T,P) = \omega_0 \exp^{-2\alpha R} \exp\left(\frac{E_a + PV_a}{k_BT}\right), \tag{3.13}$$

$$V_a = -k_BT\frac{\partial \ln \Gamma}{\partial P} + k_BT(2\alpha R_0\kappa_T/3) + k_BT\gamma\kappa_T. \tag{3.14}$$

Applying the same approximations as above, it can be shown at 300 K that the last two terms of the right hand side of Eq. 3.14 sum to ~ 0.1 Å^3.

Despite the aforementioned challenges associated with high pressure conductivity measurements, bulk transport measurements remain the most common method to study activation volumes. While conductivity data are clearly pertinent to the performance in an electrode material, these measurements are not a direct measure of the local polaron hopping rate, $\Gamma(P,T)$. The Nernst-Einstein equation relates the conductivity to the mobility of the moving species,

$$\sigma = \frac{cq^2}{k_BT}D, \tag{3.15}$$

where q is the polaron charge, c is the concentration and D is the diffusivity. Furthermore, the conductivity is related to the polaron hopping rate,

$$\sigma = \frac{e^2}{k_BT}c(1-c)R^2\Gamma(T,P), \tag{3.16}$$

accounting for dependence of the polaron diffusivity on the average number of surrounding open sites as well as the jump distance between sites. The additional factor R^2 in the prefactor of Eq. 3.16 gives rise to an additional correction factor,

$$-k_B T \frac{\partial \ln \sigma}{\partial P} = -k_B T \frac{\partial \ln \Gamma}{\partial P} + k_B T \left(\frac{2\kappa_T}{3 - P\kappa_T} \right). \tag{3.17}$$

Again, assuming pressures of of $0-10$ GPa, a temperature of 300 K, and a bulk modus of 150 GPa, this correction factor is $\sim 0.02\,\mathring{A}^3$.

3.4 Pressure dependence of the Holstein activation barrier

While the molecular crystal model does not explicitly account for any volume dependence, an examination of the pressure shift of the Holstein activation barrier can lead to pertinent physical insights. As detailed in the preceding chapter, for adiabatic polaron hopping at elevated temperature, the activation barrier in the Holstein model becomes,

$$E_a = E_b/2 - J = \frac{A^2}{4M\omega_0^2} - J, \tag{3.18}$$

where A is an electron-phonon coupling term, M is the reduced mass of the molecule, ω_0 is characteristic phonon frequency, and J is the overlap integral. For nonadiabatic hopping, Eq. 3.18 reduces to half the polaron binding energy, E_b. A pressure derivative of Eq. 3.18 gives,

$$\frac{\partial E_a}{\partial P} = E_b \left(\frac{\partial \ln A}{\partial P} - \frac{\partial \ln \omega_0}{\partial P} \right) - \frac{\partial J}{\partial P}. \tag{3.19}$$

Using Harrison's approximation for the overlap integral Eq. 3.19 can be expressed,

$$\frac{\partial E_a}{\partial P} = E_b \left(\frac{1}{A} \frac{\partial A}{\partial P} - \gamma \kappa_T \right) - \frac{5}{3} \kappa_T J. \tag{3.20}$$

Unlike the correction terms discussed in previous section that arose from pressure effects on the prefactor, the terms in this expression are a result of the pressure dependence of the activation barrier itself. From the first term, it can be seen that a fractional enhancement of the electron-phonon coupling with pressure will give rise to a positive term in the activation volume. The final

term, due to the enhancement in wavefunction overlap, is often cited as the source of negative polaron activation volumes.

3.5 Activation volume for ion diffusion

The topic of activation volumes for ion diffusion has received more attention than the polaron counterpart. Similar to polaron mobility, ion diffusion in solids is treated as a thermally activated process with an Arrhenius-type mobility. The ionic activation volume is associated with a change in material volume associated with the migration of an ion. The pressure dependence of ionic conductivity gives information about the volume relaxation associated with the formation and motion of defects. Although there are reports of some superionic conductors having negligible or even negative activation volumes, the vast majority of conventional ionic conductors exhibit a strong suppression of ionic mobility with pressure, giving activation volumes ranging from $+1 to +10\,\text{Å}^3$ [38]. Applying a simple hard-sphere model, the migration volume is roughly equivalent to the volume of the diffusing species. However, experimentally determined activation volumes are usually significantly smaller than this model would imply. Several more sophisticated models assume the free energy for ion migration can be attributed to the strain energy of the lattice. Treating the surrounding crystal as a continuous medium, the activation volume scales with the lattice compressibility.

Chapter 4

Methods

4.1 Synchrotron x-ray diffraction

X-ray diffraction (XRD) is a powerful technique for determining crystal structures. The spectral brilliance of synchrotron x-rays allows for the study of small samples confined in a diamond-anvil cell. In addition, the high intensity of a synchrotron beam provides sufficient resolution to resolve weak superstructure peaks that would be difficult to observe with a typical lab-diffractometer. Using a two-dimensional CCD detector, a full pattern can be collected in matter of seconds. Angular dispersive XRD patterns are collected in transmission mode using a monochromatic synchrotron beam and a MAR CCD detector. The raw data appear as a set of rings centered around the beam

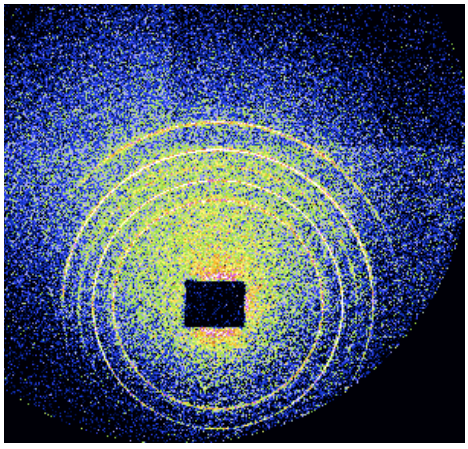

Figure 4.1. Typical 2D image file collected with CCD detector.

stop, with radii related to the crystallographic d-spacings through Bragg's law,

$$\lambda = 2d\sin(\theta), \tag{4.1}$$

where θ is a quarter of the diffraction-cone angle. A typical CCD image is shown in Fig. 4.1. A diffraction pattern from a CeO_2 sample calibration is collected to establish the distance between the detector and the sample. To transform the image file into typical one-dimensional diffraction, data in the images are integrated azimuthally using the Fit2D package [39]. The data can then be analyzed to study the crystal structure of the material.

4.2 X-ray diffraction data analysis

Rietveld analysis of the synchrotron x-ray data was performed to obtain information on phase fractions and thermal trends of lattice parameters. Given starting structural information, Rietveld programs calculate a model diffraction pattern, then proceed to iteratively optimize this model by minimizing the difference between the fit and the experimental data. The iterations refine experimental parameters such as background, peak broadening and lattice constants. This type of refinement requires a reasonably accurate starting structure, and while the method is powerful for honing in on precise structural details, if the crystal structure is not known, it will not be possible to solve for it. Given a starting structure, Rietveld refinement allows for accurate determination of unit cell parameters, strain broadening effects, and qualitative phase analysis. The method is particularly useful for the evaluation of powder patterns with overlapping peaks.

Rietveld analysis was performed using the General Structure Analysis System (GSAS) [40,41]. A shifted Chebyschev polynomial was used to fit the background, including between four and six terms as needed. To capture accurate peak shapes, the fit model employed psedo-Voigt profile functions. For all samples, both Gaussian and Lorentzian crystallite size broadening were assumed to be negligible. As low angle data was not considered, profile terms related to axial-divergence were not included. The angular dependence of the Gaussian variance is set by the Cagliotti Function,

$$\sigma^2 = U\tan^2\theta + V\tan\theta + W. \tag{4.2}$$

It was assumed that the instrumental broadening was primarily Gaussian. As such, the Cagliotti terms (U, V,W) were determined from a refinement of a CeO_2 standard and fixed for all additional refinements.

Strain broadening effects were treated as entirely Lorentzian. To reproduce accurate profiles, anisotropic strain broadening had to be accounted for, where peak broadening varied by reflection class. To reproduce this anisotropy, profile terms based on Stephen's anisotropic strain model were included [42]. Within this semi-empirical model, the strain components are restricted in terms of the first and second order terms allowed by lattice symmetry. For an orthorhombic cell this gives rise to six independent strain terms,

$$\Gamma_S^2 = S_{400}h^4 + S_{040}k^4 + 3(S_{200}h^2k^2 + S_{202}h^2l^2 + S_{022}k^2l^2). \tag{4.3}$$

When possible, these anisotropic strain broadening terms were fixed for each phase and not allowed to vary for patterns collected at different temperatures. In cases where this did not produce good fits, the terms were refined with strong"damping", such that only a small fraction of the shift is applied. In this case, the temperature evolution of the strain terms were carefully monitored to ensure the trends were physically reasonable. The refinement of strain terms was only necessary when handling the precipitation of a secondary phase. At low temperature, the phase fraction of the second phase is low and the effects of strain broadening are readily apparent. As the temperature is raised and the fraction of the new phase increases, strains are relaxed and the magnitude of the strain terms falls off. Having established physically reasonable and reasonably reproducible profile terms, the phase fractions as well as the lattice parameters can be refined. This allows for a study of the phase stability as well as the thermal expansion.

4.3 Mössbauer spectrometry

4.3.1 The Mössbauer effect

The Mössbauer effect describes the recoil-free absorption and emission of a γ-ray by atoms in a solid. The γ-ray emission that accompanies the decay of a radioactive nuclei in an excited state has the potential to excite other similar nuclei. For free nuclei, the efficiency of this process is severely

limited by the nuclear recoil during both the emission and absorption processes. As a result, the energy of the emitted γ-ray is reduced by the kinetic energy of recoil of a free nucleus E_R,

$$E_R = \frac{E_\gamma^2}{2Mc^2} \sim 2\,\mathrm{meV}, \tag{4.4}$$

where E_γ is the photon energy, M is the nuclear mass, and c is the speed of light. The linewidths of the nuclear excited states are remarkably precise, on the order of 10^{-9} eV. The recoil of a free nucleus will prevent an emitted γ-ray from having an energy that falls in the tight window necessary to excite an additional nuclei. During his doctoral work, Rudolf Mössbauer recognized that this complication could be effectively circumvented if the recoil was absorbed by an entire crystal rather than a single nuclei. In this case the mass in Eq. 4.4 is enhanced by a factor equal to the number of atoms in the crystal and the recoil energy is inconsequential. This will be realized if the recoil energy is less than the energy of the lowest quantized mode of the crystal. Within the framework of the Debye model, the probability of a recoil free event is described by the Lamb-Mössbauer factor [43],

$$f = \frac{-6E_R}{k_B\Theta_D}\left[\frac{1}{4} + \left(\frac{T}{\Theta_D}\right)^2 \int_0^{\frac{\Theta_D}{T}} \frac{x}{\exp(x)-1}dx\right], \tag{4.5}$$

where k_B is Boltzmann's constant and Θ_D is the Debye temperature. To observe the Mössbauer effect, the recoilless fraction, f, must be large. In general this occurs when $\mathrm{E}_R << \hbar\omega_D$. Since the Lamb-Mössbauer factor depends on the γ-ray energy through, E_R, the probability of a recoil-free event is only appreciable for certain isotopes with low lying excited states. Fortunately this includes ^{57}Fe, making the Mössbauer effect useful for a wide range of studies of iron-bearing materials. In addition to iron, the Mössbauer effect has been observed in a wide range of isotopes, including but not limited to ^{151}Eu, ^{191}Ir and ^{119}Sn.

4.3.2 Hyperfine interactions

Recoilless γ-ray emission in ^{57}Fe occur between a nuclear ground state having spin I=1/2 and a 14.41 keV excited state, I=3/2. Electrons in the vicinity of the resonant nuclei can break rotational symmetry and perturb the energies of the nuclear states. Measurement of the nuclear transitions then serves as a probe to study the electronic environment of the resonant atom and its nearest neighbors. The isomer shift (IS) arises from a Coulomb interaction between the nuclear and electronic charge

distributions. The s-electron wave functions have a finite overlap with the nucleus, lowering the nuclear energy levels. The Coulomb interaction between the s-electron density and the nuclear charge causes an energy level shift,

$$\delta E = \frac{2}{3}\pi Z e^2 |\Psi(0)_S|^2 \langle R \rangle^2 , \tag{4.6}$$

where Z is the atomic number, $|\Psi(0)_S|$ is the s-electron density, and $\langle R \rangle$ is the mean-square radius of the nuclear charge distribution. Any difference in the s-electron density between the absorber and the emitter will give an overall shift in the observed resonance. The measured splitting becomes,

$$\delta E = \frac{2}{3}\pi Z e^2 (|\Psi(0)_A|^2 - |\Psi(0)_S|^2)(\langle R \rangle_E^2 - \langle R \rangle_G^2), \tag{4.7}$$

where the subscripts S, A, E and G refer to the source, absorber, excited and ground states respectively. Screening effects of the 3d electrons can reduce the electron density at the nucleus, thereby increasing the IS. Consequently, a ferrous ion will show an appreciably larger IS compared to a ferric ion in a similar environment. IS is a relative quantity and can only be determined in comparison to other materials or as a difference between two crystallographically distinct Fe sites within the same material.

The electric quadrupole splitting (QS) results from the interaction of the nuclear quadruple moment with an inhomogeneous electric field. The quadrupole moment, Q, describes the departure from spherical symmetry in the rest frame of the nucleus. For nuclei with spin quantum numbers I=0 or 1/2, the nuclei will have spherical symmetry and Q=0. A nucleus with a spin number I$>$1/2 will have a non-spherical charge distribution where Q$>$0 describes an oblate nucleus with respect to the spin axis, while Q$<$0 indicates a prolate nucleus. When a nonzero nuclear quadruple moment is exposed to an asymmetric electric field resulting from an asymmetric electronic environment, an electric quadrupole interaction results in the loss of degeneracy of the nuclear energy levels . The asymmetry of the electronic environment of the nuclei is characterized by the electric field gradient (EFG). The result of this interaction is a splitting of the nuclear energy levels corresponding to the different alignments of the quadruple moment with respect to the principal axes of the EFG tensor,

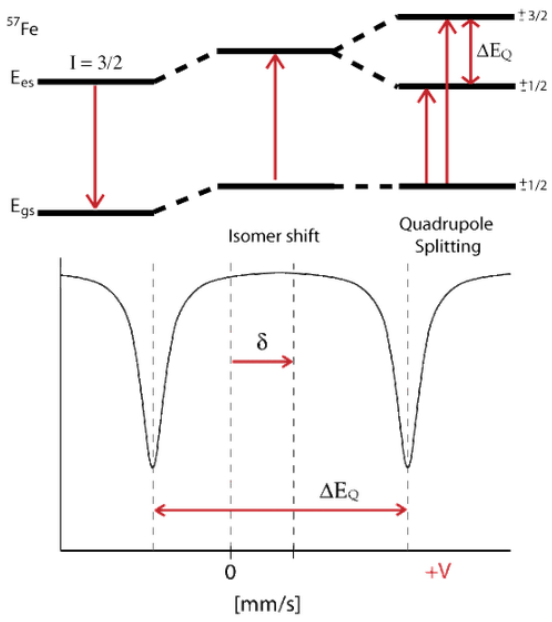

Figure 4.2. Energy diagram of isomer shift and quadrupole splitting, ΔE_Q, for the ^{57}Fe 3/2→1/2 transition in an asymmetric EFG. Figure: UC Davis ChemWiki- CC BY-SA 3.0.

V_{zz}. The eigenvalues of the Hamiltonian for the quadrupole interaction are,

$$E_Q = \frac{eQV_{zz}}{4I(2I-1)}[3m_I^2 - I(I+1)]\left(1+\frac{\eta^2}{3}\right)^{1/2}, \qquad m_I = I, I-1, \ldots -|I|, \tag{4.8}$$

where I is the nuclear angular momentum and η is the asymmetry parameter,

$$\eta = \frac{V_{xx} - V_{yy}}{V_{zz}}. \tag{4.9}$$

The result for ^{57}Fe is an excited state with two doubly degenerate sublevels corresponding to the $m =_I \pm 3/2$ and $m_I = \pm 1/2$ nuclear spin states. The energy splitting is given by,

$$\delta E = \pm\frac{1}{4}eQV_{zz}\left(1+\frac{\eta^2}{3}\right)^{1/2}. \tag{4.10}$$

As the nuclear quadruple moment is fixed, $Q \sim 0.16$ for the I=3/2 excited state of ^{57}Fe [44], the magnitude of the splitting gives information about the local electric field in the vicinity of the Mössbauer nuclei. Variation in QS between different Fe-bearing materials is caused by distinct EFG tensors arising from valance differences and changes in the local symmetry surrounding the

resonant ion.

4.3.3 Mössbauer measurements

The experimental set-up for a typical Mössbauer measurement involves a radioactive source, containing the resonant isotope in an excited state, and a sample, containing the resonant nuclei in the ground state. For measurements involving ^{57}Fe, the usual source is ^{57}Co embedded in a Rh matrix. ^{57}Co decays to a metastable ^{57}Fe state via electron capture which successively decays to the ground state by emitting a 14.4 keV photon. To study the hyperfine structure, the energy of the incident γ-ray must scan through a range that covers the spectral splittings. To modulate the energy, the source is moved relative to the absorber using Doppler drive. The γ-ray source is mounted on a mechanical transducer which oscillates back and forth giving a shifted energy,

$$E = \frac{v}{c} E_\gamma, \tag{4.11}$$

where v is the source velocity, E_γ is the 14.4 keV photon energy and c is the speed of light. The Mössbauer spectrum is collected by recording the transmitted photons as a function of source velocity. The resonant absorptions appear as dips in the spectrum with Lorentzian linewidths. The cross section for resonant absorption is described by the Breit-Wigner formula,

$$\sigma_a(E) = \frac{\sigma_0 \Gamma_a^2/4}{(E - E_0)^2 + \frac{1}{4}\Gamma_a^2}, \tag{4.12}$$

where σ_0 is the nuclear resonant cross-section and Γ_a is the line width of the excited state of the absorber. Similarly the emitted γ-rays from the source have a Lorentzian distribution around 14.4 keV with a linewidth, Γ_s. Given a sufficiently thin source and absorber, the observed resonance curve is simply a convolution of the two distributions, resulting in a Lorentzian curve with linewidth $\Gamma_s + \Gamma_a$. For the limiting case where both the source and observer have a natural linewidth, $\Gamma_n \sim 0.097$ mm/s, the observed resonance will have a linewidth of $2\Gamma_n$, where $\Gamma_n = \hbar/141$ ns, and 141 ns is the lifetime of the first nuclear excited state for ^{57}Fe.

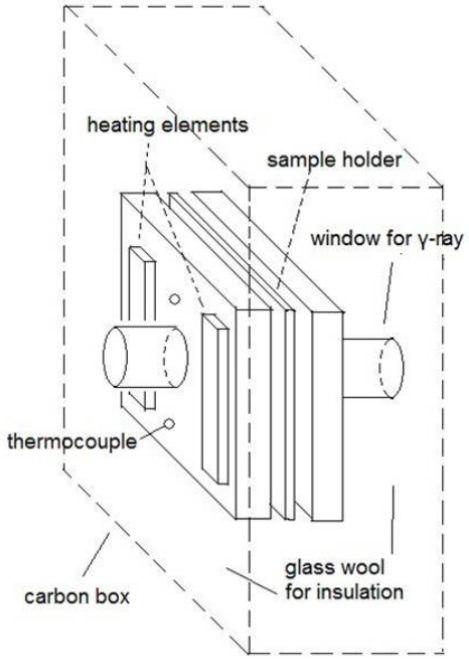

Figure 4.3. Schematic of furnace used for elevated temperature Mössbauer measurements.

4.3.4 Resistive furnace for high temperature Mössbauer measurements

To collect Mössbauer data at elevated temperature, the sample is mounted in a resistive furnace, depicted in Fig. 4.3. The sample is contained in high temperature kapton and sandwiched between two aluminum plates, with a window for γ-ray transmission. The temperature is controlled with two resistors mounted on the aluminum sample holder. Three thermocouples to are affixed to different positions around the sample to monitor the temperature. The entire assembly is aligned between the source and the detector to optimize γ-ray transmission.

4.4 Nuclear forward scattering

The high intensity and pulsed structure of a synchrotron radiation source allows for the collection of nuclear resonant time spectra. This time domain analogue to traditional Mössbauer Spectrometry is known as nuclear forward scattering (NFS) or Synchrotron Mössbauer Spectrometry (SMS). The small line width of the nuclear resonance of ^{57}Fe, 4.66 neV, necessitates an x-ray source with high spectral intensity to excite the nuclear transition. The low angular divergence and

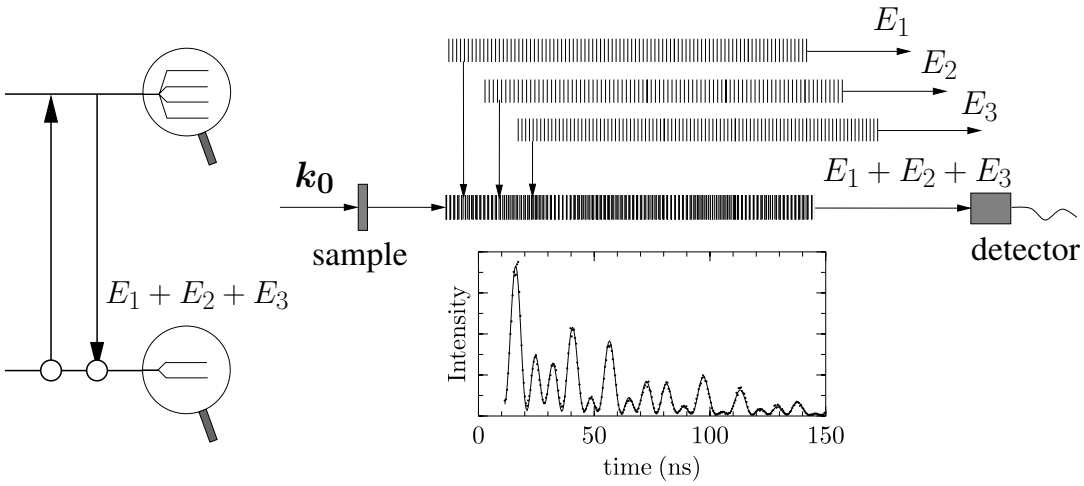

Figure 4.4. A coherent superposition of wavlets from slightly offset energy levels gives rise to quantum beats in the temporal evolution of the nuclear decay. Figure from Röhlsberger (2004) [2].

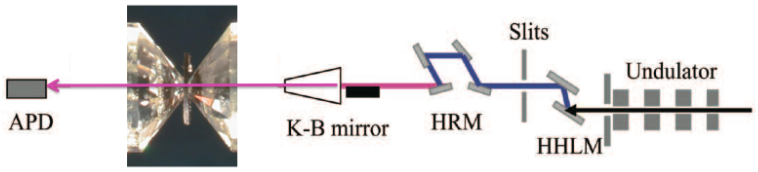

Figure 4.5. Schematic of beamline set up for nuclear resonant scattering. Picture adapted from Zhou, et al. (2004) [3].

high brilliance of the synchrotron beam allows for high-pressure experiments to be run in a diamond anvil-cell.

A pre-monochromater filters and tunes the incident beam to the resonant energy, and a high-resolution monochrometer further reduces the energy bandwidth to $\sim$2meV. The ensemble of ^{57}Fe nuclei are simultaneously excited by a synchrotron radiation pulse. The standard time structure of the synchrotron radiation at the advanced photon source (APS) provides 24 pulses separated by 153.3 ns, each having a duration of $\sim$70ps. The electronic scattering occurs within femtoseconds of the pulse arrival, while the lifetime of the nuclear resonant state is 141 ns. This allows for a clear separation of the prompt electronic scattering from the delayed, resonant scattering of interest. The synchrotron pulse creates a collective nuclear excitation with coherent interference between emitted photons in the forward direction. If the degeneracy of the nuclear levels has been lifted by hyperfine interactions, the phased de-excitation of slightly offset energy levels produces beat patterns in trans-

mitted intensity. The delayed emisson is expressed as a sum over oscillatory terms whose arguments are the differences in the energies of the nuclear levels superimposed on the exponential decay [45].

$$T(t) \sim \frac{\eta^2}{16\Omega\tau^2} \exp(-t/\tau) \sum_{j,l} \exp(-\mathrm{i}\omega_{j,l}t)\ \mathbf{a_0^*}\, W_j W_l\, \mathbf{a_0}\ .$$

Here $\hbar\Omega$ is the energy bandwidth of the synchrotron pulse, W is the normalized weight of the nuclear transition, $\omega_{j,l} = \omega_j - \omega_l$, $\mathbf{a_0}$ is the polarization unit vector of the synchrotron radiation, and $\eta = f\sigma\rho D$ is the effective thickness. The effective thickness quantifies the scattering power and the influence of sample thickness on spectra. In this expression f is the recoil free fraction, σ is the nuclear resonant cross section, ρ is the density of ^{57}Fe nuclei, and D is the sample thickness. A sample with two Fe sites, each with distinct quadrupole splittings and isomer shifts, will have six component beat frequencies in the transmitted intensity, each with a period that is inversely related to the difference in nuclear energy levels, $\hbar/\Delta E_{HF}$.

To collect an NFS spectra, timing electronics are used to block the signal for the first several ns after the pulse arrival. After this deadtime, an avalanche photodiode detector (APD) positioned in the forward-scattered x-ray beam measures the delayed counts as a function of time after pulse arrival.

4.5 High pressure measurements

Elevated pressure measurements where carried out using diamond-anvil cells (DACs) to generate quasi-hydrostatic pressure. Pressure is simply the applied force divided by the area over which this force is distributed: P=F/A. To generate a high pressure with a moderate force, the area must be small. The flattened faces of gem quality diamonds are ideal surfaces to generate high pressures because diamonds have unparalleled hardness and are optically transparent at typical x-ray frequencies. In a conventional diamond-anvil cell, depicted in Fig. 4.6, the sample is compressed between the culets of two gem quality diamonds. Typical culet diameters range from 100-500μm. For the experiments in this thesis all culets were $\sim 300\mu$m. The sample is contained in a chamber made from a metal gasket sandwiched between the opposing diamonds. The diamonds are mounted on tungsten carbide seats with epoxy resin and these seats are screwed into the cell, taking care to ensure the diamonds are both centered and the culet faces are parallel. To prepare the sample cham-

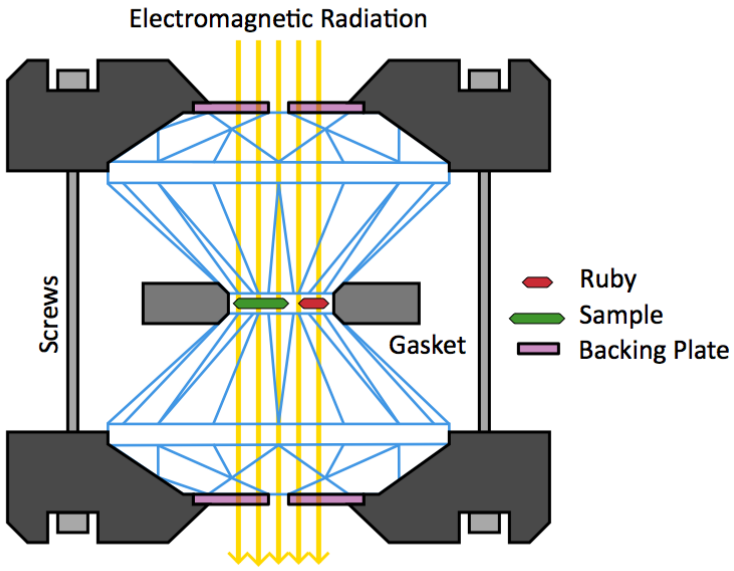

Figure 4.6. Schematic of diamond-anvil cell. Figure: Tobias 1984- CC BY-SA 3.0.

ber, a rhenium gasket is pre-compressed between the diamonds to generate a culet-size indentation in the center of the gasket. A sample chamber is drilled in the center of the indentation using an electric discharge milling machine. For 300μm culets the appropriate drill bit is chosen to make a hole with an $\sim 100\mu$m diameter. After drilling, the gasket is cleaned and placed back into the DAC. Using the tip of a needle, the sample is loaded into the chamber, along with a few small pieces of ruby that will be used for pressure measurement. Finally the cell is closed by tightening the screws, pushing the two sides of the cell together confining the sample between the opposing culets and the gasket. The cell has several screws around its circumference that push the opposing sides of the DAC together. Care is taken to maintain parallel alignment, by tightening the cell in small steps and turning pairs of screws on either side of the cell simultaneously. This is done using a DAC designed with a combination of right and left-handed screws. Commonly the screws are fitted with spring-loaded washers to allow for carefully-controlled tightening.

For the measurements in this thesis, two different types of DAC designs were used, a Mao-type symmetric DAC and a smaller Tel-Aviv DAC, shown in Figs. 4.8 and 4.7 respectively. The smaller of the two designs is a Merill-Bassett, Tel Aviv-type cell [46]. This design has two opposing plates that are held together with a series of pins. The symmetric cell has a piston-cylinder design, that has

Figure 4.7. Photo of Tel Aviv-DACs, shown with stack of quarters for size comparison.

Figure 4.8. Photo of Mao-type symmetric cell.

the benefit of making it easier to ensure the diamonds remain parallel during operation. To generate hydrostatic pressure, this sample chamber is filled with a pressure medium if possible. The pressure medium transmits the uniaxial pressure generated by the opposing diamond culets to the sample by creating an isotropic fluid-filled pressure chamber that is confined laterally by the gasket material. Pressurized helium or neon gas are optimal pressure media. To fill the sample chamber with gas, the cell is placed in a specialized chamber that is first evacuated then filled with pressurized gas. The cell is then closed using gears within the chamber that are controlled remotely. A system designed to gas-load symmetric DACs is maintained by the staff at sector 13 at the Advanced Photon Source.

An alternative to using the screws to increase pressure is to use a gas-membrane system. This

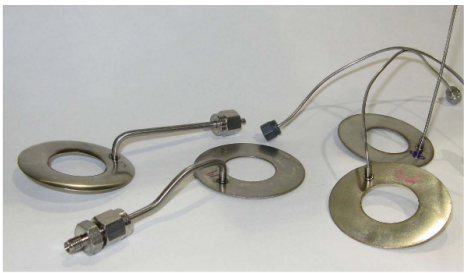

Figure 4.9. Pressure membranes for remote pressure control.

configuration allows for the pressure to be adjusted remotely, which is particularly useful when conducting experiments in a sample environment (i.e. a cyostat or furnace). Shown in Fig. 4.9, a doughnut shaped gasket that can be inflated with gas is pushed against the back of the cell and clamped in place flush with the cell. The force that this bladder exerts on the back of the cell substitutes for the force that would otherwise be applied by tightening the screws. The expansion/contraction of the bladder is controlled remotely by controlling the gas pressure.

To determine the pressure in the sample chamber, a laser is used to monitor the frequency shift of the R ruby-fluorescence lines. The behavior of this band at elevated pressure and temperature is well known. The R_1/R_2 doublet shows an approximately linear shift upward with increasing pressure, providing a good reference for pressure calibration. Using a laser/spectrometer system that can be moved into the beam path when the x-ray shutter is closed, the pressure of the sample can be monitored in situ. When using the gas-membrane system to control the sample pressure, this information can be used as feedback to maintain the desired pressure. This feedback is particularly important when heating or cooling the DAC assembly, as changing the temperature will often result in changes in pressure in the cell.

4.6 Experimental setup for high temperature, high pressure measurements

To collect synchrotron data at elevated pressure and temperature, the diamond-anvil cell is mounted in a resistive furnace. The first iteration of experiments in this thesis where carried out using inconel Tel-Aviv DACs and a resistive furnace, shown in Fig. 4.10. A continuous flow of Ar/1%H_2 gas was maintained with the aim of protecting the diamonds from damage at elevated temperature. In later experiments, a symmetric cell was used. In these experiments, a copper-block furnace was used to heat the cell, shown in Fig. 4.11 This furnace was used in conjunction with a gas membrane pressure system, allowing for remote monitoring and adjustment of pressure in the cell. The entire furnace assembly was contained in a vacuum chamber. To monitor the temperature, three thermocouples were used, one was glued to the side of the diamond, a second was affixed to the outside of the cell, and a third was attached to the Cu block. For NFS experiments at beamline 16ID-D at the Advanced Photon Source, the vacuum furnace was used in conjunction with a

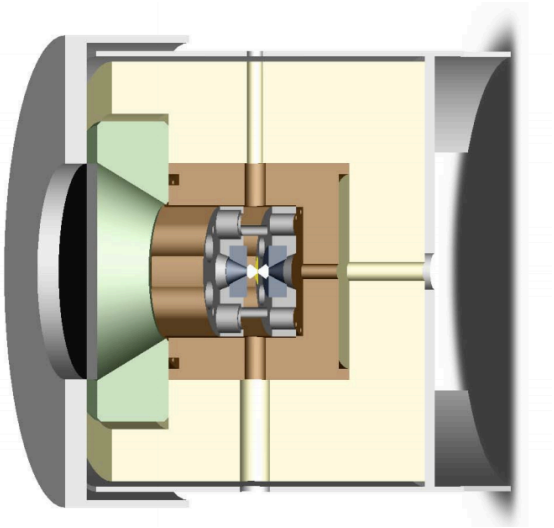

Figure 4.10. Schematic of furnace used for high temperature, high pressure synchrotron experiments with Tel Aviv-DACs.

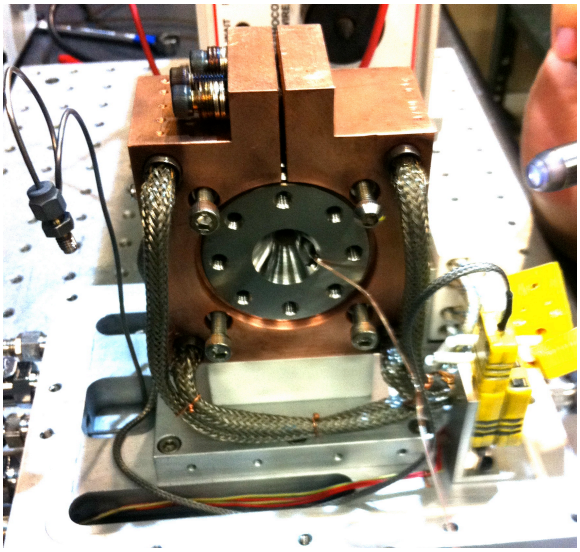

Figure 4.11. Photo of furnace used for high temperature, high pressure synchrotron experiments with symmetric DACs.

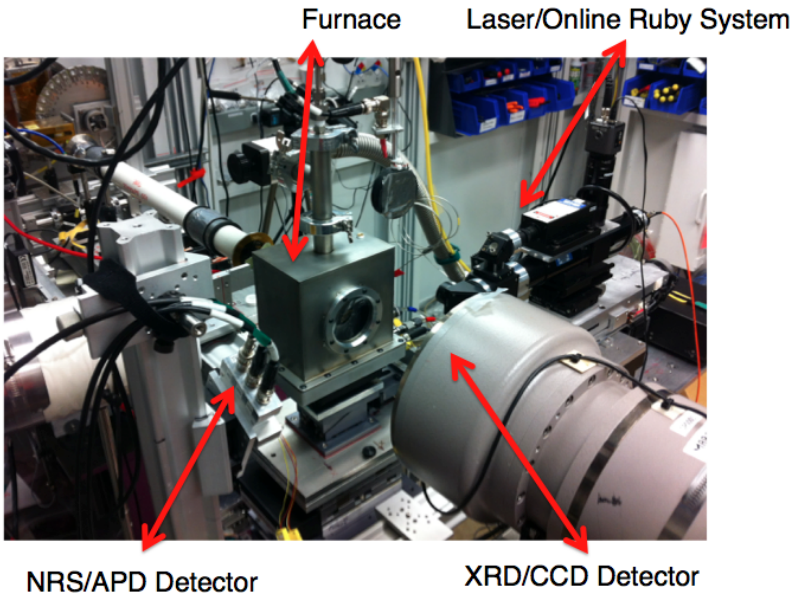

Figure 4.12. Photo of setup at beamline 16-IDD, including vacuum furnace, online ruby system, CCD for XRD, and APD for NFS.

pressure-membrane/online-ruby system. In addition, a CCD detector was used to collect in-situ XRD using the 14.4 keV wavelength. The full experimental set-up is shown in Fig. 4.12.

4.7 Relaxation effects

4.7.1 Overview

Nuclear resonant scattering provides a particularly effective method to study the dynamics of charge hopping processes. It is possible to observe the dynamical effects when the fluctuations in the hyperfine field occur on the same time scale as the nuclear decay process. The quadruple interaction provides a natural time window for sampling the electric field surrounding the Mössbauer nuclei: $\tau_{EFG} = \hbar/\Delta E_{HF}$. If the time scale of the charge hopping processes is much slower than this window, the observed spectrum is a coherent superposition of two static components associated with distinct 2+ and 3+ Fe valences. If the polaron hopping frequency exceeds this sampling frequency, observable distortions appear in the spectra. With further increase in hopping frequency, the spectrum begins to resemble that of a single, time-averaged doublet. Altering the valence fluctuation frequency can give rise to rich variations of the shape and symmetry of the quadrupole doublets. The interesting behavior occurs when the valence of a ^{57}Fe ion fluctuates between Fe^{2+} and Fe^{3+}

at a frequency between 1 and 100 MHz. In conventional Mössbauer energy spectra the quadrupole doublets from Fe^{2+} and Fe^{3+} merge together, with asymmetric, non-Lorentzian lineshapes for these intermediate frequencies. For nuclear forward scattering in the time domain, these effects are seen as a distortion and washing-out of the quantum beat pattern from interference of the nuclear hyperfine levels. When the relaxation is most pronounced, there is a large suppression in the integrated count rate. The fast fluctuations tend to dephase the photons emitted from separate nuclei, resulting in a loss of coherence that is seen as an overall reduction in the probability for the excitation of a nuclear exciton. Although the dynamical information that can be extracted from an NFS spectra is essentially the same as from a conventional Mössbauer spectrum, this strong suppression of intensity is unique to NFS.

4.7.2 Blume-Tjon model

Drawing on ideas about motional narrowing developed by Kubo and Anderson [47], Blume and Tjon developed a stochastic theory to describe the effect of randomly fluctuating hyperfine fields on a Mössbauer spectrum [48, 49]. Within this model, a fluctuating nuclear environment is treated by providing multiple sets of hyperfine parameters, together with a matrix of transition rates describing the random jumps between the different sets of hyperfine parameters. This allows for the refinement of the hyperfine parameters specific to each site, as well as a transition frequency. For polycrystalline samples, the problem reduces to the simplest case treated by Blume and Tjon in which the stochastic and quantum mechanical parts of the problem are separable as there is no issue of non-commutativity of the Hamiltonian at different times.

The nuclear Hamiltonian is written in terms of a stochastic function $f(t) = \pm 1$, describing either the 3+ or the 2+ site at any instant,

$$\hat{H} = \hat{H}_o + \frac{1}{12}\left[(1+f(t))\Delta Q S^{2+} + (1-f(t))\Delta Q S^{3+}\right](3m_I^2 - I(I+1)), \tag{4.13}$$

where $\hat{H}_0$ is the nuclear Hamiltonian in the absence of hyperfine splittings,

$$\begin{aligned} \hat{H}_0|I_0 m_0\rangle &= E_0|I_0 m_0\rangle, \\ \hat{H}_0|I_1 m_1\rangle &= E_1|I_1 m_1\rangle, \\ E_1 - E_0 &= 14.41\,\text{keV}. \end{aligned} \tag{4.14}$$

Isolating the time dependent terms, Eq. 4.13 can be rewritten as,

$$\begin{aligned} \hat{H} &= \hat{H}_o + [q_1 + q_2 f(t)]\,(3m_I^2 - I(I+1)), \\ q_1 &= \frac{1}{12}(\Delta Q S^{2+} + \Delta Q S^{3+}), \\ q_2 &= \frac{1}{12}(\Delta Q S^{2+} - \Delta Q S^{3+}). \end{aligned} \tag{4.15}$$

The probability for a transition between the excited and ground state with the emission of a photon is Lorentzian in form,

$$P_{1,0}(\omega) = \frac{|\,\langle I_0 m_0|\hat{H}^{(+)}|I_1 m_1\rangle\,|^2}{(\omega + E_0 - E_1)^2 + \frac{1}{4}\Gamma^2}, \tag{4.16}$$

where $\mathrm{H}^{(+)}$ is interaction Hamiltonian of solid and photon and Γ is the linewidth of the excited state. Expressing the denominator in integral form, the relationship

$$\left((\omega + E_0 - E_1)^2 + \frac{1}{4}\Gamma^2\right)^{-1} = \frac{2}{\Gamma}\mathrm{Re}\int_0^\infty \exp\left[i(\omega + E_0 - E_1)t - \Gamma t/2\right] dt, \tag{4.17}$$

allows for a recasting of Eq. 4.16 to incorporate an explicit time dependence,

$$\begin{aligned} P_{1,0}(\omega) &= \frac{2}{\Gamma}\mathrm{Re}\int_0^\infty \exp(i\omega t - \frac{1}{2}\Gamma t)\langle I_0 m_0|\hat{H}^{(+)}|I_1 m_1\rangle^* \langle I_0 m_0|\exp^{i-E_0 t}\hat{H}^{(+)}\exp^{i-E_1 t}|I_1 m_1\rangle dt \\ &= \frac{2}{\Gamma}\mathrm{Re}\int_0^\infty \exp(i\omega t - \frac{1}{2}\Gamma t)\langle I_1 m_1|\hat{H}^{(-)}|I_0 m_0\rangle\langle I_0 m_0|\hat{U}^\dagger(t)\hat{H}^{(+)}\hat{U}(t)|I_1 m_1\rangle dt. \end{aligned} \tag{4.18}$$

Here $\hat{H}^{(-)} = \hat{H}^{(+)\dagger}$ and $\hat{U}(t)$ is the time evolution operator,

$$\begin{aligned} \hat{U}(t) &= \exp(-i\hat{H}t), \\ \hat{H}^{(+)}(t) &= \hat{U}^\dagger(t)\hat{H}^{(+)}\hat{U}(t). \end{aligned} \tag{4.19}$$

The observed probability results from averaging Eq. 4.18 over all possible excited states $|I_1 m_1\rangle$ and summing over the ground states $|I_0 m_0\rangle$,

$$P(\omega) = \sum_{0,1} p_1 W_{0,1} = \frac{2}{\Gamma} \mathrm{Re} \int_0^\infty \exp(i\omega t - \frac{1}{2}\Gamma t))[\langle \hat{H}^{(-)} \hat{H}^{(+)}(t)\rangle]_{av} dt. \tag{4.20}$$

Here $[]_{av}$ indicates an average over the Hamiltonian's stochastic degrees of freedom. The correlation function in Eq. 4.20 is defined as,

$$\begin{aligned}[\langle \hat{H}^{(-)} \hat{H}^{(+)}(t)\rangle]_{av} = \sum_{m_1 m_0 m_1^{'} m_0^{'}} \frac{1}{2I_1+1} [\langle I_1 m_1 | \hat{H}^{(-)} | I_0 m_0\rangle \langle I_0 m_0 | \exp(i \int_0^t \hat{H}(t')dt') | I_0 m_0'\rangle \\ \times \langle I_0 m_0' | \hat{H}^{(+)} | I_1 m_1'\rangle \langle I_1 m_1' | \exp(-i \int_0^t \hat{H}(t')dt') | I_1 m_1\rangle]_{av}.\end{aligned} \tag{4.21}$$

Here it is assumed that the excited m_1 sublevels are equally probable, i.e. $p_1 = 1/(2I_1+1)$, and the operator in Eq. 4.19 has been replaced with a time-ordered operator,

$$\hat{U}(t) = \exp\left[-i \int_0^t \hat{H}(t')dt'\right]. \tag{4.22}$$

The sum in Eq. 4.21 involves two time-ordered series. For the Hamiltonian defined in Eq. 4.13, the first of these series is straightforward to evaluate, as the ground state in the ^{57}Fe I= $3/2 \rightarrow 1/2$ transition is unspilt,

$$\langle I_0 m_0 | \exp(i \int_0^t \hat{H}(t')dt') | I_0 m_0'\rangle = \exp(iE_0 t)\delta_{m_0 m_0'}. \tag{4.23}$$

The second sum in Eq. 4.21 becomes,

$$\begin{aligned}[\langle I_1 m_1' | \exp(-i \int_0^t \hat{H}(t')dt') | I_1 m_1\rangle]_{av} = \exp(-iE_1 t)\exp(-i\beta t)\left[\exp\left(-i\alpha \int_0^t f(t')dt'\right)\delta_{m_1 m_{1'}}\right]_{av}, \\ \alpha = q_2(3m_I^2 - 15/4), \\ \beta = q_1(3m_I^2 - 15/4).\end{aligned} \tag{4.24}$$

The stochastic average in Eq. 4.24 is evaluated with the use of a transition probability matrix,

W, that describes the transition rates between the different sets of hyperfine parameters,

$$\left[\exp\left(-i\alpha\int_0^t f(t')dt'\right)\delta_{m_1 m_{1'}}\right]_{av} = \sum_{\rho\sigma} p_\rho(\sigma|\exp(-i\alpha\mathbf{F}+\mathbf{W})t|\rho). \tag{4.25}$$

Here **F** is a matrix with the possible values of the stochastic function $f(t)$ on the diagonal,

$$\mathbf{F} = \begin{bmatrix} 1 & 0 \\ 0 & -1 \end{bmatrix}. \tag{4.26}$$

The elements transition probability matrix, $W_{\rho\sigma}$, represent the probability per unit time that the system experiences a transition from state ρ to state σ,

$$\mathbf{W} = \begin{bmatrix} -w_{3+\to 2+} & w_{3+\to 2+} \\ w_{2+\to 3+} & -w_{2+\to 3+} \end{bmatrix}. \tag{4.27}$$

The diagonal elements of the transition probability matrix are determined by the off diagonal elements such that,

$$W_{\rho\rho} = -\sum_{\rho} W_{\rho\sigma}. \tag{4.28}$$

For charge hopping between Fe^{2+} and Fe^{3+} sites, in order to maintain charge balance, **W** is expressed using a single frequency weighted by population of the two states,

$$\mathbf{W} = \begin{bmatrix} -\rho_{2+}w & \rho_{2+}w \\ \rho_{3+}w & -\rho_{3+}w \end{bmatrix}. \tag{4.29}$$

Substituting Eqs. 4.23 and 4.24 into Eq. 4.20 and integrating gives the observed profile as an analytic expression in terms of the transition probability matrix,

$$\begin{aligned} P(\omega) = \frac{1}{2\Gamma}\sum_{m_0 m_1} |\langle I_0 m_0|\hat{H}^{(+)}|I_1 m_1\rangle|^2 \mathrm{Re}\sum_{\rho\sigma} p_\rho(\sigma|[p\mathbf{I}+i\alpha\mathbf{F}-\mathbf{W}]^{-1}|\rho), \\ p = -i\,(\omega-\omega_0-\beta)+\Gamma/2, \\ \omega_0 = E_1 - E_0 = 14.4\,\mathrm{keV}. \end{aligned} \tag{4.30}$$

The matrix elements $|\langle I_0 m_0|\hat{H}^{(+)}|I_1 m_1\rangle|$ determine the polarization and intensity of the individual lines and for polycrystalline samples the first part of Eq. 4.30 can be treated as a constant. For charge hopping in the phospho-olivines, ferric iron is introduced by removing alkali ions, $M_x Fe_x^{2+} Fe_{1-x}^{3+} PO_4$, such that $\rho_{2+} = x$ and $\rho_{2+} + \rho_{3+} = 1.0$. The calculation of the second part of Eq. 4.30 is now straightforward,

$$P(\omega) \propto \text{Re}\left(\frac{p + 2w + i\alpha(2x-1)}{p^2 + \alpha^2 + pw + i\alpha w(2x-1)}\right). \tag{4.31}$$

4.8 Nuclear resonant scattering data analysis

Analysis of nuclear resonant scattering data was carried out using the CONUSS package (COherent NUclear resonant Scattering by Single crystals) [50]. CONUSS allows for the calculation and refinement of nuclear resonant scattering spectra both in the time and energy domains. The program enables the user to define a fit model, specifying the hyperfine parameters associated with a number of iron sites and the phase fractions of these sites. CONUSS requires a starting model that is reasonably accurate and is best suited for optimizing parameters within a known model. While the software was originally developed for analysis of time spectra from synchrotron nuclear resonant scattering, the program can handle conventional Mössbauer data as well. The program incorporates a full treatment of thickness-dependent dynamical effects that can give rise to "speed-up," as well as complicated spectral distortions.

CONUSS offers a choice between static hyperfine interactions and randomly fluctuating hyperfine fields, as described by a Blume-Tjon model [48, 49]. It is also possible to set up a fit model where certain sites experience fluctuating hyperfine fields while others are static. A static site is characterized by its weight fraction, an isomer shift, a quadrupole splitting and a linewidth for a lorentzian quadrupole splitting distribution. When appropriate, it is also possible to include an asymmetry parameter as well as parameters associated with magnetism and textural effects. To calculate thickness effects, the program input also calls for the definition of the sample thickness and a Debye temperature to calculate the recoil free fraction. Given these parameters, the hyperfine splittings and corresponding eigenvectors are determined by numerically diagonalizing the nuclear

Hamiltonian,

$$\sum_{m_0 m_1} \Phi_{j_0 m_0} H_{m_0 m_1} \Phi_{m_1 j_1} = E_j \delta_{j_0 j_1}. \tag{4.32}$$

Fluctuating hyperfine fields are treated by providing the same set of hyperfine parameters together with the matrix of transition rates, W, describing the jumps between different sets of hyperfine parameters. In this case, the eigenvalue problem becomes,

$$\sum_{m_0 m_1 m_0' m_1' \rho\sigma} L^{\mu\rho}_{j_0 j_1 m_0 m_1} A^{\rho\sigma}_{m_0 m_1 m_0' m_1'} R^{\sigma\nu}_{m_0' m_1' l_0 l_1} = \Omega^{\mu}_{j j_1} \delta_{\mu\nu} \delta_{j_0 l_0} \delta_{j_1 l_1}. \tag{4.33}$$

Here L and R are the left and right eigenvectors and the eigenvalues (Ω) are now complex. The matrix A incorporates the transition probability matrix, W, along with the matrix elements of the Hamiltonian for the excited and ground states,

$$A^{\rho\sigma}_{m_0 m_1 m_0' m_1'} = iW^{\rho\sigma} \delta_{m_0 m_0'} \delta_{m_1 m_1'} + \langle I_1 m_1 | \hat{H}^{\rho} | I_1 m_1' \rangle \delta_{m_0 m_0'} \delta_{\rho\sigma} - \langle I_0 m_0 | \hat{H}^{\rho} | I_0 m_0' \rangle \delta_{m_1 m_1'} \delta_{\rho\sigma}, \tag{4.34}$$

where ρ indicates a particular set of hyperfine parameters.

CONUSS uses the solutions to the eigenvalue problems of Eqs. 4.32 or 4.33 to calculate the coherent nuclear scattering amplitudes. For nuclear forward scattering, the Fourier transformation of the energy-dependent transmission function allows for the calculation of the time-dependent intensity. This theoretical model is then compared to the data, and parameters are adjusted iteratively to minimize the mean square deviation between the fit model and the experimental spectra. This allows for the refinement of the hyperfine parameters specific to each site as well as the elements of the transition probability matrix, W, which defines the jump rates between the different sets of hyperfine parameters. For a typical two-site dynamical model, the ratio of these matrix elements is proportional to the weight ratio of the two sites. Consequently, to maintain charge balance a constant ratio must be maintained. CONUSS allows for the grouping of fit parameters such that the matrix elements can be refined while keeping their ratio fixed.

Chapter 5

Polaron-ion correlations in $Li_{0.6}FePO_4$

5.1 Introduction

Lithium-iron phosphate, $LiFePO_4$, is a new material for cathode electrodes of rechargeable Li-ion batteries [51]. An important issue, however, is its low electrical conductivity; at low temperatures $LiFePO_4$ is an insulator with a band gap of approximately 3.7 eV [52–54]. $LiFePO_4$ has the orthorhombic olivine-type structure shown in Fig. 5.1. Layers of corner-sharing networks of canted FeO_6 octahedra in the b-c plane are spaced by phosphate tetrahedra. Li^+ cations form one-dimensional chains that run between the FeO_6 planes. Previous work showed that the Li^+ diffusion pathway is along these b-axis channels [12, 55]. The electronic carrier mobility is expected to be two-dimensional, occurring within the layers of FeO_6 octahedra that are separated by insulating phosphate groups.

Experimental values of both electrical conductivity and Li^+-ion diffusivity in $LiFePO_4$ span several orders of magnitude [56–62]. These large discrepancies have been attributed to differences in samples and experimental technique [63]. It is generally accepted that the Li^+ ion diffusivity is highly sensitive to defects in the one-dimensional channels along the b axis. Less understood is the scatter in reported values of electrical conductivity, however, which contributed to an early controversy about whether the electronic conductivity can be improved by doping [64]. Measurements of bulk properties on polycrystalline samples also present challenges in decoupling the intrinsic conductivity from the interparticle conductivity. Nevertheless, a keen interest remains in improving the intrinsic electrical conductivity of $LiFePO_4$, and better understanding the transport of Li^+ ions and

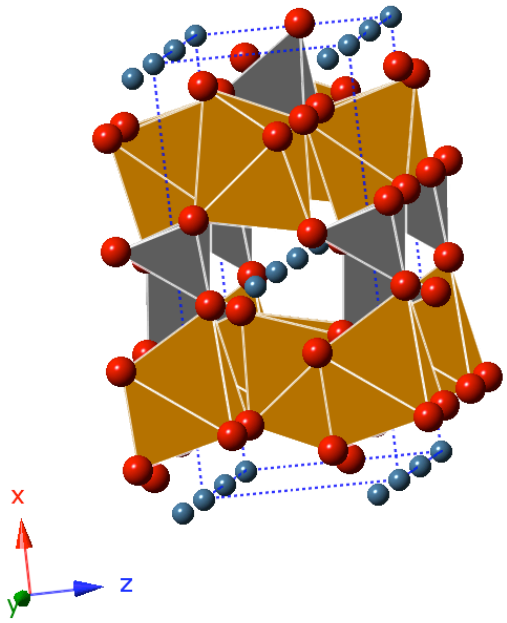

Figure 5.1. Olivine-type structure of $LiFePO_4$ with chains of Li^+ ions (blue), planes of FeO_6 octahedra (brown), and phosphate tetrahedra (grey).

electrons.

As with many other transition metal oxides, the mechanism of electrical conductivity in mixed valent $Li_xFe^{2+}_xFe^{3+}_{1-x}PO_4$ is small polaron hopping [65–67]. A small polaron quasiparticle comprises an electron or hole localized by atomic displacements of neighboring anions. When an electron transfers between Fe^{2+} and Fe^{3+} sites, the local configurations of the FeO_6 octahedra must also transfer. The difference between these atomic configurations in $LiFePO_4$ is large. By removing Li^+ ions from the lattice, lithiated $Li_1Fe^{2+}PO_4$ is transformed into delithiated $Fe^{3+}PO_4$ with the same olivine-type structure. As the Fe ions change from Fe^{2+} to Fe^{3+} during delithiation, the average Fe-O bond lengths are reduced by 6% [68].

At moderate temperatures, the motion of a polaron quasiparticle is diffusive and can be understood as an activated process with a jump rate [37, 69],

$$\Gamma(T,P) \simeq \nu \, \exp(-2\alpha R) \, \exp\left(-\frac{E_a + PV_a}{k_B T}\right) , \tag{5.1}$$

where T is temperature, P is pressure, k_B is the Boltzmann constant, ν is a characteristic phonon

frequency, R is the Fe-Fe distance, and α is the inverse localization length of the Fe wave functions. The activation energy, E_a, describes the energetic barrier for the polaron quasiparticle to transfer between adjacent iron sites. Previous measurements of bulk electronic conductivity as a function of temperature gave a wide range of activation energies between 155 and 630 meV [64, 70–73]. Mössbauer spectrometry provides a more direct measurement of the rate of polaron hops between iron sites, and gives an activation energy around 500 meV [65, 66].

The effect of pressure on the activation barrier is quantified with an activation volume, V_a. PV_a is the extra enthalpy required from thermal fluctuations to induce a polaron hop when the material is under the pressure P. For $V_a > 0$, the activation barrier is effectively raised with pressure, and the polaron hopping frequency is suppressed. V_a is the difference in volume between the material with the configuration favorable for electron transfer, and the volume in the equilibrium configuration. It is expected to be local in origin, and is expected to reflect the local expansion or contraction in the vicinity of the hopping polaron. In accordance with the Frank-Condon principle, these local atomic distortions bring the electron levels of the initial and final states into coincidence, facilitating electron transfer. An understanding of the activation volume therefore gives insight into the atom configurations at the transient state of the polaron hop.

There have been few studies of the activation volume for polaron hopping. Previous measurements of electrical conductivity in geophysically relevant oxides under applied pressure gave small, negative values for V_a of a few tenths of a cubic angstrom [30–33]. It has been suggested that the dominant effect in these systems was the decrease of R under pressure, allowing the electron to better sample the final state, therefore enhancing the polaron conductivity [33]. To our knowledge there has been no measurement of the electronic conductivity of $LiFePO_4$ under pressure.

Unlike the motion of polarons, the diffusion of Li^+ ions can be understood classically. Ion jumps into vacant neighboring sites occur by an activated process that does not sense the ion destination until after the jump is complete. First principles simulations suggest that Li^+ ions diffuse rapidly along the [010] channels, but there is a high energy barrier to cross between channels [12]. These calculations do not include defects or electron-ion interactions, however, and other reports suggest the material is a slow ion conductor [56]. The one-dimensional character of the Li^+ mobility results in an ion conductivity that is highly sensitive to defects that block conduction channels, such as Li-Fe antisite point defects [11, 12].

Here we report new results on the charge dynamics at elevated pressure, obtained by performing measurements on Li_xFePO_4 heated in a diamond-anvil cell. The ^{57}Fe valence fluctuations in Li_xFePO_4 are strongly sensitive to pressure, giving a large and positive activation volume for polaron hopping that is more characteristic of ion diffusion. We show how this large effect could result from a correlated dynamics of polarons and mobile Li^+ ions. Previous density functional theory calculations for $LiFePO_4$ gave low activation barriers for polaron hopping compared to experimental results. This discrepancy was attributed to polaron-ion interactions [74]. The concept of a bound polaron has also been discussed in calculations of polaron migration barriers for lithium peroxide [75]. These studies assume a rigid lattice during electron transport, however. The authors state, "...the electron density alone is relaxed self-consistently and atom positions remain fixed for calculations along the migration path." [74] In other words, this method employs a linear combination of the initial and final states without allowing for ion rearrangements in the transition state, so $V_a = 0$. Ion-electron correlations have also been mentioned in reports of NMR and molecular dynamics studies on $LiMn_2O_4$ and Li_xNiO_2 [76, 77], for example, but there has been scant experimental evidence to support this concept. With a polaron-ion interaction, the activation enthalpy for moving a polaron depends in part on the ion motion by a vacancy mechanism. Vacancy diffusion is suppressed by pressure, and activation volumes for ion transport in oxides range from +1 to +10 Å^3 [38]. Because ion transport is suppressed by pressure, polaronic conductivity should also be suppressed if the polaron-ion interaction energy, $E_{\rm pi}$, is large. In what follows, we estimate $E_{\rm pi}$ to be approximately –300 meV, which should have important consequences for the dynamics and positions of both polarons and ions.

5.2 Experimental

A solid solution of Li^+ ions in Li_xFePO_4 is stable at temperatures above 473 K, and is easily preserved at room temperature by quenching [23, 24]. Previous x-ray diffractometry measurements showed that the olivine structures of $FePO_4$, $Li_{0.6}FePO_4$, and Li_1FePO_4 are stable to pressures of at least 30 GPa at 300 K [78]. Solid solutions of $Li_{0.6}FePO_4$ were prepared by a solid-state reaction and delithiated as described previously [23, 79]. Powders were loaded into a Merrill-Bassett, Tel Aviv-type, diamond-anvil cell [46] along with ruby chips for pressure measurement by the ruby

florescence method [80]. The cells were prepared using rhenium gaskets and diamonds with 350 μm culets. The cell was heated in a resistive furnace with an Ar/1% H_2 atmosphere and kapton windows for x-ray transmission.

Nuclear forward scattering (NFS) measurements were performed at beamline 16ID-D at the Advanced Photon Source at Argonne National Laboratory. An avalanche photodiode detector was placed in the forward-scattered x-ray beam to measure transmitted intensity as a function of time. Four sets of measurements were taken at pressures of 0, 3.5, 7.1, and 17 GPa, with temperatures between 298 and 598 K. A high-resolution monochrometer tunes the incident beam to the 14.414-keV resonant energy and reduces the bandwidth to $\sim$2 meV. The synchrotron flashes had durations of 70 ps, and were separated by 153 ns. Electronic scattering occurs within femtoseconds of the pulse arrival at the sample. The relatively long lifetime of the nuclear resonant state ($\tau = 141$ ns) allows for a clear separation of the prompt electronic scattering from the delayed, resonant scattering.

The ^{57}Fe nuclei in the sample are simultaneously excited by the synchrotron x-ray pulse, giving rise to coherent interference between emitted photons in the forward direction. When the degeneracy of the nuclear levels is lifted by hyperfine interactions, the phased de-excitation of slightly offset energy levels generates beat patterns in the transmitted intensity. Within the kinematical limit, the delayed emission in the forward direction is expressed as a sum over oscillatory terms whose arguments are the differences in the energies of the nuclear levels, superimposed on the exponential decay [45],

$$A(t) \sim \exp(-t/\tau) \sum_{j,l} \exp(-\mathrm{i}\omega_{j,l} t)\ \mathbf{a_0^*}\, W_j W_l\, \mathbf{a_0}\ . \tag{5.2}$$

Here W is the normalized weight of the nuclear transition, $\omega_{j,l} = \omega_j - \omega_l$, and $\mathbf{a_0}$ is the polarization unit vector of the synchrotron radiation. A sample with two iron sites, each with a distinct value for quadrupole splitting (QS) and isomer shift (IS), will have six component beat frequencies in the transmitted intensity, each with a period that is inversely related to the difference in nuclear energy levels.

Nuclear resonant scattering allows for the study of local electron dynamics at iron ions. The measured spectra are altered when the hyperfine fields fluctuate on the same time scale as the characteristic frequency of the hyperfine interaction energies, $\hbar\omega$. In Li_xFePO_4 the frequency of valence fluctuations, and how this frequency changes with temperature, leads to rich variations of the shape

and symmetry of the quadrupole doublets from Fe^{2+} and Fe^{3+}. At low frequencies and low temperatures, the spectral components from Fe^{2+} and Fe^{3+} remain distinct, and at very high frequencies the spectrum is a single doublet. The rich behavior occurs when the valence of a ^{57}Fe ion fluctuates between Fe^{2+} and Fe^{3+} at a frequency between 1 and 100 MHz. In conventional Mössbauer energy spectra the quadrupole doublets from Fe^{2+} and Fe^{3+} merge together, with asymmetric, non-Lorentzian lineshapes for these intermediate frequencies. For nuclear forward scattering (NFS) in the time domain, these effects are seen as a distortion and washing-out of the quantum beat pattern from interference of the nuclear hyperfine levels. Previous conventional Mössbauer energy spectrometry studies on Li_xFePO_4 reported dramatic spectral distortions at temperatures between 373 and 513 K [65, 66].

5.3 Simulational

The hops of electron polarons are likely confined to the b-c plane, but they would tend to follow the one-dimensional paths of ions if the interactions between polarons and ions are strong. We performed a series of Monte Carlo (MC) simulations on a coupled pair of one-dimensional chains. As shown in Fig. 5.2, one chain contained Li^+ ions, and the other contained electron polarons. The goal of these simulations was to estimate the strength of the polaron-ion interaction by comparing the simulated electron dynamics under pressure to the valence fluctuations measured by nuclear resonant scattering.

The hop of a Li^+ ion requires an empty site at an adjacent position on the ion chain, so ion diffusion was assumed to occur by a vacancy mechanism. Likewise, an electron-polaron at an Fe^{2+} site requires a neighboring Fe^{3+} on the same chain for the electron to hop, so a vacancy mechanism was used for the electron dynamics as well. Activated state rate theory was used to calculate jump probabilities of the ions and electrons. The activation barrier for the ion depended only on the initial configuration, but in the adiabatic approximation the electron samples the initial and final state energies before making a transition.

Each chain depicted in Fig. 5.2 had 3000 sites and periodic boundaries. Half of the sites on each chain were initially populated at random, one with Li^+ ions, and the other chain with electrons. Both species moved along their respective chains by a vacancy-type mechanism. For each step in

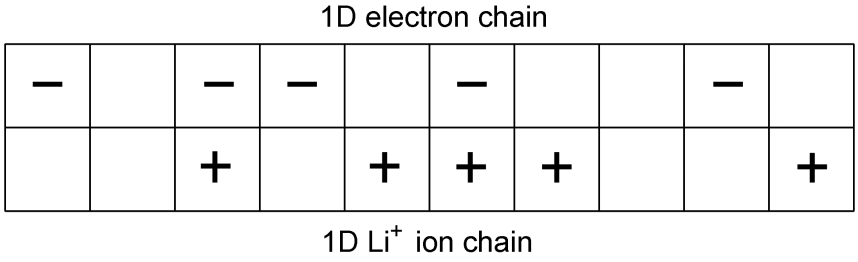

Figure 5.2. Schematic of randomly populated 1D coupled Li^+ ion and electron chains.

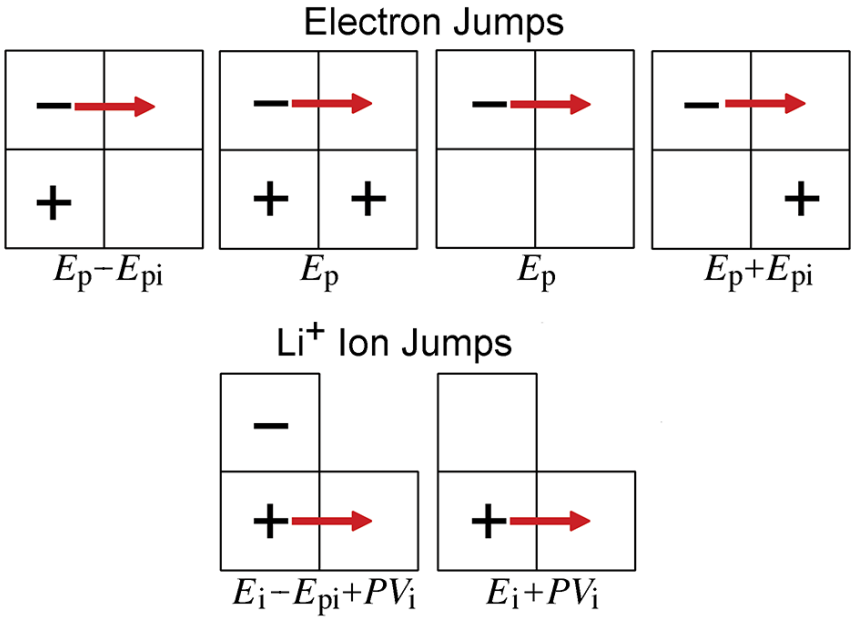

Figure 5.3. Six subprocesses describing ion and electron jumps on coupled 1D chains, where the energy barrier for each subprocess is listed below the schematic. E_p and E_i are the free polaron and ion activation barriers respectively, E_{pi} is the polaron-ion interaction energy, and V_i is the activation volume for ion hopping. For Li^+ ion jumps, depicted in the lower frames, the energy barrier depends only on the initial 1NN electron site; the final 1NN site on the electron chain is not depicted.

the simulation, every site on both chains was selected in a random sequence. If the site contained an electron or ion, the probability that a jump will occur was calculated using Boltzmann factors, described below, for T = 573 K. The time was obtained as a running sum of the inverse of the Boltzmann factors of the jumps that occurred.

The energies used in the Boltzmann factors are

$$\{E_{\rm i},\ E_{\rm p},\ E_{\rm pi}\}\ , \tag{5.3}$$

where the first two are activation energies for the jump of a bare (noninteracting) ion and a polaron, respectively, and the third is the polaron-ion interaction energy. For a given event, the relevent site occupancies of the electron or ion on a site were either 0 or 1, as set by four Kroneker δ-functions. For a site directly opposite on the other chain the index is 0, to its left –1, or right +1,

$$\{\delta_{0\rm p},\ \delta_{0\rm i},\ \delta_{-1\rm i},\ \delta_{+1\rm i}\}\ . \tag{5.4}$$

The two Kroneker δ-functions for the vacancy pertain to vacancies on the same chain as the moving species, which allow the jump to occur to the left or right (±1),

$$\{\delta_{-1\rm v},\ \delta_{+1\rm v}\}\ . \tag{5.5}$$

The Boltzmann factors for the four jumps to the left or right by the ion or electron-polaron are

$$B_{-1\rm i} = \delta_{-1\rm v}\exp\Big(-\beta(E_{\rm i}+PV_{\rm i}+\delta_{0\rm p}E_{\rm pi})\Big)\ , \tag{5.6}$$

$$B_{+1\rm i} = \delta_{+1\rm v}\exp\Big(-\beta(E_{\rm i}+PV_{\rm i}+\delta_{0\rm p}E_{\rm pi})\Big)\ , \tag{5.7}$$

$$B_{-1\rm p} = \delta_{-1\rm v}\exp\Big(-\beta[E_{\rm p}+(\delta_{0\rm i}-\delta_{-1\rm i})E_{\rm pi}]\Big)\ , \tag{5.8}$$

$$B_{+1\rm p} = \delta_{+1\rm v}\exp\Big(-\beta[E_{\rm p}+(\delta_{0\rm i}-\delta_{+1\rm i})E_{\rm pi}]\Big)\ , \tag{5.9}$$

where the ion jump is influenced by pressure, and depends on the presence of an electron-polaron directly opposite (subscript 0), whereas the electron jump depends on the presence of an ion directly opposite, but also opposite to its final position after the jump.

The jump probabilities were normalized by the two possibilities that could occur and the possi-

bility of no event

$$\Gamma_{-1\mathrm{i}} = \frac{B_{-1\mathrm{i}}}{1 + B_{-1\mathrm{i}} + B_{+1\mathrm{i}}}\,, \tag{5.10}$$

$$\Gamma_{+1\mathrm{i}} = \frac{B_{+1\mathrm{i}}}{1 + B_{-1\mathrm{i}} + B_{+1\mathrm{i}}}\,, \tag{5.11}$$

$$\Gamma_{-1\mathrm{p}} = \frac{B_{-1\mathrm{p}}}{1 + B_{-1\mathrm{p}} + B_{+1\mathrm{p}}}\,, \tag{5.12}$$

$$\Gamma_{+1\mathrm{p}} = \frac{B_{+1\mathrm{p}}}{1 + B_{-1\mathrm{p}} + B_{+1\mathrm{p}}}\,. \tag{5.13}$$

At each step of the simulation, the state of the chains was used to obtain the Kroneker δ-functions needed for Eqs. 5.6 through 5.9. The electron or ion under consideration moved left, right or remained stationary based on a randomly generated number, Q, between 0 and 1. For a given electron, a left jump occurred when $Q < \Gamma_{-1\mathrm{p}}$, a right jump when $\Gamma_{-1\mathrm{p}} < Q < \Gamma_{+1\mathrm{p}} + \Gamma_{-1\mathrm{p}}$, and no jump when $Q > \Gamma_{+1\mathrm{p}} + \Gamma_{-1\mathrm{p}}$. Ion jumps were determined similarly. The local change after a successful jump was used to update the state of the chains, and the inverse of the Boltzmann factor was added to the time.

For the results shown below, activation barriers were set using previous computational results for the "free-polaron" activation energy, E_{p} = 215 meV, and the activation energy for Li^+ ion diffusion, E_{i} = 270 meV [12, 74] (although many other values were tried). These activation barriers were altered by a polaron-ion interaction energy, E_{pi}, the strength of the coupling between the Li^+ ion, and the electron polaron when the two are first nearest neighbors (1NN), being at the same sites on their respective chains. First principles calculations place E_{pi} in the range of –370 meV to –500 meV, depending on the degree of lithiation, and the authors suggested that the the polaron-ion interaction could affect polaron dynamics [74]. When a Li^+ ion jumps away from a 1NN electron, the activation barrier for the jump is raised by an amount $|E_{\mathrm{pi}}|$. The quantum character of the electrons gives an activation barrier that depends on the 1NN on the Li^+ chain in both the initial and final positions. Accordingly, the electronic activation barrier is raised by an amount $|E_{\mathrm{pi}}|$ when the electron jumps away from a Li^+ 1NN, and is lowered by an amount $|E_{\mathrm{pi}}|$ for a jump into a site with a Li^+ 1NN. The possible jumps are broken down into the six subprocesses shown in Fig. 5.3.

The activation barrier for ion hopping was altered by an amount PV_{i}, where V_{i} is the activation volume for ion diffusion. An activation volume of +5 $\mathrm{Å}^3$ was used, typical of activation volumes

measured for ion diffusion in similar systems [38]. Assuming $LiFePO_4$ behaves similarly to other transition metal oxides, we expect the activation enthalpy for the hop of a bare electron polaron to decrease with pressure [30–33]. Because this effect is expected to be an order of magnitude smaller than the effect on ionic diffusion, for the purpose of these simulations we treated the activation barrier for electron hopping as pressure independent.

5.4 Results

5.4.1 Experimental results

The NFS spectra are presented in Fig. 5.4. In the 0 GPa series, with increasing temperature, especially above 400 K, the quantum beats are broadened and flattened, and the integrated count rate decreases. This washing out of the spectral features and suppression of count rate comes from a dephasing of the scattered intensity, consistent with the development of broad, asymmetric energy spectra. The temperature range of the onset of these effects is consistent with the polaron dynamics reported by conventional Mössbauer spectrometry [66]. At elevated pressures these large spectral distortions do not occur until higher temperatures, approximately 100 K higher for 3.5 GPa. Smaller changes can be seen at lower temperatures, however.

The spectra were evaluated using the software package CONUSS [50, 81]. CONUSS allows for the calculation and refinement of spectra using the theory of Blume and Tjon for random temporal fluctuations of the hyperfine field [48, 49]. Drawing on the Kubo-Anderson model of motional narrowing [47], Blume and Tjon used a correlation function, time averaged over the stochastic degrees of freedom, to evaluate the lineshapes of emitted radiation from a system with a fluctuating nuclear Hamiltonian. Depending on the relaxation time relative to the lifetime of the excited state, the effective widths of the resonance lines can either sharpen or broaden inhomogeneously and amalgamate. While the probability for a transition between the excited state and the ground state with the emission of photon is Lorentzian in form, the observed probability results from a sum over the possible ground states and a stochastic average over the sampled excited states. For polycrystalline samples, the problem reduces to the simplest case treated by Blume and Tjon in which the stochastic and quantum mechanical parts of the problem are separable as there is no issue of non-commutativity of the Hamiltonian at different times.

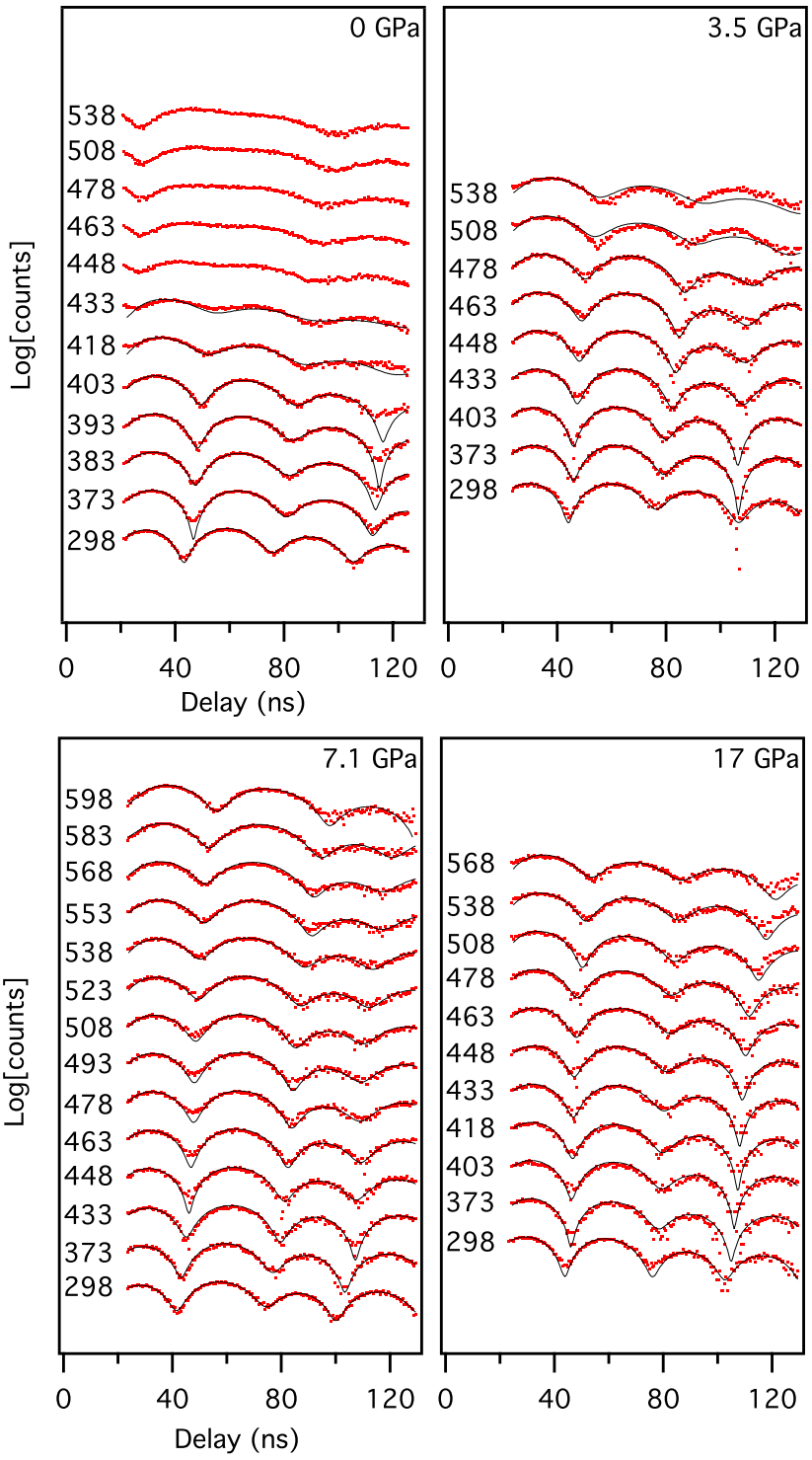

Figure 5.4. Temperature series of NFS spectra taken at 0, 3.5, 7.1 and 17 GPa. The fits (black curves) overlay experimental data (red points). Temperatures are listed to the left of spectra in Kelvin. The x-axis is the delay in nanoseconds after the arrival of the synchrotron pulse. The spectra have been scaled by their maximum value and offset for comparison.

The fluctuations from polaron hopping require two sets of hyperfine parameters for the Fe^{2+} and Fe^{3+} sites, together with a relaxation matrix of transition rates, describing the random jumps between the two sets of hyperfine parameters:

$$\mathbf{W} = \begin{bmatrix} -\Gamma\rho_{2+} & \Gamma\rho_{2+} \\ \Gamma\rho_{3+} & -\Gamma\rho_{3+} \end{bmatrix} . \tag{5.14}$$

The elements of the relaxation matrix are weighted by the populations, ρ, of the two sites, maintaining charge balance. This allows for the refinement of a QS specific to each site, a relative IS, and a polaron hopping frequency, $\Gamma(T, P)$.

The Blume-Tjon model was not used for the spectra at 298 K. These spectra were fit with a static model, allowing for the refinement of the sample thickness as well as the distribution of QS that may result from disorder in the sample and pressure gradients in the cell. The sample thickness and the distribution of QS were then fixed for the fits at elevated temperatures, minimizing problems from correlations between the hopping frequency and the distribution of quadrupole splittings (which produce similar effects at low hopping frequencies). For fitting a data set at a fixed pressure, after fixing the thickness and the distribution of the QS at their values for 298 K, four parameters were varied to fit the spectra at elevated temperatures. The refined fits overlay experimental spectra in Fig. 5.4. Most of the hyperfine parameters showed gradual changes with temperature and pressure that we summarize here with linear relationships:

QS of Fe^{2+}: $[2.9 - 2 \times 10^{-3}(T - 298)]$ mm(s K)$^{-1}$,

QS of Fe^{3+}: $[1.1 - 2 \times 10^{-3}(T - 298)]$ mm(s K)$^{-1}$,

Relative IS: $[0.8 - 10^{-3}(T - 298)]$ mm(s K)$^{-1}$,

QS of Fe^{2+}: $[2.9 + 0.04P]$ mm(s GPa)$^{-1}$,

QS of Fe^{3+}: $[1.1 + 0.04P]$ mm(s GPa)$^{-1}$.

The relative IS (IS Fe^{2+} – IS Fe^{3+}) did not show a discernible trend with pressure. These parameters are consistent with those determined using conventional Mössbauer spectrometry for the same material [65, 66]. The data and fits in Fig. 5.4 are plotted on a logarithmic scale. The fitting algorithm uses a least squares criterion, so the fit discrepancies in the regions of the lowest count rate (most notably the third minima) are smaller than they appear and do not significantly affect the quality of

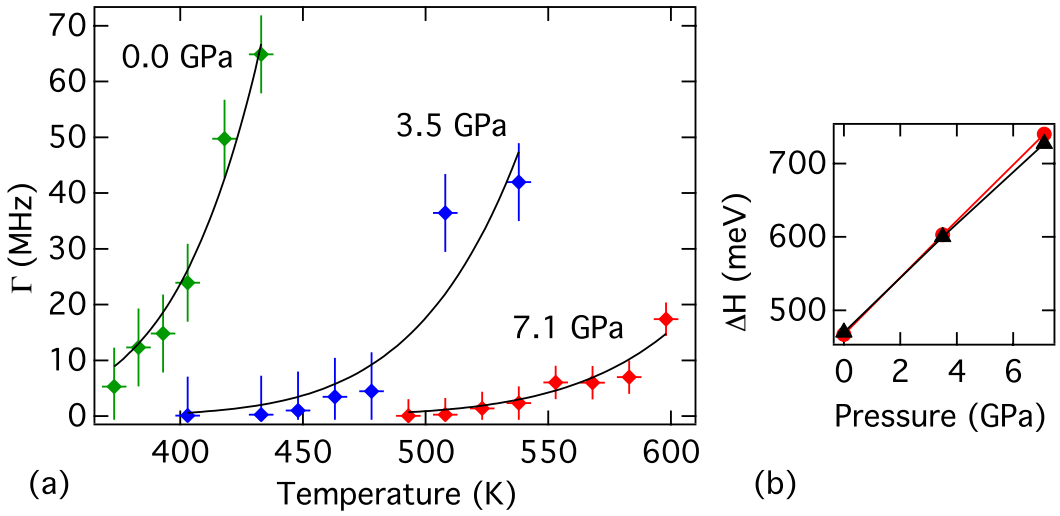

Figure 5.5. (**a**) Polaron hopping frequencies, $\Gamma(T, P)$, at 0, 3.5 and 7.1 GPa, as determined from the solid curves of Fig. 5.4. Solid curves are Arrhenius-type fits using a pressure-independent prefactor. (**b**) Activation enthalpies, $\Delta H = E_a + PV_a$, versus pressure, where $E_a = 470$ meV. Black triangles are results for fixed prefactor and red circles are for a pressure dependent prefactor.

the fits.

Figure 5.5(a) shows the polaron hopping frequencies, $\Gamma(T, P)$, determined from the fits to the spectra of Fig. 5.4. For frequencies below approximately 1 MHz, the spectra are fit equally well with a static model. In this low-frequency limit, a static spectrum and a dynamic spectrum are identical, all else held constant. For the 17 GPa series, the hopping frequencies for the entire temperature series were below this threshold. The suppression of hopping frequencies at moderate pressures indicates that V_a is positive and large. The three data sets in Fig. 5.5(a) were fit simultaneously with Eq. 5.1 to determine the activation enthalpies and the prefactor. From the ambient pressure series, the activation energy was found to be 470 ± 50 meV, where the uncertainty arises from the weighting of the different data points in linear or logarithmic fits, and the choice a prefactor for Eq. 5.1. This is comparable to the values of 512, 550, and 570 meV for activation energies of hyperfine parameters from the same material measured by conventional Mössbauer spectrometry [65].

The prefactor was first assumed independent of pressure. The result, $\sim 10^{13}$ Hz, is typical of optical phonon frequencies measured by inelastic neutron scattering and by Raman spectrometry [82, 83]. For a second set of fits, we calculated the pressure dependence of the prefactor, $\nu \exp(-2\alpha R)$. We extrapolated the attempt frequency to elevated pressure using a typical

Grüneisen parameter, $\gamma = 2$, and the compressibility, κ_T,

$$\nu(P) \simeq \nu_0(1 + \gamma P \kappa_T) \ . \tag{5.15}$$

The wave function overlap was approximated assuming a pressure-independent localization length

$$\exp[-2\alpha R] \simeq \exp[-2\alpha R_0(1 - P\kappa_T/3)] \ , \tag{5.16}$$

where R_0 is the ambient pressure inter-cation distance. X-ray diffractometry measurements at 300 K on an olivine $Li_{0.6}FePO_4$ solid solution at pressures up to 32 GPa gave a bulk modulus of 120±4 GPa [78]. This is somewhat larger than for Li_1FePO_4, with bulk modulus measured as 106±8 GPa, and calculated as 96 GPa [84]. These additional considerations did not significantly affect the results below for V_a.

From Eqs. 5.1, 5.15 and 5.16, V_a can be determined from the pressure dependence of the activation enthalpy. For a given pressure, we determine the activation enthalpy by looking at the linear part of $\ln(\Gamma)$ as a function of β, where $\beta = 1/(k_B T)$ [31].

$$\ln(\Gamma) = -\beta \Delta H - 2\alpha R + \ln(\nu) \ , \tag{5.17}$$

$$\Delta H \simeq -\left(\frac{\partial \ln(\Gamma)}{\partial \beta}\right)_P \ . \tag{5.18}$$

To account for any pressure dependence of the prefactor of Eq. 5.1, we consider the pressure dependence of the last two terms in Eq. 5.17. Assuming these terms are independent of temperature, Eqs. 5.15 and 5.16 can be used to correct the V_a obtained from the jump rates, $\Gamma(T, P)$,

$$V_a = \left(\frac{\partial \Delta H}{\partial P}\right) \ , \tag{5.19}$$

$$V_a \approx -\frac{\partial \left(\frac{\partial \ln \Gamma}{\partial \beta}\right)_P}{\partial P} + \frac{2\,\alpha R_0\,\kappa_T}{3\,\beta} + \frac{\gamma \kappa_T}{\beta} \ . \tag{5.20}$$

The dominant source of error in the determination of the enthalpies lies in the choice of a prefactor for Eq. 5.1. Constraining the prefactor to a reasonable range based on past measurements of optical phonons [82, 83, 85] gives an error in the magnitude of the activation enthalpies of approximately

$\pm 10\%$. The slope of the curve in Fig. 5.5(b) gives an activation volume of +5.8$\pm$0.7 Å^3. The second and third terms of Eq. 5.20 are an order of magnitude smaller than the first term from the slope of Fig. 5.5(b), but will increase V_a above the value of +5.8 Å^3. Our V_a is between one and two orders of magnitude larger than previously reported polaron activation volumes from resistivity measurements on oxides [30–33].

5.4.2 Simulational results

Polaron jump frequencies were calculated as a function of pressure, assuming these frequencies were proportional to Boltzmann factors with thermal activations. The activation energies were taken as the appropriate combination of $E_{\rm p}$, $E_{\rm i}$, and $E_{\rm pi}$, depending on their local configurations. The activation energy for an ion jump was increased with pressure by $PV_{\rm i}$, where $V_{\rm i}$ was +5 Å^3 and P was 0, 3 or 7 GPa. We used values of $E_{\rm p} = 215$ meV and $E_{\rm i} = 270$ meV as reported in the literature [12, 74], but we also calculated frequencies using several other activation barriers ranging from 50% to 200% of these values.

For simulations with $|E_{\rm pi}|$ greater than 100 meV, after a quick initial relaxation, more than 90% of the electrons were paired to a Li^+ across the coupled chains. By inspecting the jump probabilities of Eqs. 5.10 – 5.13, we found that $E_{\rm pi}$ = –300 meV could account for the experimental trend in the pressure-induced suppression of the polaron jump frequency at $T = 573$ K. Nevertheless, values of $E_{\rm pi}$ from –200 to over –400 meV gave similar results.

In the MC simulations, we monitored the mean-squared displacement (MSD) of both species as a function of pressure and $E_{\rm pi}$. Our interest was how the electron MSD was altered under pressure as a result of suppressed ionic mobility. The simulations varied the ionic mobility while monitoring the effect on the electronic mobility. The activation barrier for electron hopping was pressure independent, so raising the activation barrier for ion hopping (through pressure) has no effect on the electron MSD when the ion and electron chains are decoupled ($E_{\rm pi}$=0). When a coupling is introduced, an indirect effect on the electron mobility is observed with increasing $|E_{\rm pi}|$. Figure 5.6 presents typical results of such a series of simulations. The electron MSD increases approximately as $t^{0.5}$. This exponent is well-known when particles cannot pass on a 1D chain and require concentration fluctuations to move forward [86]. A suppression of the MSD with pressure clearly emerges for values of $E_{\rm pi}$ less than –200 meV and becomes increasingly pronounced as the magnitude of

$E_{\rm pi}$ is increased. For a polaron-ion interaction energy of –250 meV at 3 GPa the MSD is suppressed by 45% and at 7 GPa the MSD is suppressed an additional 40%. For agreement with experiment, it appears that $E_{\rm pi}$ for $LiFePO_4$ is between –200 and –300 meV. Larger magnitude values are not ruled out, however. The effects of pressure on the polaron jump frequency saturated when $|E_{\rm pi}|$ was somewhat larger than $E_{\rm p}$. It was also noted that the effects of pressure on the polaron jump rate became larger as $E_{\rm i}$ decreased relative to $E_{\rm p}$, consistent with a larger role of ion motion in the overall dynamics.

5.5 Discussion

Holstein's molecular crystal model captures the essential physics of small polaron formation and dynamics [1, 28, 87]. A tight-binding model is used to describe an extra electron in an array of N molecules, each with an internuclear distortion variable, x_n, and a reduced mass M, where $M^{-1} = N^{-1}\sum_{\rm ions} m^{-1}$. The positive strain energy is quadratic in the x_n (e.g., the interatomic separation of two ions in a diatomic molecule) with harmonic oscillator frequency, ω_0, associated with the configurational coordinate of an isolated molecule. The electronic energy is reduced linearly with x_n in proportion to the strength of an electron-phonon interaction parameter, A, that characterizes the electron-lattice coupling strength in units of force.

A finite local distortion, x_n, results in a reduced potential that effectively pins the electron, so the localized polaron is favored by the binding energy, E_b, relative to an electron in an undeformed lattice,

$$E_b \approx \frac{A^2}{2M\omega_0^2} \; . \tag{5.21}$$

In the adiabatic limit, the prefactor in Eq. 5.1 reduces to the mean optical phonon frequency and the activation energy is lowered by an amount J, associated with the d-bandwidth [30],

$$E_a = \frac{E_b}{2} - J \; . \tag{5.22}$$

The activation energy depends on pressure through the exchange integral, J, as well as any pressure dependence of the binding energy. Taking the activation volume as the pressure derivative of the activation energy,

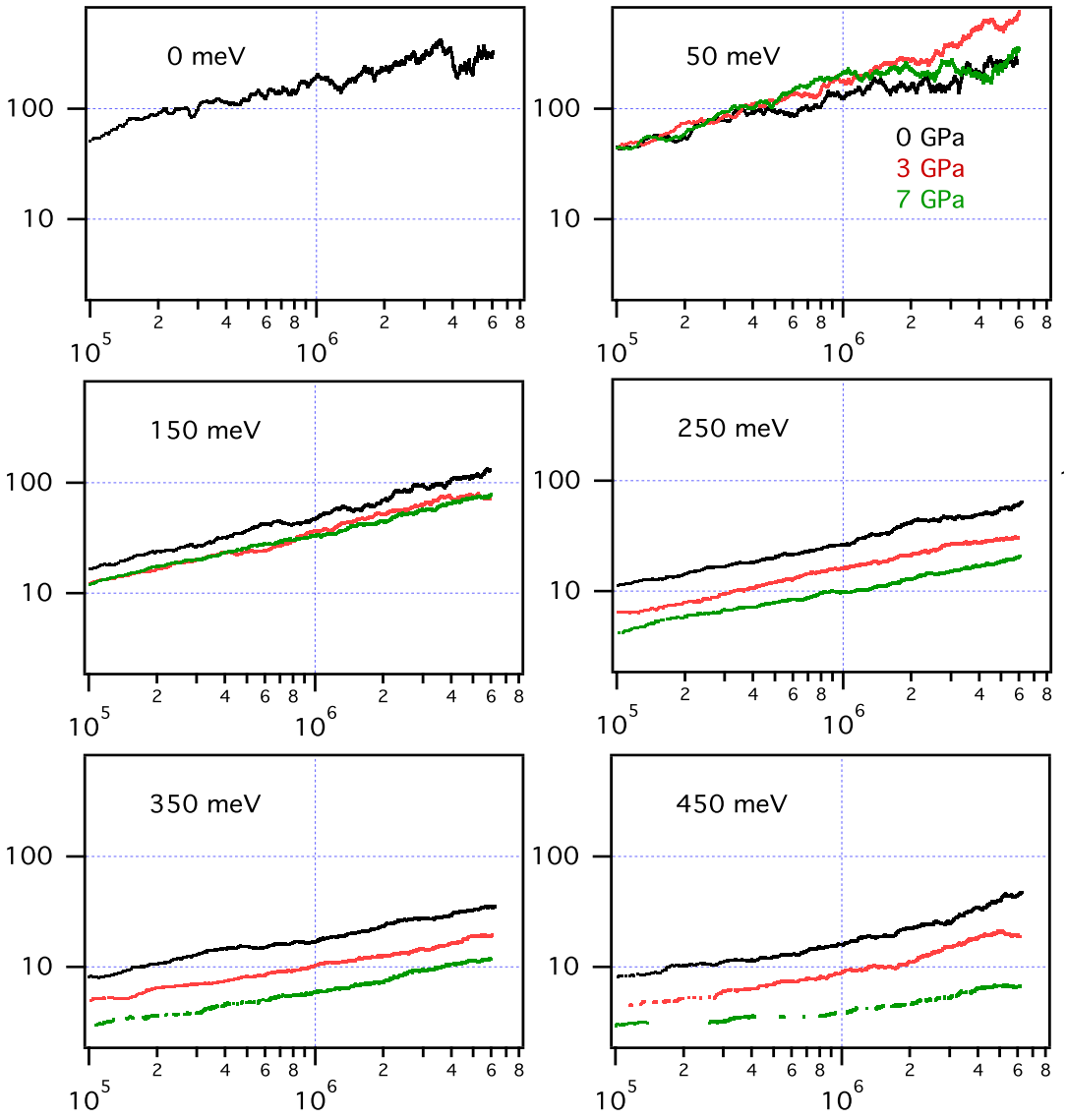

Figure 5.6. Electron MSD versus time for six series of MC simulations for a pair of coupled 1D ion and electron chains. Units for MSD are site index squared. Time is dimensionless. Each subplot shows the results for a different $E_{\rm pi}$. Subplots are labeled with -$E_{\rm pi}$ (0, 50, 150, 250, 350 and 450 meV). In each series, the MSD is shown for three different pressures: 0 (black), 3 (red) and 7 GPa (green).

$$V_a = \frac{\partial E_a}{\partial P} \approx E_b \left(\frac{1}{A}\frac{\partial A}{\partial P} - \frac{1}{\omega_0}\frac{\partial \omega_0}{\partial P} \right) - \frac{\partial J}{\partial P}, \tag{5.23}$$

and using the definition of the compressibility and the Grüneisen parameter, γ, the activation volume becomes,

$$V_a \approx E_b \left(\frac{1}{A}\frac{\partial A}{\partial P} - \gamma\kappa_T \right) - \frac{\partial J}{\partial P} \ . \tag{5.24}$$

The last term, from the increased wave-function overlap, is positive, and tends to destabilize the localized polaron. This term is believed to be responsible for the negative activation volumes in other polaronic conductors [30]. Our large, positive V_a would be consistent with an effect of pressure on the electron-phonon interaction parameter, A, if $\partial A/\partial P > 0$, giving $\partial E_b/\partial P > 0$ by Eq. 5.21. In general, however, we expect destabilization of an electron polaron centered at a Fe^{2+} ion because the compressibility of ferrous-oxygen bonds is greater than for ferric-oxygen bonds. First principles calculations suggest the activation barrier is raised by $\sim$50 meV under 4% biaxial compression (along the b and c axes) [88]. The authors attribute this effect to an enhancement of the electron-phonon coupling. Frozen phonon calculations for the strained system show the electron phonon coupling constant increases by more than 20% [88]. These effects on the activation barrier from standard polaron models are too small, or of the wrong sign, to account for our experimental results.

The electron-phonon interaction could be affected by the electrostatic interaction between the polaron and a nearby Li^+ ion if the ion has a pressure-dependent mobility. We suggest the origin of our large difference between the activation volume measured for $LiFePO_4$ and previous activation volumes determined using conductivity measurements on oxides without mobile ions is the strong coupling between the polarons and the mobile Li^+ ions, $E_{\rm pi}$.

Previous first principles calculations for polaron hopping in $LiFePO_4$ gave activation energies of 175 and 215 meV for electron and hole polarons, respectively [74]. These results are for free-polaron transport. Measured activation energies, from either Mössbauer spectrometry or conductivity measurements, are two to three times higher than these calculated values. This is consistent with a tendency for the electrons on Fe^{2+} sites to remain near Li^+ ions.

The effect of pressure on valence fluctuations at Fe sites is indirect, but potentially large. It is well known that pressure suppresses ionic diffusion by a vacancy mechanism [as in Eqs. 5.6 and 5.7]. The MC simulations show how polaron dynamics are suppressed if the polaron-ion interac-

tion energy tends to attract the polaron to immobile ions. The required interaction energy, $E_{\rm pi}$, is approximately –300 meV for the pressures and temperatures of interest.

Some discrepancies deserve further investigation. Electron jumps between two sites where both have ion neighbors, or both have vacancies (middle processes at top of Fig. 5.3), are unaffected by pressure, and predict a background dynamics that is not found experimentally. In the olivine structure, electron mobility is likely confined to the b-c plane. The Fe and Li sites are staggered in a way that each Fe site has two symmetrically positioned Li sites, but within a given FeO_6 plane each Li-site has one 1NN Fe site and one second-nearest-neighbor (2NN) Fe site. A polaron following the path of closest approach to a given ion chain will necessarily alternate between these 1NN and 2NN-type sites where the Li-Fe bond length is 6% longer in the 2NN site [68]. When pressure immobilizes the Li^+ ions, there may be a tendency for electron-polarons to localize in these 1NN-type sites in such a way that local dynamics are suppressed. Alternatively, the experimental technique may not be sensitive to certain dynamics, for example, minority processes or dynamics that fall outside the window of sensitivity of frequencies sampled by Mössbauer spectrometry measurements. It is also possible that pressure suppresses other aspects of polaron dynamics, or the ions and polarons may form an ordered structure with reduced dynamics.

The generally good agreement between the experiment and simulated dynamics with a reasonable value of $E_{\rm pi}$, together with a measured activation volume of +5.8 Å^3, consistent with ion diffusion, indicate a strong coupling between the ions and polarons in Li_xFePO_4. A transport of net charge requires decoupling of the ion and polaron motions, however, so the coupling is not immutable. Nevertheless, the correlated motions of electrons and ions should suppress electrical conductivity in $LiFePO_4$. Furthermore, a large correlation in the motions of polarons and ions can explain why the electrical conductivity of $LiFePO_4$ is so sensitive to materials preparation. Because Li^+ diffusion in $LiFePO_4$ is essentially one dimensional, Li^+ ion mobility suffers as a result of channel blockage by defects [11, 12]. Blocked channels for Li^+ ions then suppress electronic conductivity if polaron-ion interactions are strong. This effect may be common in materials when both ions and electrons are mobile.

A small polaron quasiparticle comprises an electron localized by atomic contractions from neighboring anions. Both the charge and distortion of the polaron are large enough to interact with the charge and distortion around a Li^+ ion, altering the formation energy and dynamics of the

polaron. The quantum dynamics of small polaron hopping is likely modified by the classical dynamics of ion motion; likewise, the configurations of polarons and ions on the crystal lattice should also be affected by these interactions.

5.6 Conclusions

Nuclear resonant scattering spectra of Li_xFePO_4 were measured at elevated pressure and temperature. An analysis of the spectra using the Blume–Tjon model for a system with a fluctuating electric field gradient gave frequencies of Fe valence fluctuations that correspond to frequencies of polaron hopping. From measurements over a range of temperatures and pressures, both the activation energy and activation volume were determined for polaron hopping. To our knowledge this is the first measurement of an activation volume for polarons in a material with mixed ion-polaron conductivity.

Pressure caused a large suppression of valence fluctuations in Li_xFePO_4, giving an activation volume for polaron hopping of +5.8 $Å^3$. This unusually large and positive activation volume is not typical of bare polaron hopping. It indicates a correlated motion of polarons and Li^+ ions. From model calculations and Monte Carlo simulations, the binding energy between the polaron and the Li^+ ion was found to be approximately –300 meV. This strong binding and polaron-ion correlation should suppress the intrinsic electronic conductivity of Li_xFePO_4. It may also affect the diffusion of Li^+ ions. Such coupled processes may be common to other materials where both ions and polarons are mobile.

Chapter 6

Polaron mobility and disordering of the Na sublattice in Na_xFePO_4 with the triphylite structure

6.1 Introduction

Li-ion batteries have been an active subject of research within the last two decades and are now widely commercialized in consumer electronics and electric vehicles. The effort to design improved batteries has motivated the investigation of a range of polyanionic framework materials. Within this context, the phospho-olivines have emerged as particularly promising with their low toxicity, thermal stability and high energy density. The orthorhombic olivine-type structure (Pmna) is shown in Fig. 6.1(a). Layers of corner-sharing networks of canted FeO_6 octahedra in the b-c plane are spaced by phosphate tetrahedra, and alkali cations form one-dimensional chains that run between these FeO_6 planes. Previous work has shown that the predominant ion diffusion pathway is along these b-axis channels [15, 55]. In comparison, the electronic carrier mobility is expected to be two-dimensional, occurring within the layers of FeO_6 octahedra that are separated by insulating phosphate groups.

With the increasing reliance on Li-ion technology, it has become apparent that lithium itself is a limited resource. By contrast, sodium is one of the major rock-forming elements in the Earth's crust, and consequently is both environmentally abundant and relatively affordable. As a result, the

idea of designing sodium analogues to lithium cathode materials is immensely appealing, especially for large energy-storage systems. The sodium counterpart to $LiFePO_4$ has attracted attention as a particularly promising sodium cathode [16–18, 26, 89–94]. The ground-state of $NaFePO_4$ has the maricite structure. Compared to the triphylite structure favored by Li_xFePO_4, the site occupancies of the alkali ion are swapped with the iron cations. The sodium cations are then isolated by the phosphate groups, and the maricite structure is electrochemically inactive. While density functional theory calculations suggest the energy of the two polymorphs is similar [15], the maricite structure is apparently favored at higher temperatures where the material is formed. However, recent results have shown that it is possible to synthesize a sodiated triphylite structure using an ion-exchange route [89] starting with $LiFePO_4$. The triphylite-$NaFePO_4$ exhibits excellent electrochemical performance compared to other candidate sodium-ion cathode materials [17, 18].

The phase diagram for the triphylite-M_xFePO_4 (M=Na, Li) framework is altered when Na^+ replaces Li^+ as the intercalation ion. While the Li_xFePO_4 phase diagram shows a broad solid solution above 473 K [23, 24], a solid solution of Na^+ ions forms only above x=2/3, but is stable at low temperatures. Below x=2/3 there exists an intermediate ordered phase, which persists to high temperatures [16]. The proposed structure of the intermediate phase is shown in Fig. 6.1(b). This superstructure results from a vacancy at every third sodium site along the Pmna b-axis, giving rise to three crystallographically distinct iron sites, shown in red, green and blue in Fig. 6.1(b). These distinctions in phase behavior are likely a result of the larger size of the sodium cation, having a nearly 30% larger ionic radius than lithium. Full sodiation of the $FePO_4$ lattice results in a 17% volume expansion, compared to the 7% expansion seen in $LiFePO_4$ [16]. This large lattice mismatch between the end members in Na_xFePO_4 may play a role in the stabilization of the intermediate ordered phase.

As with many other transition metal oxides, the mechanism of electrical conductivity in mixed valent $M_xFe^{2+}_xFe^{3+}_{1-x}PO_4$ is small polaron hopping [65–67]. A small polaron quasiparticle comprises an electron or hole localized by atomic displacements of neighboring anions. When the carrier transfers between adjacent iron sites, this local distortion must also transfer, resulting in a slow moving particle with a large effective mass. In contrast to semi-free carriers, polarons tend to have a low mobility that rises with increasing temperature. At moderate temperatures, the motion

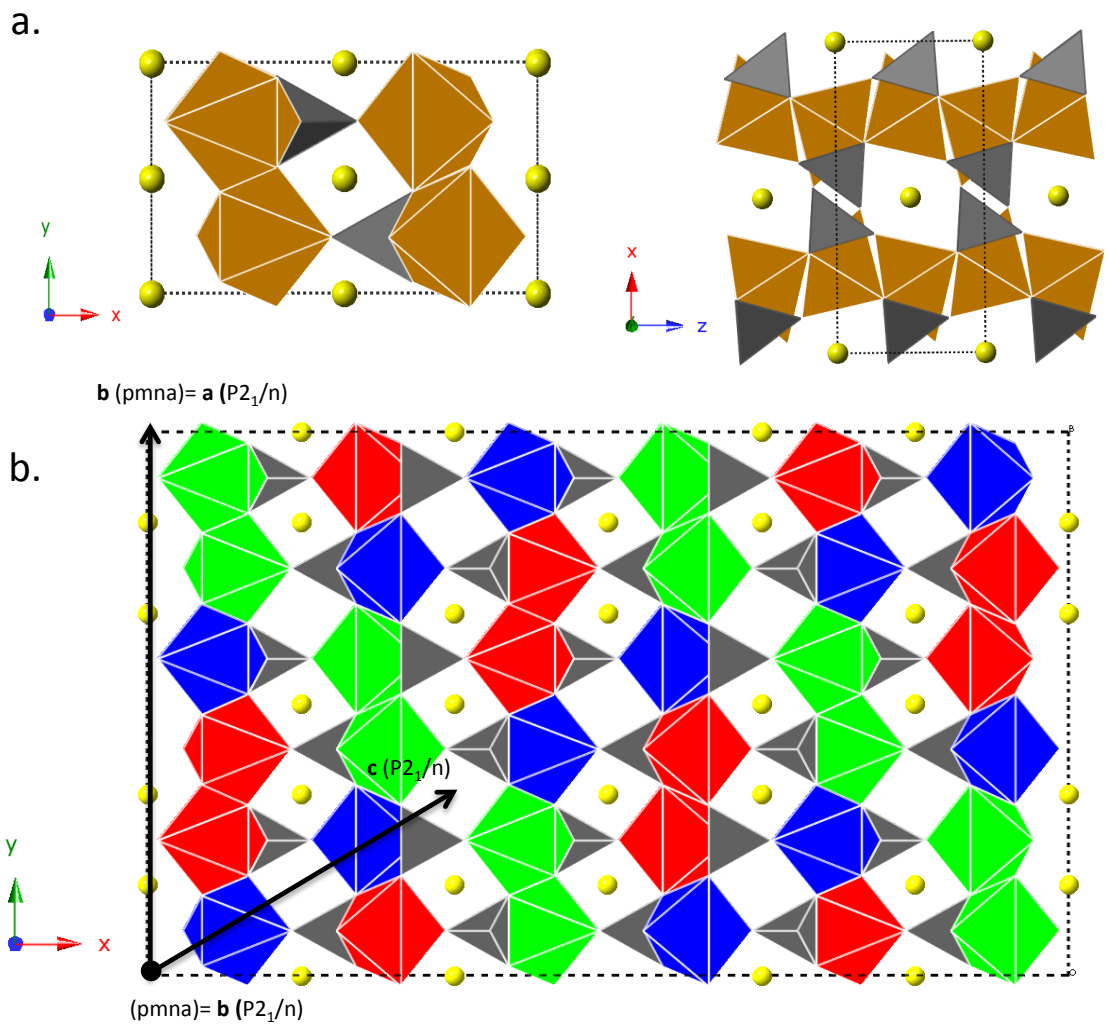

Figure 6.1. (a) Triphylite-type structure of $MFePO_4$ (M= Li, Na) with chains of M^+ ions (yellow), planes of FeO_6 octahedra (brown) and phosphate tetrahedra (grey). (b) Ordered superstructure for x=2/3. Three structurally distinct iron sites are shown in blue, green and red. The axes on left are for the orthorhombic Pmna cell. Oblique axes of $P2_1/n$ cell are shown in black.

of the polaron quasiparticle can be understood as an activated process with the jump rate [37, 69],

$$\Gamma(T) \sim \nu \exp\left(-\frac{E_a}{k_B T}\right) , \tag{6.1}$$

where T is temperature, k_B is the Boltzmann constant and ν is a characteristic phonon frequency. The activation energy, E_a, describes the energetic barrier for the polaron quasiparticle to transfer between adjacent iron sites.

Mössbauer spectrometry allows for the study of local electron dynamics at iron ions. Polaron hopping between Fe^{2+} and Fe^{3+} results in ^{57}Fe ions that experience a fluctuating local environment. The measured spectra are altered when the hyperfine fields fluctuate on the same time scale as the ^{57}Fe nuclear decay, or near a characteristic frequency set by the spectral hyperfine energies, $\nu_{HF} = \Delta E_{HF}/\hbar$. Fortuitously, typical quadrupole splittings for ^{57}Fe fall within a range that is well suited to the study of polaron dynamics, and the temperature evolution of the valence fluctuation frequencies gives rise to variations of the shape and symmetry of the quadrupole doublets from Fe^{2+} and Fe^{3+}. At low frequencies and low temperatures, the spectral components from Fe^{2+} and Fe^{3+} remain distinct, and at very high frequencies the spectrum approaches a single time-averaged doublet. More complex behavior occurs between these limits, when the valence of a ^{57}Fe ion fluctuates between Fe^{2+} and Fe^{3+} at a frequency between 1 and 100 MHz. Within this range, the quadrupole doublets from Fe^{2+} and Fe^{3+} merge together, with asymmetric, non-Lorentzian lineshapes. Previous Mössbauer spectrometry studies of the lithium analogue, Li_xFePO_4, reported dramatic spectral distortions for temperatures between 373 and 513 K [65, 66, 95].

The structure and stability of the intermediate phase at x=2/3 has been addressed in a handful of recent papers, but a comprehensive understanding of the crystallographic ordering of Na-ions and electrons is lacking. The origin of a secondary ferrous doublet in the Mössbauer spectra and how this relates to the crystallographic ordering of Na-ions and electrons or the presence of fast electron hopping is unsettled [16, 26]. Here we report new results on the phase stability and charge dynamics in $Na_{0.73}FePO_4$ at elevated temperatures, obtained by performing measurements in a resistive furnace. The evolution of the iron site occupancies with temperature, as determined from Mössbauer spectrometry, gives new information that helps resolve the nature of the ordering in the intermediate phase. Mössbauer spectrometry coupled with synchrotron x-ray diffraction shows

that the disordering of sodium ions at above 450 K and the onset of rapid electron dynamics occur simultaneously. We suggest that there is a polaron-ion interaction that affects the dynamics of both, much as is the case for Li_xFePO_4 [95].

6.2 Experimental

$LiFePO_4$ was prepared by a solid-state reaction and chemically delithiated using $K_2S_2O_8$ in an aqueous solution [23, 79]. To chemically insert sodium into the lattice, the sample was refluxed for 48 hours in an acetonitrile solution of excess NaI [92]. The resulting sample retained a minor amount of ferric iron, ranging from 3-10%. The sodiated sample was subsequently oxidized with $K_2S_2O_8$ to give a final composition of $Na_{0.73}FePO_4$.

$$\begin{aligned} LiFePO_4 + \frac{1}{2}K_2S_2O_8 &\rightarrow FePO_4 + \frac{1}{2}(Li_2SO_4 + K_2SO_4), \\ FePO_4 + \frac{3z}{2}NaI &\rightarrow Na_zFePO_4 + \frac{z}{2}NaI_3, \\ Na_xFePO_4 + \frac{(x-z)}{2}K_2S_2O_8 &\rightarrow Na_zFePO_4 + \frac{(x-z)}{2}(Li_2SO_4 + K_2SO_4). \end{aligned} \tag{6.2}$$

X-ray diffraction of the final sample shows no evidence of residual $FePO_4$. The concentration of the final sample was determined using the spectral area ratios determined from Mössbauer spectrometry.

Synchrotron X-ray diffraction (XRD) measurements were performed at beamline 16ID-D at the Advanced Photon Source at Argonne National Laboratory using a monochromatic beam with $\lambda = 0.86$ Å. Diffraction was measured in transmission geometry using a Mar CCD detector plate while the sample was held in a resistively heated vacuum furnace.

Mössbauer spectra were collected in transmission geometry using a constant acceleration system with a ^{57}Co in Rh γ-ray source. Velocity and isomer shift calibrations were performed in reference to room temperature α-iron. Elevated temperature Mössbauer spectrometry was performed with the sample mounted in a resistive furnace for a series of temperatures between 298 K and 550 K. At each temperature, the furnace was given four hours to equilibrate, after which the spectrum was collected for 20 hours. After collecting the 550 K spectra, an additional 298 K spectrum was collected and x-ray diffraction was performed on the retrieved sample.

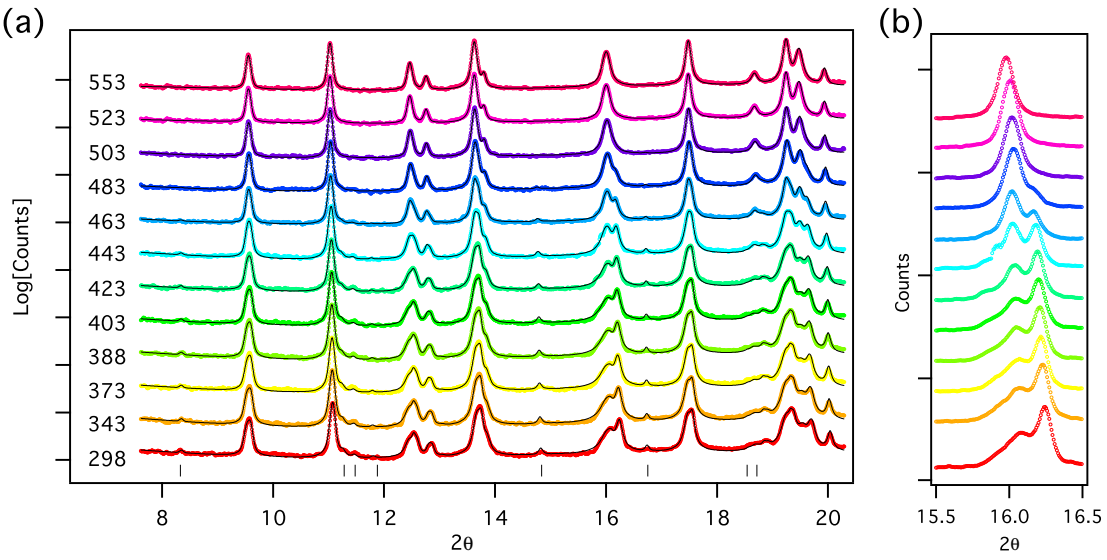

Figure 6.2. (a) Temperature series of XRD spectra taken between 295 K and 550 K. The Rietveld fits (black curves) overlay experimental data (points). Black tick marks at bottom of figure indicate locations of superstructure phase in ordered structure. (b) Enlargement of (200) peak on linear scale.

6.3 Results

6.3.1 X-ray diffractometry

Figure 6.2(a) shows the synchrotron x-ray diffraction (XRD) spectra collected at temperatures between 298 K and 553 K. The locations of the superstructure peaks from Na^+ ordering are indicated with tick marks below the 298 K spectra. Based on the phase diagram by Lu, et al. [16], the present sample (x= 0.73) should be within the solid solution phase at room temperature, but the presence of the superstructure peaks suggests that long range order persists well above x=2/3. Upon heating, the superstructure peaks become increasingly diffuse and are completely gone by 483 K. This is especially clear for the superstructure peak at ~ 15 degrees.

As the sodium disorders on the lattice, structural changes can also be seen through a closer inspection of the fundamental peaks, particularly those peaks that are sensitive to the changes in the Pmna b-axis. Inserting sodium into the $Na_{2/3}$FePO4 superstructure results in a large expansion of the b- and a-axes. A closeup of the Pmna (020) peak is shown in of the Figure 6.2(b). At 298 K this peak has a clear low-angle shoulder. The higher-angle component corresponds to the expected d-spacing for the ordered structure. As the temperature increases, the relative intensity of this shoulder increases, and above 500 K the entire weight of the (200) peak has shifted to the lower-

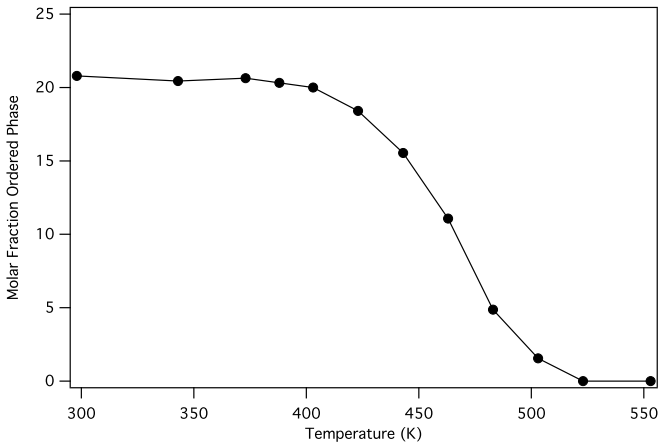

Figure 6.3. Molar fraction of x=2/3 ordered phase, determined from Rietveld analysis of x-ray patterns shown in Fig. 6.2

angle position. Similar effects can be seen in the (220) and (121) peaks with increasing temperature. The presence of this shoulder suggests that the region above x=2/3 is actually biphasic at room temperature, containing a solid solution phase as well as the x=2/3 ordered phase. This finding confirms previous XRD results as a function of desodiation by Galceran, et al. [92]. Their study showed an abrupt discontinuity in the b-axis at compositions above x=2/3, suggesting the onset of ordering starts above a composition of x=2/3. Additionally, an inspection of the room temperature XRD collected by Lu, et al. [16] reveals the (020) diffraction does not entirely disappear until x= 0.8. These observations, combined with our high temperature XRD, are evidence for an appreciable two-phase region of the phase diagram between the x=2/3 intermediate phase and a solid solution of higher concentration.

Reitveld analysis was performed with the software package GSAS, using psedo-Voigt peak profiles [40,41]. The fits to the spectra are shown as solid lines in Fig. 6.2. The instrumental broadening was modeled as Gaussian, while the strain broadening was assumed to be entirely Lorentzian. For accurate peak shapes, a Stephens model for anisotropic strain broadening was included [42]. The data were fit with two diffraction patterns, one from a solid solution phase and the other from the ordered phase, using the superstructure proposed by Boucher, et al. [26]. The ordered structure can be described by a 3x3x1 orthorhombic supercell with a Na-vacancy at every third site along the Pmna b-axis. This unit cell is equivalently described by the monoclinic $P2_1/n$ system. Both unit cells are shown in Fig. 6.1 (b). The sodium concentration of the ordered phase was fixed at x=2/3, and the sodium concentration of the solid solution was constrained so the total sodium concentration was

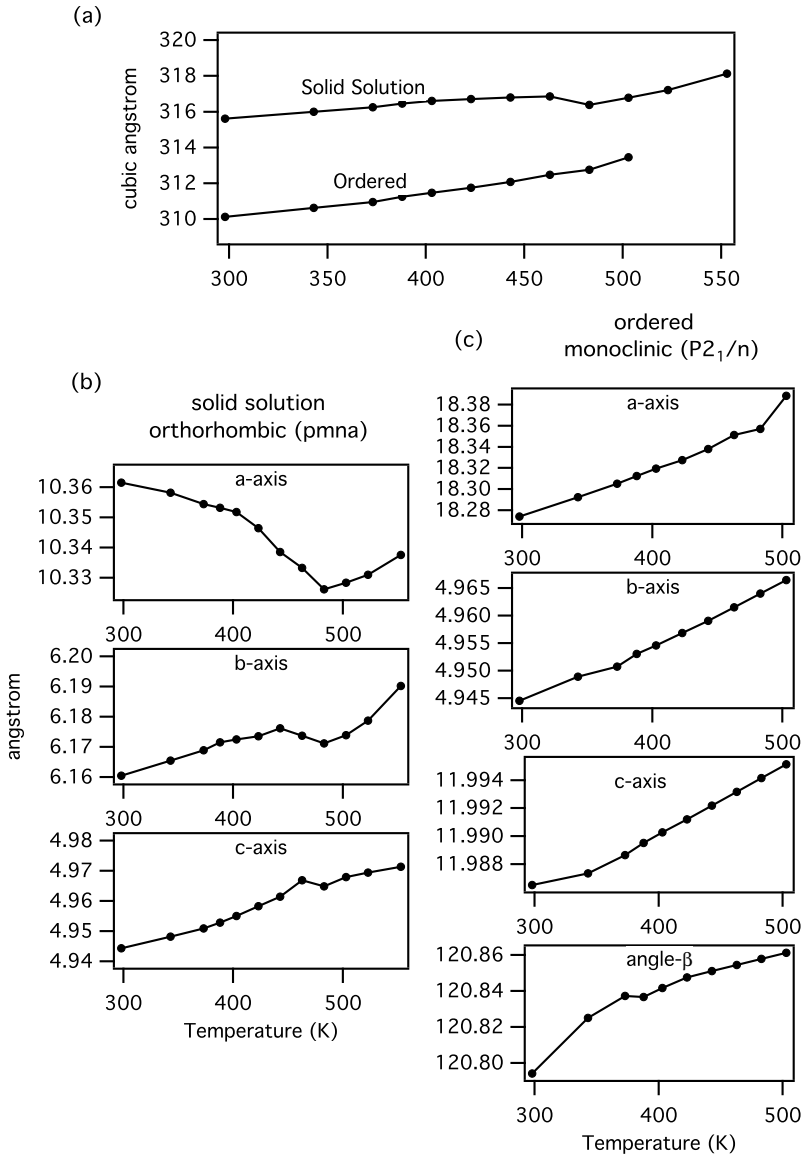

Figure 6.4. Structural parameters determined from Rietveld fits in Fig. 6.2. (a) Volume of unit cell for ordered and solid solution phases. Volume of ordered ($P2_1/n$) cell has been normalized by a factor of three for comparison with orthorhombic Pmna cell. (b) Lattice parameters for orthorhombic solid solution phase. (c) Lattice parameters for monoclinic ordered phase. The $P2_1/n$ a-axis coincides with the Pmna b-axis and the $P2_1/n$ b-axis coincides with the Pmna c-axis.

fixed at 73%.

Figure 6.3 shows the molar fraction of the x=2/3 ordered phase as a function of temperature, as determined from the Reitveld refinements. Between 298 and 400 K the molar fraction is around 20%. Above 420 K, the fraction of ordered phase drops substantially and is totally gone at 520 K. Fig 6.4(a) shows the thermal trend of unit cell volume for both phases. Here the volume of the $P2_1/n$ cell has been normalized by a factor of three for comparison with the orthorhombic cell. There is a clear volume collapse between 463 and 483 K in the solid solution phase. Fig. 6.4(b) shows the lattice parameters for the orthorhombic solid solution phase and the ordered phase, using the monoclinic crystal system. In the solid solution, between 298 and 483 K the a-axis shows a gradual contraction, above which it starts to expand. The other two axes exhibit thermal expansion throughout the entire temperature range, although both axes also show a discontinuity between 443 and 483 K.

6.3.2 Mössbauer spectrometry

Mössbauer spectra, collected in the same temperature range, are presented in Fig. 6.5. The room temperature spectrum has two distinct ferrous components with quadrupole splittings of 2.6 and 1.7 mm/s. In what follows, these are called A- and B-type sites, respectively. A fit to the 298 K spectrum gives an area ratio of the two components, B/A ∼20/80. The presence of this secondary Fe^{2+} component is consistent with other recent Mössbauer studies of this system [16,26]. A spectrum of the same sample, collected prior to chemical desodiation, exhibited a single doublet with a splitting of 2.74 mm/s, shown in Fig. 6.6 (c). This "fully sodiated" sample contained a residual ferric concentration of ∼3%. Two additional samples were prepared with concentrations of $x = 0.54$ and $x = 0.67$. Room temperature spectra for these samples are shown in Figs. 6.6(a) and (b), respectively. Fits to these spectra gave B/A site area ratios of ∼34/66.

The spectra were evaluated using the software package CONUSS [50, 81], which generated the solid curves in Fig. 6.5. CONUSS allows for the calculation and refinement of spectra using the theory of Blume and Tjon for random temporal fluctuations of the hyperfine field [48, 49]. This model uses a time average over the stochastic degrees of freedom of the fluctuating nuclear Hamiltonian, making use of a relaxation matrix that describes the transition rates between the two sets of hyperfine parameters associated with the Fe^{2+} and Fe^{3+} environments. Depending on the

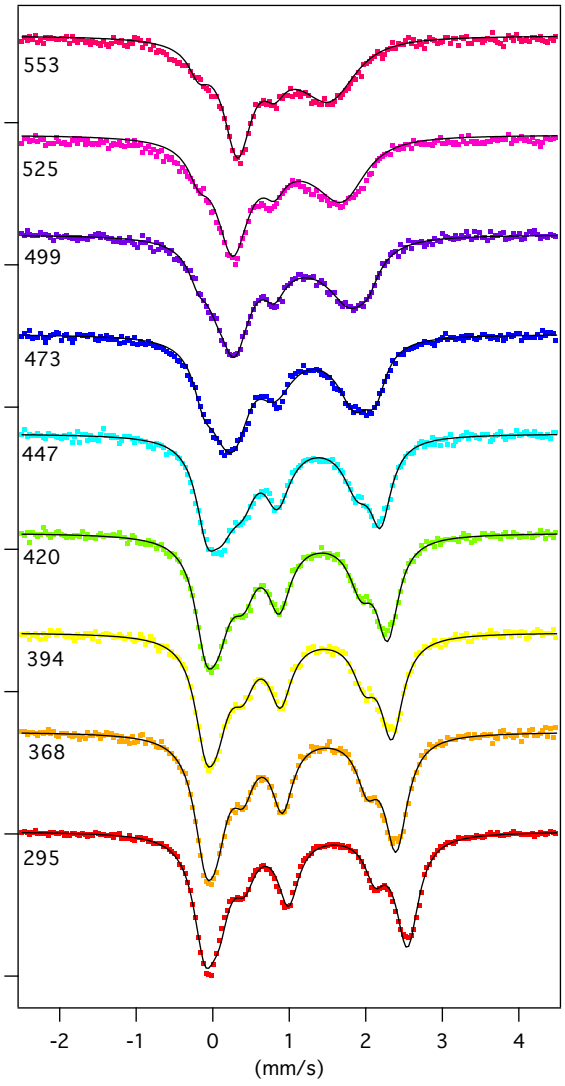

Figure 6.5. Temperature series of Mössbauer spectra taken between 295 K and 550 K. The fits (black curves) overlay experimental data (points). Temperatures are listed to the left of the spectra in Kelvin.

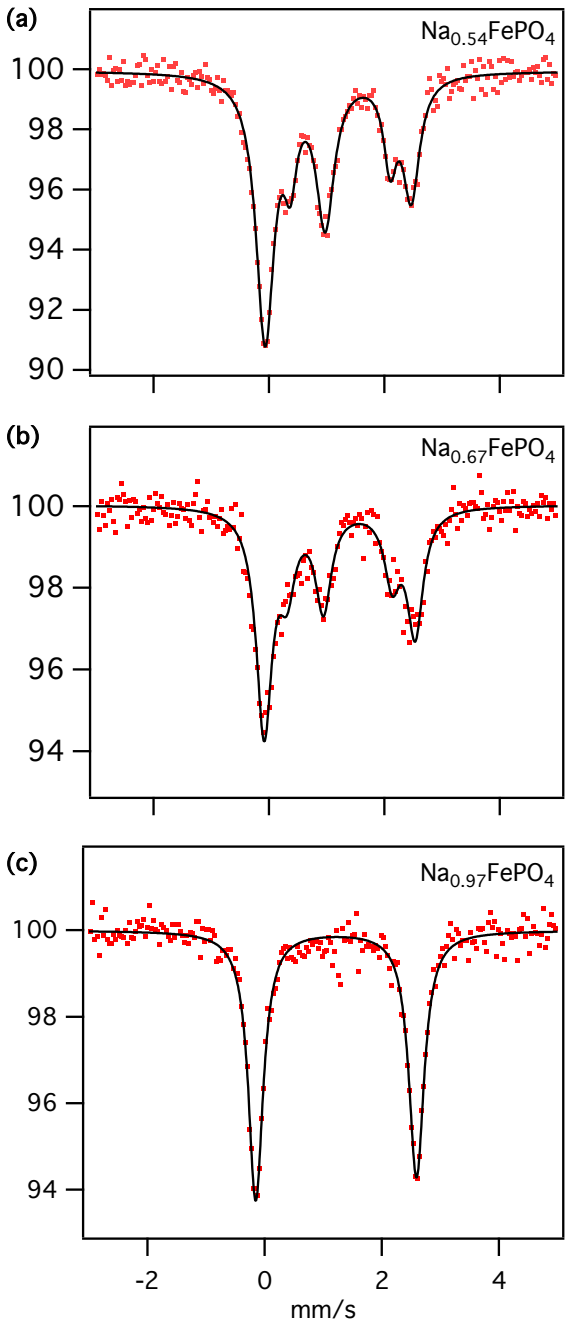

Figure 6.6. 298 K Mössbauer spectra Na_xFePO_4 (x=0.54, 0.67, 0.97).

relaxation time relative to the lifetime of the excited state, the effective widths of the resonance lines can either sharpen or broaden inhomogeneously and amalgamate. While the probability of a transition between the excited state and the ground state with the emission of photon is Lorentzian in form, the observed probability results from a sum over the possible ground states and a stochastic average over the sampled excited states. For polycrystalline samples, the problem reduces to the simplest case treated by Blume and Tjon in which the stochastic and quantum mechanical parts of the problem are separable as there is no issue of non-commutativity of the Hamiltonian at different times.

The fluctuations from polaron hopping require a set of hyperfine parameters for each iron site, together with a relaxation matrix of transition rates,

$$\mathbf{W} = \begin{bmatrix} -\Gamma\rho_{3+} & \Gamma\rho_{3+} \\ \Gamma\rho_{2+B} & -\Gamma\rho_{2+B} \end{bmatrix}. \tag{6.3}$$

To maintain charge balance, the elements of the relaxation matrix are weighted by the populations of the sites, ρ. This allows for the refinement of the relative weight of each site and the polaron hopping frequency, $\Gamma(T)$. The weight ratio of ferrous A/B-type iron sites was also introduced as a fit parameter. For the fits shown in Fig. 6.5, the valence fluctuations were limited to charge hopping between B-type ferrous sites and Fe^{3+} sites, while the A-type ferrous sites were treated as static. This assumption was justified by the observation that the onset of valence fluctuations coincides with a decrease in the fraction of the A-type ferrous site, suggesting the valence fluctuations are largely limited to the B-type iron environment. The Blume-Tjon model was not used for the spectra below 400 K. These spectra were fit with a static model.

Above 400 K the sample begins to show a minor impurity component as a result of oxidation. A comparison of the initial 298 K spectrum and a final spectrum collected after cooling to room temperature from 553 K, reveals a $\sim$16$\%$ decrease in the concentration of ferrous iron. This down temperature spectrum is shown in Fig. 6.7. X-ray diffraction completed at the conclusion of the measurement did not show any indication of a second crystalline phase. The oxidation is likely a result of a reaction with O_2 to produce amorphous Fe_2O_3. For temperatures above 500 K, a second ferric site was added to the fit model to account for this oxidation. This site did not participate in the

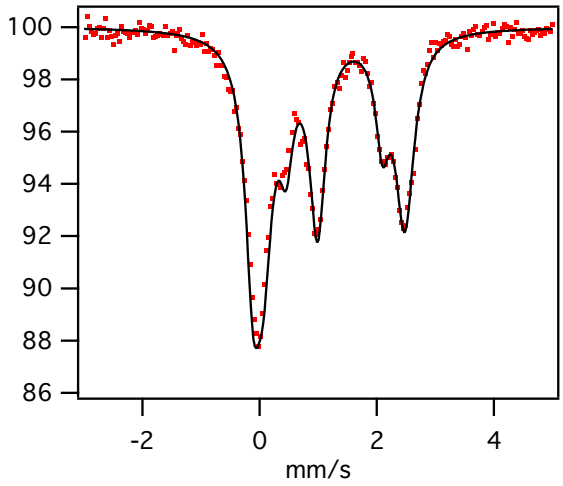

Figure 6.7. Down-temperature spectrum, at 298 K, acquired after cooling from 550 K.

dynamics and the hyperfine parameters of this site were fixed as $IS = 0.31$mm/s and $QS = 0.99$ mm/s. As the temperature was further increased, the spectral contribution of this site was left as a fit parameter and allowed to drift upward with the restriction that the total weight of the ferric contribution to the spectra could not exceed the observed ferric contribution from the down temperature measurement.

All hyperfine parameters showed gradual linear trends as a function of temperature. The temperature dependence of the quadruple splittings of the ferrous iron sites (high spin) are expected to follow an Ingalls-type model [96], where the degeneracy of the t_{2g} levels is removed owing to a Boltzmann occupation of the different crystal field split $t_{2g}\downarrow$ electronic levels by the sixth valence electron,

$$\Delta QS^{2+}(T) \sim \Delta QS_v \frac{1 - \exp^{\frac{-\Delta}{k_B T}}}{1 + 2\exp^{\frac{-\Delta}{k_B T}}} + \Delta QS_l. \tag{6.4}$$

Here ΔQS_v and ΔQS_l refer to the ground state valence and lattice contributions to the quadrupole splitting. The ground state quadrupole splittings and the t_{2g} level splitting (Δ) were determined from best fits to the temperature trends, giving $\Delta = 104$ meV, $QS_v = 2.406$ mm/s, $QS_l^A = 0.33$ mm/s, and $QS_l^B = -0.54$ mm/s. At 473 K there is an abrupt jump in the B-sites quadrupole splitting of $\sim$0.09 mm/s. Following this discontinuity, the thermal trend in the quadrupole splitting continues to follow the same Ingalls-type slope as lower temperatures.

Having one fewer valence electron, ferric sites should not exhibit the Ingalls-type crystal-field

splitting effect. Therefore, any thermal trend in the quadrupole splitting is presumably related to an evolution in the local bonding environment. The temperature dependence of the Fe^{3+} quadrupole splitting has an approximately linear temperature trend,

$$\Delta QS^{3+}(T) = 1.8 - 2 \times 10^{-3} \times T. \tag{6.5}$$

The isomer shift for all sites showed progressive reduction with temperature, following approximately linear trends:

$$\begin{aligned} IS_A^{2+}(T) &= 1.6 - 1.0 \times 10^{-3} \times T, \\ IS_B^{2+}(T) &= 1.5 - 7.0 \times 10^{-4} \times T, \\ IS^{3+}(T) &= 1.0 - 1.0 \times 10^{-3} \times T. \end{aligned} \tag{6.6}$$

This decrease is in part related to the temperature-dependent second-order Doppler shift, [43],

$$\begin{aligned} IS(T) &= \delta_0 - \frac{9k_B\Theta_D}{16Mc}\left[1 + 8\left(\frac{T}{\Theta_D}\right)^4 \int_0^{\frac{\Theta_D}{T}} \frac{x^3}{\exp(x)-1}dx\right], \\ IS(T) &\sim \delta_0 - \frac{3k_BT}{2Mc}\left[1 + \frac{\Theta_D^2}{20T^2}\right], T > \Theta_D, \end{aligned} \tag{6.7}$$

where Θ_D is the Debye temperature, M is the nuclear mass, c is the speed of light and δ_0 is the intrinsic isomer shift.

An inspection of Fig. 6.5 suggests that temperatures around 420 K, there is a onset of electronic dynamics that give rise to spectral distortions, including line broadening and a collapse of the Fe^{2+} and Fe^{3+} doublets. Figure 6.8 shows a plot for the polaron hopping frequencies, $\Gamma(T)$, determined from the fits to the spectra shown in Fig. 6.5. Figure 6.9 shows the evolution of the iron site occupancies as a function of temperature, as determined from these fits. Starting at 450 K there is a rapid conversion of A-type to B-type ferrous iron sites. The data set in Fig. 6.8 was fit with Eq. 6.1 to determine the activation energy for polaron hopping. The activation energy was found to be 505 ± 50 meV, where the uncertainty arises from the choice a prefactor for Eq. 6.1. This value is comparable to the result obtained for $LiFePO_4$ of 470 meV [95].

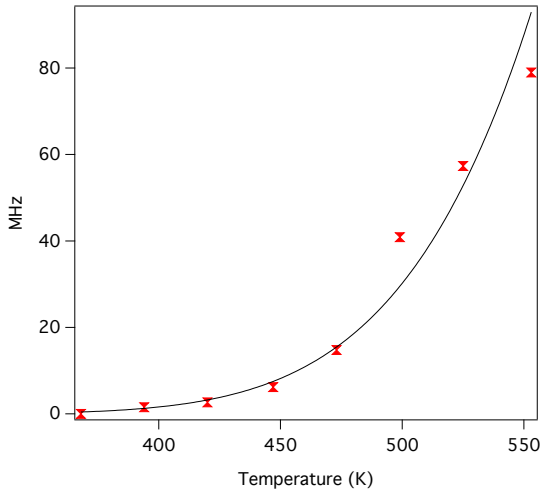

Figure 6.8. (**a**) Polaron hopping frequencies, $\Gamma(T)$, as determined from the solid curves of Fig. 6.5. Solid curve is an Arrhenius-type fit.

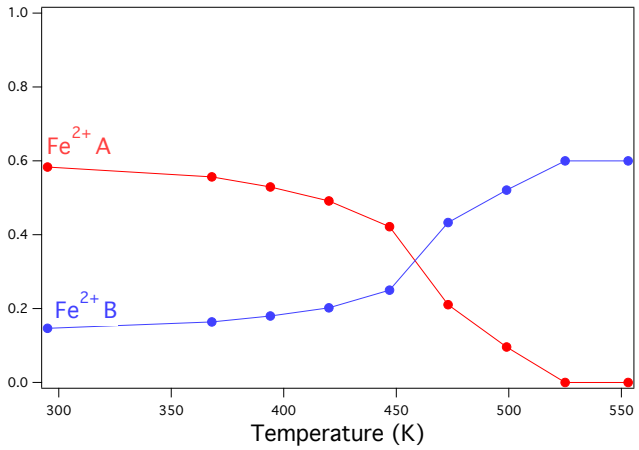

Figure 6.9. Relative weight of Fe^{2+} iron sites as a function of temperature, as determined from fits to Mössbauer spectra.

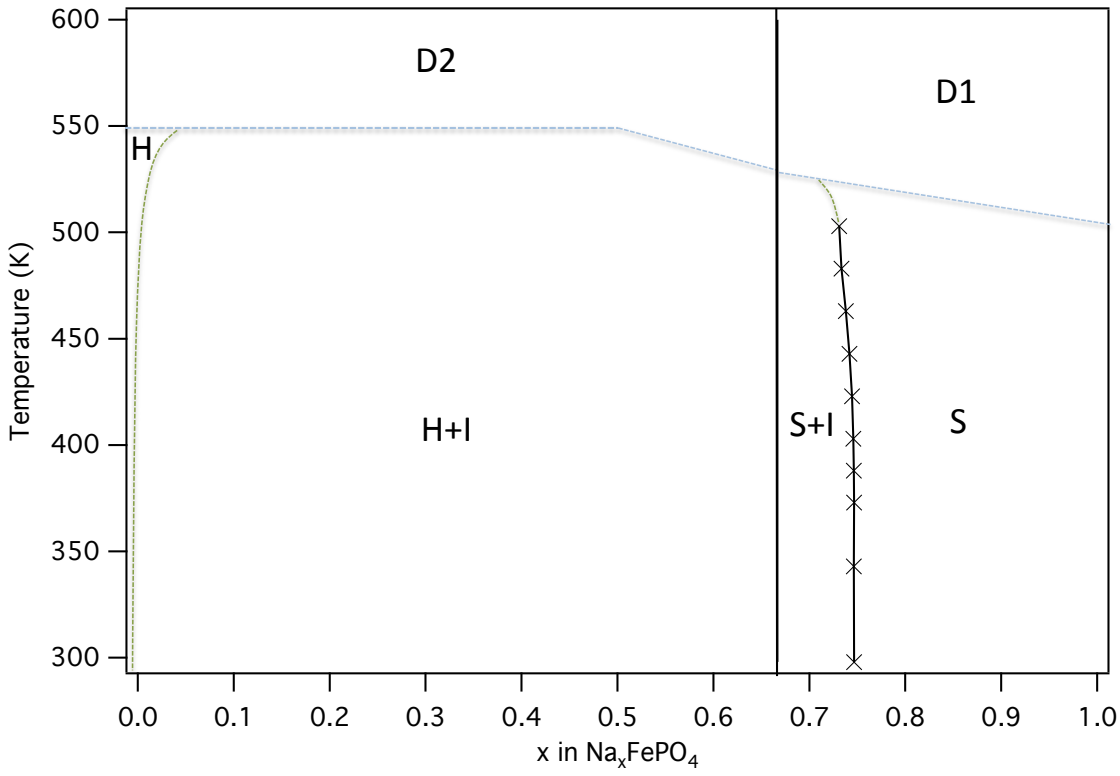

Figure 6.10. Revised phase Diagram, including two phase region above x=2/3.

6.4 Discussion

The solid solution lattice parameters (Fig. 6.4) show a gradual contraction of the pnma a-axis up to 483 K. As the weight ratio of the solid-solution phase grows relative to the ordered phase, there is a concomitant drop in the sodium concentration in the solid solution. This results in a contraction of the a-axis that dominates the thermal expansion for temperatures up to the crossover into a single-phase region, at which point there is no longer a driving force for sodium to leave the solid solution. The other two axes show thermal expansion throughout the entire temperature range, although both show a kink between 443 and 483 K. This discontinuity can be identified as the crossing of a phase boundary into a region of complete sodium disordering on the lattice. Within this temperature range, there is a rapid drop in the sodium concentration in the solid solution as the lower concentration ordered phase is converted to a solid solution. This corresponds to the temperature range of the loss of superstructure peaks. While a minority ordered component does not entirely disappear until 523 K, this is probably a result of delayed kinetics.

Figure 6.10 shows a revised phase diagram for the Na_xFePO_4 system that includes a two phase region above x=2/3. The points along the phase line separating the two phase region from the solid solution were determined from the Rietveld analysis. The blue dashed lines in this figure are from pervious phase diagram study by Lu et. al. [16] and the green dashed line is added to account for some degree of solubility of vacancies in the heterosite phase. At the highest temperatures the sample will revert to the maricite phase plus some combination of phosphate oxides depending on the concentration.

The phase stability of the Na_xFePO_4 system is likely influenced by the details of the coulombic interactions between the Na-ions, Na-vacancies, electrons, and holes. In Li_xFePO_4, the two-body interactions between Li^+, vacancies (V), Fe^{2+}, and Fe^{3+} are essential to understanding the phase behavior. While Li^+/Li^+, and V/V interactions promote the formation of a solid solution, the Li^+/Fe^{2+} and Li^+/Fe^{3+} interactions contribute to a tendency for phase separation. As temperature increases, the electronic configurational entropy from the disordering of the electrons and holes on the lattice dominates [25].

Solid solutions of Li_xFePO_4 (stable above 473 K) are easily preserved at room temperature by quenching. Mössbauer spectra of these quenched samples show broadened quadrupole splitting distributions and an overall decrease in the splitting compared to the pure end members, particularly of the minority site [65]. This results from a sampling of a range of local environments, as expected for a solid solution. The larger shift in the splitting of the minority component arises as a result of a large number of sites that are dissimilar to the environment seen in the end member, i.e. an Fe^{3+} site surrounded by Li-ions. In contrast to the broadened distributions seen in $LiFePO_4$, the sodiated samples show two discrete ferrous components, indicating the presence of two structurally distinct local environments for ferrous iron. The A-type site is reminiscent of the Mössbauer spectra of the fully sodiated structure which exhibits a single site with a quadruple splitting of 2.74 mm/s. The abnormally low quadruple splitting of the B-site (1.7 mm/s) is suggestive of a local environment that is quite different, consistent with a sodium-deficient local environment.

Samples prepared with sodium concentrations below x=2/3 all show ferrous components with area ratio of B/A-type sites of $\sim$34/66, in reasonable agreement with previous results [16,26]. In the study by Lu, et. al., samples in the concentration range Na_xFePO_4 ($x = 0.1 - 2/3$) exhibited an area ratio of approximately 40/60. This range is within a two-phase regime of $FePO_4$ and $Na_{2/3}FePO_4$.

Above this threshold, as additional sodium is inserted into the lattice, the concentration of the B-component falls off with the concentration of ferric iron. The relative ratio of the two ferrous components in the present sample (20/80) is consistent with these results. In another recent study by Boucher, et al., the room temperature spectrum showed a 30/70 ferrous site ratio, but when the same sample was cooled to liquid nitrogen temperatures the spectrum no longer contained a secondary B-site with anomalously low splitting. Instead, the spectrum could be fit with two overlapping Gaussians, having a 50/50 weight ratio and quadrupole splittings of 2.5 and 2.9 mm/s [26]. The authors suggested the presence of the secondary doublet at room temperature may result from rapid electron dynamics, similar to the dynamical effects that are observed at higher temperatures in Li_xFePO_4.

Because the present sample ($x = 0.73$) is biphasic at room temperature, it is tempting to attribute the two doublets to ferrous iron in the two phases. A combination of previous XRD and Mössbauer work show that the secondary component is present for concentrations below $x = 2/3$, where all ferrous iron is within the ordered structure. This observation, combined with the consistent area ratio of the two doublets for all concentrations below x=2/3, suggests the secondary ferrous doublet is inherent to the ordered structure. At 298 K the ordered phase makes up only 20% of the $Na_{0.73}FePO_4$ sample. The retention of the two sharp spectral doublets suggests that the local structure remains much the same in the solid solution phase, at least at room temperature. It appears that the solid solution retains much of the framework of the ordered structure, shown in Fig. 6.1(b), with additional sodium ions distributed randomly on the Pmna (220) planes.

The ∼34/66 weight ratio of the ferrous sites in the room temperature ordered phase seems to contradict the proposed superstructure, determined from synchrotron x-ray diffraction and transmission electron microscopy [26]. In the fully sodiated structure, each iron has three pairs of symmetrically positioned sodium ions, forming a distorted triangular prism. In the proposed superstructure, shown in Fig. 6.11, every third sodium along Pmna b-axis is vacant, giving rise to three distinct iron sites with a 1/1/1 weight ratio. The three sites correspond to sites with one, two and three vacancies in their six-fold sodium coordination shell. In 6.11 these sites are shown in red, green and blue, respectively. Calculation of a sodium specific effective coordination number (ECoN) gives 3.72,

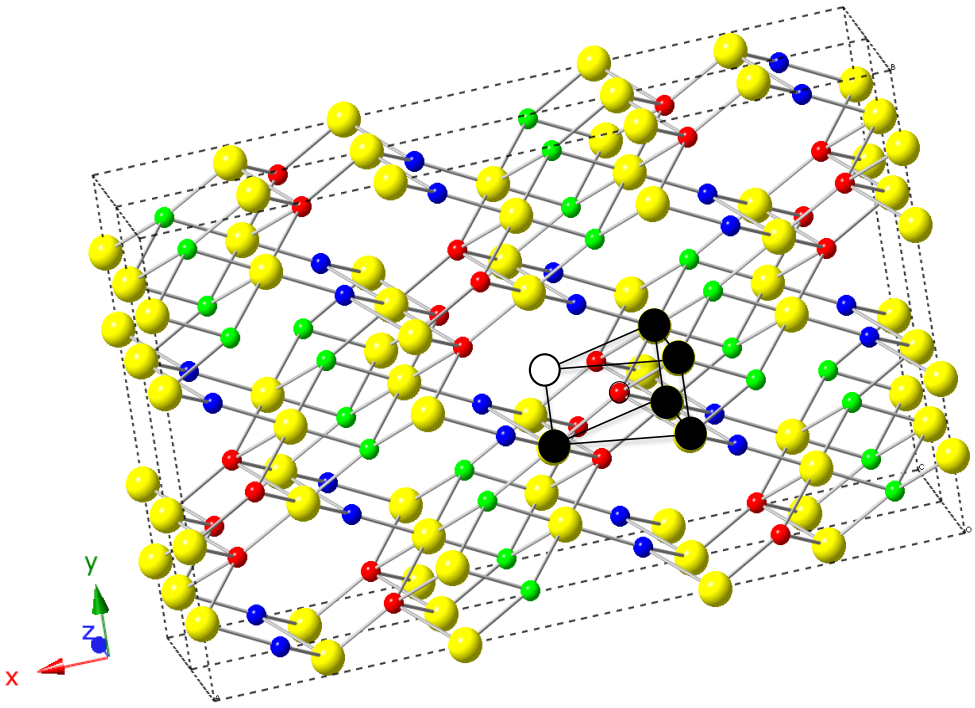

Figure 6.11. Sodium-ion sublattice of the $x = 2/3$ ordered phase. Sodium ions are shown in yellow and three structurally distinct iron sites are shown in blue, green and red, corresponding to iron sites with three, two and one vacancies in the six-fold sodium coordination shell. The pyramidal outline of this coordination shell in shown in black for a red-type iron site.

3.69, and 2.990 for the red, green and blue sites. Here ECoN is defined as [97],

$$\text{ECoN} = \sum_i \exp\left[1 - \left(\frac{r_i}{\langle r \rangle}\right)^6\right], \qquad \langle r \rangle = \frac{\sum_i r_i \exp\left[1-\left(\frac{r_i}{r_{min}}\right)^6\right]}{\sum_i \exp\left[1-\left(\frac{r_i}{r_{min}}\right)^6\right]}, \tag{6.8}$$

where r_{min} is the shortest bond in the set and the sum is made over all Fe-Na bonds below a cutoff radius of 4 Å.

Figure 6.12 illustrates the proposed evolution of the iron and sodium site occupancies with increasing temperature. The three iron sites in the ordered structure are depicted with their Na-coordination shells for four temperatures between 77 K and 500 K. The temperatures are listed at the top of the figure along with the B/A site ratios of the ferrous components in the Mössbauer spectra. In this figure sodium ions are depicted in black and sodium vacancies in white. The central

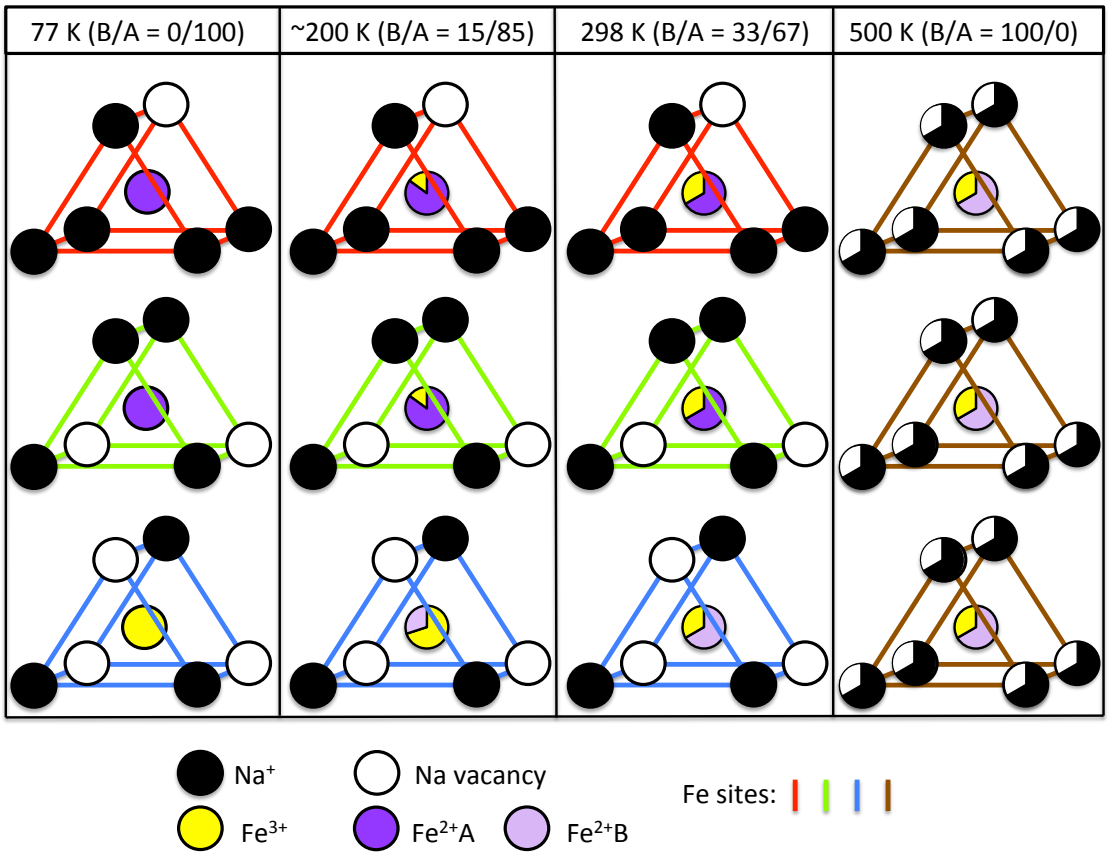

Figure 6.12. Temperature evolution of three iron sites in $Na_{2/3}FePO_4$ structure. Fe^{3+} ions are shown in yellow and Fe^{2+} in purple, where dark purple and lavender depict A- and B-type ferrous sites. Sodium ions are shown in black and sodium vacancies are shown in white. The pyramidal outline reflects the coordination environment of the central iron site, corresponding to the colors of the iron ions shown in Fig. 6.11. Red represents a crystallographic iron site with five sodium neighbors, green represents an iron site with four sodium neighbors, blue represents an iron site with three sodium neighbors and brown represents the average coordination environment for an iron site in the disordered solid solution phase. Temperature is listed at the top of each column along with B/A site ratio.

iron ion is shown in yellow for Fe^{3+} and purple for Fe^{2+}, where the local environment of the ferrous iron sites is indicated with different shades of purple. The sodium-rich and sodium-deficient environments that give rise to the A- and B-type sites in the Mössbauer spectrum are depicted with dark purple and lavender, respectively. The color of the pyramidal frame reflects the coordination environment of the central iron site, where the red, green and blue outlines correspond to the three iron sites in Fig. 6.11, having one, two and three surrounding vacancies, respectively. Upon total disordering of the Na sublattice, the three iron sites in 6.11 are no longer distinct and the outline of the coordination shells in Fig. 6.12 are shown in brown.

Electrostatic considerations suggest that the Fe^{3+} holes prefer the blue sites, surrounded by vacancies, while the Fe^{2+} electrons prefer the sodium rich red or green sites. Below room temperature, we expect charge ordering on the lattice reflecting this preference. Assuming the quadrupole splitting decreases with sodium coordination, the 77 K Mössbauer spectrum can be interpreted as the divalent cations exclusively occupying the the red- and green-type sites, shown in the first column of Fig. 6.12. Given that the red and green sites have similar effective coordination numbers, this charge ordering gives rise to two ferrous sites with similar quadrupole splittings in a 50/50 ratio.

While the diffraction results rule out a significant rearrangement of sodium ions between 77 K and room temperature, this type of charge localization transition below room temperature is a possibility. As the temperature is raised, a disordering of electrons and holes on the lattice results in a partial ferrous occupancy of the blue-type sites (with three sodium neighbors). The relatively low effective coordination number of the blue site could account for the unusually low quadruple splitting of the B-type component in the Mössbauer spectrum. At even higher temperatures, a random distribution of electrons on the three iron sites results in 1/3 of the ferrous iron sites, or $\sim 22\%$ of the total iron sites, with an Fe^{2+} ion in a sodium-deficient blue-type environment (third column of Fig. 6.12). Moreover, if the bonding environment of the red and green sites gives rise to similar values for QS, this electronically disordered state gives a B/A weight ratio of 33/67, consistent with the experimentally-observed $\sim$34/66 ratio. For concentrations above x=2/3, as additional sodium is inserted into the lattice, blue sites are converted to red sites and trivalent green sites become divalent. The result is a fall-off in the weight fraction of the B-type ferrous sites that tracks the concentration of trivalent iron.

Above 450 K, x-ray diffraction shows a loss of local order on the sodium sublattice, and Möss-

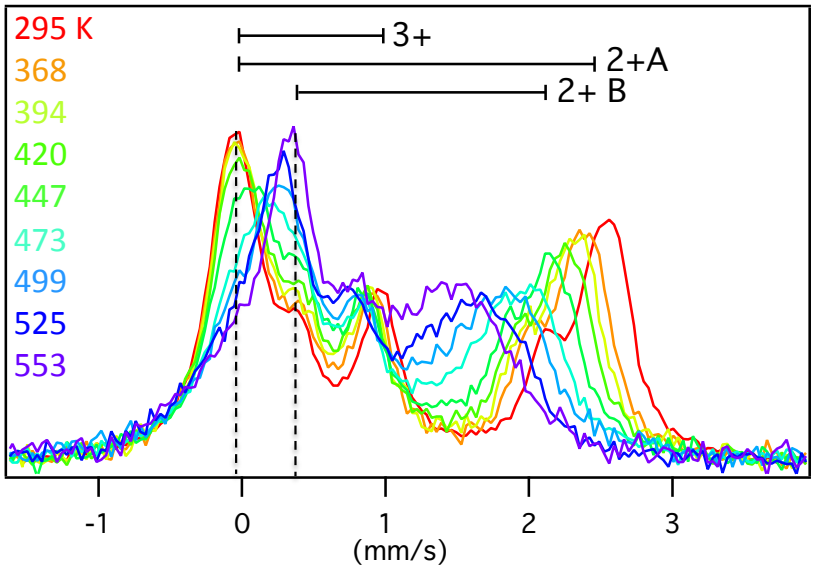

Figure 6.13. Mössbauer spectrometry of Fig. 6.5, inverted, stacked and normalized for comparison. Dotted lines mark the A- and B-type ferrous absorptions at ∼0 mm/s.

bauer spectrometry shows that all three sites start to look like a single site with an average sodium coordination. With this delocalization of sodium on the lattice, there is an overall reduction of sodium coordination around the iron sites. Red and green-type sites that result from clustering of sodium in the ordered structure are converted to sites with lower sodium coordination. This is seen as an overall conversion of A-type sites to B-type sites as the temperature increases above 298 K. This is particularly evident from an inspection of Fig. 6.13, where the Mössbauer spectra have been inverted, normalized and overlaid for comparison. At low temperature the ferrous absorption lines at ∼0 mm/s are distinct, but with increasing temperature the weight of the B-type absorption line grows relative to the A-type line. By 473 K, it appears that the B-type environment becomes the majority divalent component. For the absorption lines at ∼2 mm/s, this effect is obscured by the spectral collapse of the Fe^{2+} and Fe^{3+} lines that results from the concurrent onset of fast charge hopping. This evolution of the iron environments is also apparent from the discontinuity in the Fe_B^{2+} quadrupole splitting between 447 K and 473 K. This jump represents an abrupt local change in the B-type iron site, suggestive of a moderate increase in sodium coordination, as expected upon sodium disordering.

The temperature range of sodium delocalization on the lattice corresponds with the temperature

range where electronic dynamics begin to show large effects in the Mössbauer spectra. An analysis of the data of Fig. 6.5 gave an activation energy of 505$\pm$ 50 meV. This is comparable to the value determined using nuclear resonant scattering in Li_xFePO_4 of 470 meV [95]. In the lithium system, the onset of clear dynamical effects in the Mössbauer spectra is seen at a temperature $\sim$60 K below the onset in $NaFePO_4$. As the ion activation barrier is expected to be higher in the sodium system, a temperature offset for ion delocalization of this magnitude is not unexpected. The higher temperature onset of electronic valence fluctuations despite the comparable polaron activation barrier point to the central role of the ion delocalization for the onset of electronic dynamics. It appears that sodium disordering is required before the onset of electronic mobility.

Recent work looking at the activation barrier for polaron hopping in $LiFePO_4$ suggested that the mobility of the electronic carriers is correlated to the Li-ion mobility [95]. It was deduced that strong binding and polaron-ion correlation should suppress the intrinsic electronic conductivity of Li_xFePO_4 and may also affect the diffusion of Li^+ ions. Similar to $LiFePO_4$, simulations suggest that Na^+ ions diffuse readily along a [010] channels and there is a high energy barrier to cross between channels [15]. While the calculated activation barrier for ion mobility in $NaFePO_4$ is higher than in Li_xFePO_4, it is still below 400 meV, implying reasonably facile ionic mobility. The delayed onset of electron dynamics in the Mössbauer spectra compared to $LiFePO_4$ is likely a result of a higher activation energy for ion hopping.

6.5 Conclusions

Mössbauer spectra of $Na_{0.73}FePO_4$ were measured for temperatures between 298 K and 553 K. An analysis of the spectra using the Blume–Tjon model for a system with a fluctuating nuclear Hamiltonan gave frequencies of Fe valence fluctuations that correspond to frequencies of polaron hopping. This analysis allowed for the determination of an activation energy for polaron hopping of 505 meV. Synchrotron x-ray diffraction measurements collected in the same temperature range showed that the disordering of the sodium sublattice coincided with a marked enhancement in the electronic valence fluctuations that give rise to distortions in Mössbauer spectra. Additionally, the synchrotron x-ray diffraction data revealed the presence a two phase region between the solid solution and ordered phases.

The combination of the diffraction and Mössbauer results gave new information concerning the temperature evolution of the iron and sodium site occupancies. At the lowest temperatures there is a preference for both sodium ordering and electronic charge ordering. As the temperature increases, electronic disorder started to develop, giving rise to ferrous iron in sodium deficient local environments. The site occupancies from the room temperature Mössbauer spectrum indicate total electronic disorder. Despite this apparent loss of electronic ordering, there is no evidence of charge dynamics in the Mössbauer spectra, implying the polaron rate hopping at 298 K is still below the MHz range. Above 450 K, there is a complete loss of order on the sodium sublattice, giving rise to a true solid solution phase. This is also the range where the Mössbauer spectra begin to exhibit distortions constant with fast charge hopping, suggesting a relationship between the onset of fast electron dynamics and the redistribution of sodium in the lattice. These results clarify details related to the sodium and electronic charge ordering in the structure and suggest that electron-ion interactions play a role in both the phase stability and the elevated temperature charge dynamics.

Chapter 7

Conclusions and future work

The interacting transport properties of transition-metal intercalation compounds make for a fascinating research topic. The interplay between electron and ion mobility and the details of how these transport properties are influenced by crystal structure gives rise to interesting fundamental physics. Developing a local picture of how charge moves through the lattice is a perspective that has received little attention. The focus of this thesis was activation barrier measurements for charge hopping in the olivine-phosphate family. Nuclear resonant scattering measurements allowed for a study of the local dynamics of thermally-activated polaron hopping in lithium and sodium-iron phosphate. This led to new insights into the correlation between electronic carriers and mobile ions. There is a great deal of interest in this family of materials due to their potential use in next generation battery electrodes and new details concerning the influence of polaron-ion interactions on the charge dynamics are relevant for optimizing the electrochemical performance of these materials.

My first experiments employed synchrotron nuclear forward scattering measurements at elevated temperature and pressure to determine an activation volume for the charge hopping process. This is the first use of nuclear resonant scattering to determine an activation volume. These results showed the valence fluctuations in Li_xFePO_4 are strongly sensitive to pressure, giving an anomalously large and positive activation volume. This large, positive value is typical of ion diffusion, pointing to a cooperative mobility of polarons and Li-ions. My second study looked at the sodium analogue of Li_xFePO_4. The sodiated material shows several interesting differences in phase stability, including an ordered intermediated phase. A combination of synchrotron XRD and conventional Mössbauer spectrometry allowed for the study of the temperature evolution of the delocalization of

both Na-ions and electronic carriers on the lattice. These results revealed that the loss of sodium-ordering coincides with a marked enhancement of electronic valence fluctuations. These results show a new relationship between the ordering of the sodium and the electronic charge, and suggest that polaron-ion interactions may play an important role in the dynamics of Na_xFePO_4 at elevated temperature.

7.1 Future work

7.1.1 Pair distribution study of Li_xFePO_4

A pair distribution function (PDF) investigation of the local structure of Li_xFePO_4 as a function of temperature and pressure would provide a structural counterpart to the nuclear resonant scattering work presented in this thesis. Nuclear resonant scattering data provides valuable information about the local electronic state of the iron ion, but the interpretation of our results would benefit from a better picture of the local structure. While in-situ diffraction was collected during the nuclear forward scattering experiments, these data gave only global structural information.

Sector 11 at the Advanced Photon Source has the capability to conduct both high pressure and high temperature PDF measurements. While PDF studies as a function of temperature are now relatively routine, studies at elevated pressure remain a challenge. The small sample volumes necessary for conducting diamond anvil cell experiments result in a high ratio of background to sample scattering. Additionally, quality PDF data require access to high scattering angles so the restricted angular opening of a typical diamond anvil cell is problematic. Despite these challenges, ongoing development work at sector 11 has made measurements up to 15 GPa possible. This is well within the pressure range of interest for studies of polaron dynamics in Li_xFePO_4. Combining high pressure and temperature capabilities would likely involve additional development work, but two independent studies of the temperature evolution and the pressure evolution of the pair distribution function would have the potential to provide valuable information, including chemical short-range order and thermal broadening of nearest-neighbor separations.

7.1.2 Mössbauer study of electron dynamics in maricite-$NaFePO_4$

Maricite is the ground state structure of $NaFePO_4$. The triphylite structure is obtained only via an ion-exchange route. Figure 1.7 illustrates the structural differences between these two polymorphs. In maricite, the site occupancies of the mobile ion are swapped with the iron cations. Consequently, the sodium ions are isolated. As the structure lacks viable diffusion channels, maricite is electrochemically inactive. Despite the diminished ionic mobility, it is likely that polaron-ion interactions still play a role in the electron dynamics. In the maricite structure the iron octahedra have edge-sharing connectivity, compared to the corner sharing network in triphylite. This results in a closer iron-iron distance. The reduction in jump distance likely lowers the activation barrier for polaron hopping, although if polaron-ion correlations influence the dynamics it is possible that the lack of ion mobility results in a diminished electronic mobility as well. A Mössbauer study of the temperature dependence of the polaron hopping rate in the maricite polymorph compared to the triphylite structure would reveal new information concerning the relevance of ion conduction pathways to the electronic charge dynamics. Furthermore, a study of the phase stability of this structure as a function of sodium concentration is potentially interesting as well.

7.1.3 Nuclear resonant scattering study of activation barriers in Li_2FeSiO_4

Li_2FeSiO_4 is another interesting material to study using nuclear resonant scattering. As all its constituent elements are earth abundant, Li_2FeSiO_4 is an attractive candidate cathode material. Additionally, the Li_2FeSiO_4 system presents the possibility of removing two electrons for each iron cation, theoretically resulting in a higher capacity. Shown in Fig. 1.5 (e), the structure has two-dimensional ion conduction networks. As a result, the ion mobility is likely improved compared to $LiFePO_4$ and the issues related to channel blocking by defects in $LiFePO_4$ are not present. Unfortunately Li_2FeSiO_4 has not proved successful as a battery electrode, in part for reasons of low electronic conductivity. A study of the pressure and temperature dependence of the polaron hopping rate in Li_2FeSiO_4 could give insight into the relevance of the dimensionality of the ion conduction pathways to the electronic activation barrier.

7.1.4 Activation volume studies

Experiments on activation volumes are a largely unexplored. The concept of an activation volume is not limited to polaron hopping and applies to a wide range of activated processes in solids. Ongoing developments in tools for high pressure measurements are making pressure studies possible for different scattering techniques and expanding the availability of sample environments. With these advancements, the study of activation volumes is becoming increasingly accessible. While there are a number of additional iron-bearing polaronic systems that could be studied, in theory it should be possible apply the same technique to determine of an activation volume for atomic diffusion as well by looking at "speedup" effects in nuclear forward scattering spectra due to incoherent motions of a diffusing species. Iron diffusion is relevant to a number of structural and geological materials. An understanding of how this type of diffusion is affected by pressure seems particularly relevant to geological materials.

While nuclear forward scattering studies are limited to samples with resonant isotopes, other techniques that measure dynamical properties could be extended to high pressures to obtain activation volumes as well. One possibility is using quasielastic neutron scattering to investigate the activation volumes for the diffusion of light elements. The recent developments in high pressure cells for neutron experiments open up the potential for these types of experiments. Diffusion of light atoms in host structures has many parallels to polaron mobility, and conducting an activation volume study could provide important physical information concerning the local dynamics. This technique could be applied to a range of different types of hydrogen storage materials.

Bibliography

[1] T. Holstein, *Ann. Phys.*, vol. 8, no. 3, pp. 343 – 389, 1959.

[2] R. Röhlsberger, *Nuclear Condensed Matter Physics with Synchrotron Radiation Basic Principles, Methodology and Applications*. Springer-Verlag, 2004.

[3] J. Zhao *et al.*, *High Pressure Res.*, vol. 24, no. 4, pp. 447–457, 2004.

[4] G. Pancaldi, *Hist. Stud. Phys. Biol. Sci.*, vol. 21, no. 1, pp. 123–160, 1990.

[5] M. Whittingham, *Prog. Solid State Chem.*, vol. 12, no. 1, pp. 41–99, 1978.

[6] A. Nagelberg and W. Worrell, *J. Solid State Chem.*, vol. 29, no. 3, pp. 345–354, 1979.

[7] C. Delmas *et al.*, *Solid State Ionics*, vol. 3-4, no. AUG, pp. 165–169, 1981.

[8] J. Braconnier, C. Delmas, and P. Hagenmuller, *Mater. Res. Bull.*, vol. 17, no. 8, pp. 993–1000, 1982.

[9] J. Molenda, C. Delmas, and P. Hagenmuller, *Solid State Ionics*, vol. 9-10, no. DEC, pp. 431–435, 1983.

[10] J. Tarascon and G. Hull, *Solid State Ionics*, vol. 22, no. 1, pp. 85–96, 1986.

[11] P. Axmann *et al.*, *Chem. Mater.*, vol. 21, no. 8, pp. 1636–1644, 2009.

[12] D. Morgan, A. Van der Ven, and G. Ceder, *Electrochem. Solid St.*, vol. 7, no. 2, pp. A30–A32, 2004.

[13] A. Yamada, S. C. Chung, and K. Hinokuma, *J. Electrochem. Soc*, vol. 148, no. 3, pp. A224–A229, 2001.

[14] H. Huang, S.-C. Yin, and L. F. Nazar, *Electrochem. Solid St.*, vol. 4, no. 10, pp. A170–A172, 2001.

[15] S. P. Ong *et al.*, *Energy Environ. Sci.*, vol. 4, pp. 3680–3688, 2011.

[16] J. Lu *et al.*, *Chem. Mater.*, vol. 25, no. 22, pp. 4557–4565, 2013.

[17] Y. Zhu *et al.*, *Nanoscale*, vol. 5, no. 2, pp. 780–787, 2013.

[18] S.-M. Oh *et al.*, *Electrochem. Commun.*, vol. 22, no. 0, pp. 149 – 152, 2012.

[19] A. Van der Ven *et al.*, *J. Electrochem. Soc.*, vol. 156, no. 11, pp. A949–A957, 2009.

[20] R. Malik, F. Zhou, and G. Ceder, *Nat. Mater.*, vol. 10, no. 8, pp. 587–590, 08 2011.

[21] M. Wagemaker, F. M. Mulder, and A. Van der Ven, *Adv. Mater.*, vol. 21, no. 25-26, pp. 2703–2709, 2009.

[22] C. Delmas *et al.*, *Nat. Mater.*, vol. 7, no. 8, pp. 665–671, 08 2008.

[23] J. L. Dodd, R. Yazami, and B. Fultz, *Electrochem. Solid St.*, vol. 9, no. 3, pp. A151–A155, 2006.

[24] C. Delacourt *et al.*, *Nat. Mater.*, vol. 4, no. 3, pp. 254–260, 2005.

[25] F. Zhou, T. Maxisch, and G. Ceder, *Phys. Rev. Lett.*, vol. 97, p. 155704, 2006.

[26] F. Boucher *et al.*, *J. Electrochem. Soc.*, vol. 136, no. 25, pp. 9144–9157, 2014.

[27] L. Landau, *Phys. Z. Sowjetunion*, vol. 3, no. 3, p. 644?645, 1933.

[28] T. Holstein, *Ann. Phys.*, vol. 8, no. 3, pp. 325 – 342, 1959.

[29] J. Appel, "Polarons," in *Solid State Physics*, F. Seitz, D. Turnbull, and E. Ehreneich, Eds. Academic Press Inc., 1968, vol. 21.

[30] A. Goddat, J. Peyronneau, and J. P. Poirier, *Phys. Chem. Miner.*, vol. 27, pp. 81–87, 1999.

[31] T. J. Shankland, J. Peyronneau, and J. P. Poirier, *Nature*, vol. 366, no. 6454, pp. 453–455, 1993.

[32] D. P. Dobson and J. P. Brodholt, *J. Geophys. Res.*, vol. 105, p. 531, 2000.

[33] J. Poirier, A. Goddat, and J. Peyronneau, *Philos. Trans. R. Soc. London, Ser. A*, vol. 354, no. 1711, pp. 1361–1369, 1996.

[34] T. Yoshino, *Surveys in Geophysics*, vol. 31, no. 2, pp. 163–206, 2010.

[35] J. P. Poirier, *Introduction to the Physics of the Earth's Interior*, 2nd ed. Cambridge University Press, 2000.

[36] W. Harrison, *Electronic Structure and the Properties of Solids*. Dover Publications, Inc., 1989.

[37] N. Mott, *J. Non-Cryst. Solids*, vol. 1, no. 1, pp. 1 – 17, 1968.

[38] G. A. Samara, *Solid State Phys.*, vol. 38, pp. 1–80, 1984.

[39] A. P. Hammersley, "Fit2d: An introduction and overview," European Synchrotron Radiation Facility, Tech. Rep. ESRF97HA02T, 1997.

[40] A. C. Larson and R. B. Von Dreele, "General structure analysis system (GSAS)," Los Alamos National Laboratory, Tech. Rep. 86-748, 2000.

[41] B. Toby, *J Appl. Crystallogr.*, vol. 34, no. 2, pp. 10–213, 2001.

[42] P. Stephens, *J Appl. Crystallogr.*, vol. 32, no. 2, pp. 281–289, 1999.

[43] R. Pound and R. GA, *Phys. Rev. Lett.*, vol. 4, no. 6, pp. 274–275, 1960.

[44] P. Pyykkö, *Mol. Phys.*, vol. 106, no. 16-18, pp. 1965–1974, 2008.

[45] W. Sturhahn *et al.*, *Hyperfine Interact.*, vol. 113, no. 1-4, pp. 47–58, 1998.

[46] E. Sterer, M. P. Pasternak, and R. D. Taylor, *Rev. Sci. Instrum.*, vol. 61, no. 3, pp. 1117 –1119, mar 1990.

[47] P. W. Anderson, *J. Phys. Soc. Jpn.*, vol. 9, no. 3, pp. 316–339, 1954.

[48] M. Blume and J. A. Tjon, *Phys. Rev.*, vol. 165, no. 2, p. 446, 1968.

[49] J. A. Tjon and M. Blume, *Phys. Rev.*, vol. 165, pp. 456–461, 1968.

[50] W. Sturhahn, *Hyperfine Interact.*, vol. 125, pp. 149–172, 2000.

[51] A. K. Padhi, K. S. Nanjundaswamy, and J. B. Goodenough, *J. Electrochem. Soc.*, vol. 144, no. 4, pp. 1188–1194, 1997.

[52] F. Zhou *et al.*, *Solid State Commun.*, vol. 132, no. 3–4, pp. 181 – 186, 2004.

[53] K. Zaghib *et al.*, *Chem. Mater.*, vol. 19, no. 15, pp. 3740–3747, 2007.

[54] M. K. Kinyanjui *et al.*, *J. Phys. C: Solid State Phys.*, vol. 22, no. 27, p. 275501, 2010.

[55] S.-I. Nishimura *et al.*, *Nat. Mater.*, vol. 7, no. 9, pp. 707–711, 2008.

[56] P. P. Prosini *et al.*, *Solid State Ionics*, vol. 148, no. 1-2, pp. 45 – 51, 2002.

[57] J. Sugiyama *et al.*, *Phys. Rev. B*, vol. 85, no. 5, p. 054111, 2012.

[58] R. Amin *et al.*, *Solid State Ionics*, vol. 179, no. 2732, pp. 1683 – 1687, 2008.

[59] C. Delacourt *et al.*, *J. Electrochem. Soc.*, vol. 7, no. 12, pp. 1506–1516, 2005.

[60] C. Zhu, K. Weichert, and J. Maier, *Adv. Funct. Mater.*, vol. 21, no. 10, pp. 1917–1921, 2011.

[61] R. Amin, P. Balaya, and J. Maier, *Electrochem. Solid-State Lett.*, vol. 10, no. 1, pp. A13–A16, 2007.

[62] M. Park *et al.*, *J. Power Sources*, vol. 195, no. 24, pp. 7904 – 7929, 2010.

[63] R. Malik, A. Abdellahi, and G. Ceder, *J. Electrochem. Soc.*, vol. 160, no. 5, pp. A3179–A3197, 2013.

[64] S.-Y. Chung, J. T. Bloking, and Y.-M. Chiang, *Nat. Mater.*, vol. 1, no. 2, pp. 123–128, 2002.

[65] H. J. Tan, J. L. Dodd, and B. Fultz, *J. Phys. Chem. C*, vol. 113, no. 6, pp. 2526–2531, 2009.

[66] J. L. Dodd, I. Halevy, and B. Fultz, *J. Phys. Chem. C*, vol. 111, no. 4, pp. 1563–1566, 2007.

[67] B. Ellis *et al.*, *J. Am. Chem. Soc.*, vol. 128, no. 35, pp. 11 416–11 422, 2006.

[68] A. S. Andersson *et al.*, *Solid State Ionics*, vol. 130, no. 1–2, pp. 41 – 52, 2000.

[69] I. Austin and N. Mott, *Adv. Phys.*, vol. 18, no. 71, pp. 41–102, 1969.

[70] M. Takahashi *et al.*, *Solid State Ionics*, vol. 148, no. 3-4, pp. 283–289, 2002.

[71] S. Shi *et al.*, *Phys. Rev. B*, vol. 68, no. 19, p. 195108, 2003.

[72] Y.-N. Xu *et al.*, *Electrochem. Solid-State Lett.*, vol. 7, no. 6, pp. A131–A134, 2004.

[73] C. Delacourt *et al.*, *J. Electrochem. Soc.*, vol. 152, no. 5, pp. A913–A921, 2005.

[74] T. Maxisch, F. Zhou, and G. Ceder, *Phys. Rev. B*, vol. 73, p. 104301, 2006.

[75] S. P. Ong, Y. Mo, and G. Ceder, *Phys. Rev. B*, vol. 85, no. 8, p. 081105, 2012.

[76] C. Chazel *et al.*, *Inorg. Chem.*, vol. 45, no. 3, pp. 1184–1191, 2006.

[77] K. Tateishi, D. du Boulay, and N. Ishizawa, *Appl. Phys. Lett.*, vol. 84, no. 4, pp. 529–531, 2004.

[78] J. L. Dodd, Ph.D. dissertation, California Institute of Technology, 2007, Appendix. http://resolver.caltech.edu/CaltechETD:etd-05072007-184544.

[79] K. Amine, J. Liu, and I. Belharouak, *Electrochem. Commun.*, vol. 7, no. 7, pp. 669–673, 2005.

[80] A. Jayaraman, *Rev. Mod. Phys.*, vol. 55, pp. 65–108, 1983.

[81] W. Sturhahn and E. Gerdau, *Phys. Rev. B*, vol. 49, no. 14, pp. 9285–9294, 1994.

[82] R. Stevens *et al.*, *J. Phys. Chem. B*, vol. 110, no. 45, pp. 22 732–22 735, 2006.

[83] C. Burba and R. Frech, *J. Electrochem. Soc.*, vol. 151, no. 7, pp. A1032–A1038, 2004.

[84] T. Maxisch and G. Ceder, *Phys. Rev. B*, vol. 73, no. 17, pp. 174 112–, 2006.

[85] S. L. Shang *et al.*, *J. Mater. Chem.*, vol. 22, no. 3, pp. 1142–1149, 2012.

[86] P. M. Richards, *Phys. Rev. B*, vol. 16, no. 4, pp. 1393–1409, 1977.

[87] D. Emin, *Adv. Phys.*, vol. 24, no. 3, pp. 305–348, 1975.

[88] J. Lee, S. J. Pennycook, and S. T. Pantelides, *Appl. Phys. Lett.*, vol. 101, no. 3, 2012.

[89] P. Moreau *et al.*, *Chemistry of Materials*, vol. 22, no. 14, pp. 4126–4128, 2010.

[90] K. Zaghib *et al.*, *Journal of Power Sources*, vol. 196, no. 22, pp. 9612 – 9617, 2011.

[91] M. Casas-Cabanas *et al.*, *Journal of Materials Chemistry*, vol. 22, no. 34, pp. 17 421–17 423, 2012.

[92] M. Galceran *et al.*, *Physical Chemistry Chemical Physics*, vol. 16, no. 19, pp. 8837–8842, 2014.

[93] J. Gaubicher *et al.*, *Electrochemistry Communications*, vol. 38, pp. 104–106, JAN 2014.

[94] M. Avdeev *et al.*, *Inorganic Chemistry*, vol. 52, no. 15, pp. 8685–8693, 2013.

[95] S. J. Tracy *et al.*, *Phys. Rev. B*, vol. 90, p. 094303, 2014.

[96] R. Ingalls, *Phys. Rev.*, vol. 133, no. 3A, pp. A787–A795, 1964.

[97] R. Hoppe, *Z. Kristallogr.*, vol. 150, no. 1-4, pp. 23–52, 1979.